
Optimising the Experimental Approach to Nuclear Excitation by Electron Capture

Benjamin Wallis

Doctor of Philosophy

Physics, Engineering and Technology
University of York

June 2021

Abstract

Nuclear Excitation by Electron Capture (NEEC) is a complex process which is at the boundary between atomic and nuclear physics, defined as the inverse of internal conversion. It requires a broad expertise in nuclear, atomic, laser, plasma, and accelerator physics, and so the work is presented from an interdisciplinary perspective. NEEC is part of a wider branch of exotic nuclear excitation mechanisms under the name ‘nuclear isomeric triggering’ or ‘depletion’ and this thesis provides a road-map to constructing NEEC experiments that are able to be compared with the present theoretical models for NEEC. This helps us achieve better numerical estimates as to how feasible NEEC can be as a depletion mechanism in various environments and contexts. We rigorously present a ‘figure of merit’ that can be applied to all NEEC experiments across the different techniques, and provide the first exhaustive candidate search of both the nuclear and subsequent atomic species. This has resulted in an experimental design and astrophysical calculation tool, which is made available to the research community.

COPYRIGHT

This publication is UK Ministry of Defence © Crown copyright (2022). Material and information contained in this publication may be reproduced, stored in a retrieval system and transmitted for MOD use only, except where authority for use by other organisations or individuals has been authorised by a Patent Officer of the Defence Intellectual Property Rights (DIPR) whose details appear below.

Crown Copyright and Merchandise Licensing

Defence Intellectual Property Rights

MOD Abbey Wood South,

Poplar 2 #2214,

Bristol, BS34 8JH

Email: DIPR-Copyright@mod.gov.uk

Contents

Abstract	2
Introduction	10
1 Background and Theory	13
1.1 Internal Conversion	13
1.2 Energy Levels - Defining the Stationary States in the Atom and Nucleus	16
1.2.1 Atom Energy Levels	18
1.2.2 Nuclear Energy Levels	21
1.2.3 Transition Multipolarity and Mixing - Nuclear	22
1.2.4 Transition Rates	24
1.2.5 Transitions from the Electron Continuum	25
2 NEEC Resonance Strength	28
2.1 Resonances	30
2.1.1 Resonance Strength	32
2.1.2 Resonance Strength from the Principle of Detailed Balance	34
2.2 Accuracy of Our Resonance Strength Technique	36
2.3 Different Microscopic Candidate Systems - Defining the State of the Ion and its Constituents	39
2.3.1 Nomenclature and Different NEEC Cases	39
2.3.2 Case A(0)-N0	40
2.3.3 Case A(i)-N0: Different Charge state of the atom	40
2.3.4 Case A(i)-Nj: Isomeric Triggering, and how this motivates the work	42
2.3.5 Case A(i)-X-Nj: Capture that produces an excited atomic state	44
2.3.6 X-NEEC: NEEC into an already excited atomic state	45
2.4 Motivation of the Work, Origins of Isomerism and its Importance for NEEC	46

	5
2.4.1	Types of Isomers 48
2.4.2	Motivation to Select Prevalent Isomer Triggering Pathways 48
3	How Much NEEC? 49
3.1	The Generalised NEEC probability 50
3.1.1	Generalised NEEC Probability for a Single Capture Channel - energetic tabulation 50
3.1.2	Cross section and Resonance Fraction - The Narrow Resonance Approximations 54
3.1.3	The Total NEEC Resonance Strength - summing over capture channels introduced 56
3.1.4	The Calculated Resonance Strength 57
3.2	Resonant Flux - Velocity and Density of Collisions 57
3.2.1	The Collision Flux 57
3.2.2	The Energetic Fraction - Probability of a collision at a certain energy 58
3.2.3	The Collision Velocity $v(t, E)$ and Momentum $p(t, E)$ 59
3.2.4	The Ion-Electron Density - $n_{i-e}(t, E)$ 59
3.2.5	Summary of Generalized NEEC Probability - Temporally static equilibrium 60
3.3	The Simple Scenarios 61
3.3.1	A Simple Example - An Electron beam impinging a stationary fully stripped ensemble of ions 61
3.3.2	A Simple Example - An isomeric beam in a storage ring 63
3.3.3	A More Realistic Example - Exposing the best combination of charge states 65
3.4	NEEC Probability for Equilibrium-Plasma and Ion-Beam-Foil Parameters 65
3.4.1	Plasma Rate - Approximately Temporally Static 66
3.4.2	NEEC Yield - Expanding the Parameter Space 68
3.4.3	Quantised Regime of Electron Distribution Function 70
3.4.4	Electron Distribution Function at Equilibrium - Hot Dense but not too dense plasma's - $T_e \gg V_1 $ 72
3.4.5	Cooler Plasmas - $T_e \sim V_1 $ 76

3.4.6	Nuclear Beam Impinging a Thin Solid Target - Temporally dynamic	78
3.4.7	A comment on luminosity	81
3.5	Parameters for the Best Candidate Experiment	83
3.5.1	The Big Data Approach	84
4	Finding a not Knowingly Over-promised NEEC Enviroment	85
4.1	Trends in Nuclear and Atomic Data	86
4.1.1	Atomic Binding Energies - National Institute of Standards and Technology (NIST) Atomic Spectra Database	86
4.1.2	Nuclear Level Data - Evaluated Nuclear Structure Data Files (ENSDF)	89
4.1.3	Nuclear Gamma Ray Data - (ENSDF)	92
4.1.4	Isomer Data - Atlas of Nuclear Isomers	94
4.2	General Search Algorithm with Energetic Constraints	95
4.2.1	Map of the Database Structure	96
4.3	High Powered Laser-Plasma	97
4.3.1	The Hottest-Densest Terrestrial Plasmas	97
4.3.2	Cooler Plasma Results	102
4.4	NEEC Companion Tool	104
4.5	The Stockholm Electron-Beam Ion-Trap - Results	108
4.6	Future Work	111
5	Exploration of the Beam Approach - Channeling Proposal and Developments	112
5.1	Detection Experimental Techniques	113
5.2	Choosing a distinct NEEC Pathway	113
5.2.1	Triggering in a Beam-Foil geometry	113
5.3	Channeling: Selling Points and Theory	114
5.3.1	Cross Section Estimates for Channeling scenario	116
5.4	Optimisation of the ^{84m}Rb experiment at TRIUMF: CouEx and Channeling	117
5.4.1	^{84m}Rb Channeling experimental proposal	118
5.4.2	Experimental Setup	118
5.4.3	Beam Dynamics	121
5.4.4	Setting Up Analysis of Results - Extracting the matrix element and comparing the results with theory	125

6	Conclusions	128
A	Theoretical Computation of Internal Conversion Coefficients	130
B	Original Channeling Proposal Submitted to TRIUMF	131
C	PRL: First Direct Measurement of an Astrophysical p-Process Reaction Cross Section Using a Radioactive Ion Beam	140
D	Progress Report for Rb Channeling Experiment at TRIUMF	147
	Bibliography	152

Acknowledgements

I would firstly like to express my deep gratitude towards my supervisors, David Jenkins and Chris Murphy, for their unwavering support throughout this PhD, and for being so patient throughout what has been a long, tumultuous and complex few years.

I would also like to thank my friends at the university York, specifically Ryan, Luke, Chris R, Marcus, Jenny and Mihai and everyone else, for always being there for physics discussions and beverages.

Most of all I would like to thank my parents for putting up with me for so long, and especially for being so supportive in the most difficult and dark times during the last few years.

Declaration

I declare that this thesis is a presentation of original work and I am the sole author. The experimental proposal and progress report (attached in the appendices) were written in collaboration with Prof David Jenkins and Dr Chris Murphy, and submitted to the Nuclear Physics Experiments Evaluation Committee at TRIUMF Canada in 2019 and 2022. This work has not previously been presented for an award at this, or any other, University. All sources are acknowledged as References.

Introduction

Nuclear excitation by the capture of free electrons (NEEC) is an unlikely situation to occur in nature, but if it is realised, it is powerful in a way that would have a significant impact on energy storage technology and nuclear astrophysics.

Nuclear Excitation by Electron Capture (NEEC) was first proposed in 1976 by Goldanskii and Namiot [1] in which it was asserted that there is an inverse process to internal conversion (IC); where the nucleus becomes more energetic (excited) when capturing a free electron into the surrounding electron cloud. NEEC was considered to have limitations due to the availability of open electron shells, and we examine in this thesis if this is a significant problem.

Internal conversion (IC) exists, where an excited nucleus can eject an atomic electron to the continuum, rather than decaying via gamma emission.

Both processes must occur at some kind of equilibrium in the universe so long as there is a consistent reversibility argument, and the right conditions can be created.

We remind ourselves here of the scale of physics in this energetic realm, a nuclear excitation is typically $\sim 1\text{MeV}$ yet an (energetic) atomic transition is $\sim 1\text{eV}$. So clearly we are looking at low energy nuclear transitions and energetic atomic transitions with an overlapping boundary, and many orders of magnitude at play.

If the smaller energetic system is able to directly influence the larger, through macroscopic parameters, then one could release a reasonable amount of nuclear energy, by influencing the smaller energetic system, vastly changing the timescale of the nuclear relaxation.

This continues to be highly topical in current literature, especially since NEEC is relevant in both nuclear astrophysics and high energy-density transportable power sources. One must be adept in finding the best nuclear transitions that can couple well with the atomic wavefunctions, and macroscopic ion-electron collision controls, in order to advance. The inverse process (IC) is well understood, and can provide a useful insight into

finding the right kind of nuclear-atomic couplings.

We are limited by the principle of detailed balance (PDB) [2] [3] in being able to reverse a process; which says that (paraphrasing) "corresponding to every individual [microscopic] process there is a reverse process, and in a state of equilibrium the average rate of every process is equal to the average rate of its reverse process." [4]. It is difficult of course to produce an environment where a nuclear process is at equilibrium with its inverse process, as this is extremely unlikely in an entropic sense, however we can use reversibility, which arrives from the principle of detailed balance, allowing us to make theoretical shortcuts. Nonetheless it is also notable that a detailed balance of nuclear processes ferments the production of observable matter [in nuclear astrophysics].

To produce this equilibrium requires entirely non-terrestrial (or Astrophysical) scenarios and time-frames [5], inaccessible by last century's high power Laser-Plasmas, with such viable environments only just coming into fruition.

Theoretically, and notwithstanding, is the complication of the coupling between the immensely complex nucleus *and* the atomic electrons, and then representing and calculating this situation accurately *ab initio*. One is reminded of Godel's incompleteness theorem when considering such a profound scale change; in which it is implied universally that everything is either incomplete or inconsistent.

We will see that the nucleus quite easily emits energy as it wishes, but to excite the nucleus in a precise way via the inverse process, or any process, is very difficult. De-excitation is a natural process since the emitted products can go anywhere as entropy increases and the energy dissipates; excitation conversely requires a lot of control since we are trying to introduce order on a much smaller scale. We cannot define analytically the expression of a varying number of interacting sub-systems on this scale (typically nuclear dynamics are extremely complex and hard to compute *ab initio* even with today's computing power, however electron dynamics are accurately yet incompletely approximated using the Multi-Configuration Dirac-Fock method). We will avoid getting lost in such algebra as it is the experimentalist's role to observe how nature is, and then use these observations to predict further behaviour. This thesis essentially presents a regularisation on our ability to control the nuclear system via atomic parameters.

Repeatable observations of NEEC has been a longstanding goal in atomic and nuclear

physics, and with a road-map in mind, one can outline a critical path towards readily producing observations. The originality comes from the inclusion of all possible species and scenarios. It is understood a connection needs to be made between the different experimental approaches in order to readily challenge theory in parallel with separating the many different nuclear excitation techniques. The race is certainly on to produce further observations, yet for this to be productive, one must be systematic and meticulous, without getting lost in the inevitable complexity of the subsystems and experimental mechanics.

The structure of this thesis then is as follows:

Chapter 1 and 2 Introduces and confines the concepts of eigenstates and transitions, and resonant interactions in-between them. The NEEC resonance strength is defined as a result, via the principle of detailed balance.

Chapter 3 allows us to count the upper limit NEEC rate and yield, and we check our theoretical technique by calculating rates with *ab initio* data.

Chapter 4 is an encompassing search over all elements and nuclides to find the most promising candidates that are constrained by the maximal available macroscopically adjustable parameters for each experimental approach, limited by the principle of detailed balance.

Chapter 5 Is the optimisation of a beam experiment based on ^{84m}Rb at TRIUMF, for which we have composed and had accepted an experimental proposal. This chapter will be made as useful as possible for the final planning and execution of this experiment, although it has received the least attention due to the prospect of many years of COVID restrictions ahead.

First we will summarize the necessary background, but mainly we will establish an infallible method.

Chapter 1

Background and Theory

We begin our examination of NEEC by introducing the necessary background in quantum mechanics. This will allow us to define the current state-of-the-art in NEEC theoretical calculation, and also make some generalisations that will allow us to speed up calculating NEEC rates.

One only knows truly what has been observed in nature, and we hope to use experimental database's as a way to circumvent theoretical complications and complexities and computational limits which are described in this chapter. No doubt internal-conversion (IC) is a good place to start in ascertaining a natural understanding of the NEEC process, since IC has been well observed and well tabulated, to a similar extent as gamma-decay. Understanding an inverse process surely enlightens our knowledge of the forward process but introduces limitations, which we will assess in chapter 2.

1.1

Internal Conversion

Internal Conversion (IC) is a prevalent process in nuclear physics in which an excited nucleus, instead of emitting a gamma ray, transfers its energy to an orbiting electron, ejecting it into the continuum with residual kinetic energy E_{res} . The exit channel (right hand side) of this interaction is readily observed, due to the energy balance

$$Q - |Vi| = E_{res} \tag{1.1a}$$

$$\text{Energy excess from deexcitation} = \text{Residual electron kinetic energy} \tag{1.1b}$$

which requires the change in energy of the nucleus Q is greater than the magnitude of the electron binding energy $|V_i|$. As is evident in 1.1, the difference in energy between the bound and un-bound systems is carried away as kinetic energy of the free electron. The range of available states in the continuum does not restrict the probability of de-excitation, and thus this process is readily observed. The ejected electron can take any momentum and energy value, as the continuum is indifferent to what momentum state it can take, unless the continuum is extraordinarily dense. The IC coefficient (ICC) is defined explicitly as

$$\alpha = \frac{A_{IC}}{A_r} \quad (1.2)$$

which is the IC rate A_{IC} divided by the the gamma emission rate A_r , i.e. this ratio defines how many internal conversions occur (s^{-1}) for every gamma decay. A_r will be defined shortly. There are limitations in computing theoretically the IC coefficient, largely due to approximations in computing the many-body Breit interaction (approximating the electron wavefunctions) [6] or approximations due to nuclear structure and non-sphericity [7]. A useful summary of the IC theory in order to calculate the IC coefficient via interpolation of experimental data is available in [6]. Where interpolation is not possible or feasible, theoretical models are used via the frozen orbital approximation. Uncertainties in calculating ICC's theoretically have been minimised and characterised by comparing to experimental data, and recalculating wavefunctions for ICC's under extrapolated physical conditions [7], starting with an increasingly intelligent trial wavefunction. Theoretical ICC's are assessed to be within an accuracy of 5% or better [8].

The total IC coefficient α_{tot} can be decomposed into constituent contributions depending on the atomic principal quantum number \mathbf{n} ($K \Rightarrow n=1$, $L \Rightarrow n=2$, etc)¹. The partial IC coefficients for atomic sub-shells are additive, as are their total probability amplitudes which overlap the nucleus [6].

¹The nomenclature here stems from the first atomic spectral observations being due to early measurements by Kamen and Lyman (and the principal quantum number labels carried on down the alphabet from there). Each shell is split into its subshell's numerically (L1,L2,L3 etc.). This is an annoying simplification by atomic spectroscopist's, as although quicker to notate, one isn't informed about a subshell's angular momentum quantum numbers without a conversion table.

$$\alpha_{tot} = \alpha_K + \alpha_L + \alpha_M + \dots = \sum_n \alpha_n \quad (1.3)$$

The primary/principle atomic contributions can be further decomposed into spin-orbit shell contributions where appropriate, obeying the rules of Slater determinants [9]; for example, for the L atomic shell, there are three possible j quantum numbers which cause a noticeable variation in the L shell IC coefficients (ICC's) across the subshell.

$$\alpha_L = \alpha_{L1} + \alpha_{L2} + \alpha_{L3} \quad (1.4)$$

i.e. the contributions of neutral atom subshell ICC's are associative and their configuration determined by the diagonal of the atom's Slater determinant (described in the next section).

The IC coefficients are well observed for most nuclear transitions that obey equation 1.1, so neutral subshell constituents are well tabulated. It gets more difficult to resolve internal conversion spectra for spin-orbit splitting that takes into account pairing terms within a subshell with a large ($n > 2$) principal quantum number (eg. any M shell; or O1, O2, O3, O4, O5 subshell etc.) for heavy ions [10]. So IC coefficients are generally only tabulated in terms of their atomic principle quantum number and, if possible, constituent subshells. We use the program BrIcc[6] in later chapters in order to calculate ICC's. BrIcc calculates ICC's using the frozen orbital approximation, or where appropriate by interpolating experimentally observed values [6].

The proper ICC value for an atomic charge state will require adjustments from the values produced via BrIcc (which is for neutral atoms) due to three factors:

- Subshell occupancy adjustment. We must account for partially filled shells by multiplying the filled partial subshell ICC by the fraction of total unoccupation: i.e., $\frac{n_h}{n_{max}}$, where n_h is the number of vacancies as a fraction of the total number of vacancies n_{max} within the subshell [11].
- Charge state adjustment. The ICC for a valence electron orbital in an ion can vary up to 40% when compared to the same electron in a neutral atom [12]. We multiply by the ratio of the valence electron ionisation energy to the associated neutral atom binding energy [11]

- Excited state adjustment. When capturing into excited states, ICC's are not tabulated, although by over-scaling the inner shell ICC's we propose in chapter 2 and 3 that this fully accounts for possible excited state ICC's.

To calculate NEEC rates it is important to include a three step process to account for a detailed balance that involves photons *and* electrons². Depending on what part of the nuclear decay sequence one wants to detect, one has to include the relevant branching ratios, which will be discussed in chapter 2. This is essentially a 'rare' resonance followed by a 'difficult to detect' deexcitation. To be rigorous, we now define stationary states of the atom and its nucleus and define strengths of transitions between these states, in order to define a complete picture of a NEEC resonance channel which can be expanded into an overall NEEC rate in an environment. We first include the theory to evaluate the NEEC rate per ion, and then expand this into a figure of merit which includes an effective ion-electron density.

1.2

Energy Levels - Defining the Stationary States in the Atom and Nucleus

One quickly discovers that there are stationary states of a quantum mechanical system when finding solutions to the time-independent Schrodinger equation. This defines the energy levels of the system, from which one can gain information about the microscopic structure of an atom as a theorist.

Stationary states emerge in both the nuclear and atomic systems via the application of an appropriate Hamiltonian and state-vector (wave-function) in nuclear and electron sub-spaces separately³.

The time-dependant Schrodinger equation is defined as

$$i\hbar \frac{d\Psi}{dt} = H\Psi \quad (1.5)$$

where the statefunction Ψ has a time-independent eigenvector ϕ with $\Psi = \phi e^{-i\omega t}$, and the Schrodinger equation simplifies to the time-independent Schrodinger equation

²we account for this by using a non-local thermodynamic equilibrium in chapter 3

³although electronic energy eigenvalues do depend partly on the charge of the nucleus

$$H\phi = E_{nl}\phi \quad (1.6)$$

This is known as an eigenvalue equation, where the eigenvalues are the energies (E_{nl}) of the system of bound fermions. One methodically approximates the energy operator H , so that the wave equation 1.6 reproduces realistic values of the energies of the system. One also formulates a functional structure of ϕ so that its square amplitude physically defines the probability of a fermion appearing somewhere in the region of an appropriately chosen coordinate system.

One is reminded of wave-particle duality here which is essential in quantum mechanics, particles become non-local and behave as waves, pertinently in the scenario where their wavefunction is in a strong potential or confined or both.

When a fermion is in a spherical potential there emerges a separable distinction between the radial and angular parts of the wavefunction [13].

$$\phi(q) = \frac{1}{r}P(nl;r)Y_{lm_l}\chi_{m_s}(\sigma) \quad (1.7)$$

where q defines a multi-index for the space and spin coordinates.

This allows us the definition of a spin-orbital, which is defined by a specific value of the principle quantum number n , and orbital angular momentum quantum number l [13].

We know very little about ϕ throughout this work, but we know as much as possible about all possible energy eigenvalues E_{nl} through experimental data or through state-of-the-art theoretical calculation which are tabulated in a database. We explore the general form of the Hamiltonian for the atomic and nuclear systems separately in the next subsections. In the same manner as equation 1.6, there are several other eigenvalue equations whose operators commute with the Hamiltonian. This means that there are several simultaneous operators with which the Hamiltonian is invariant when applied to the wave-function, these will be discussed in the next sections. Essentially, for the nuclear and atomic systems, there are 'good' quantum numbers, whose eigenvectors are orthogonal, and which simultaneously define its eigenstate, along with its energy.

Eigenstates of both the nucleus and electron cloud follow the same basic rules [13] [14]:

- Pauli exclusion principle - no two fermions can occupy the same quantum state (configuration).
- Spin-orbitals - the quantum state of the fermions will be defined via spin-orbitals if the potential is spherically symmetric. A fully occupied spin-orbital will contribute zero angular momentum to the system.
- Aufbau principle - fermions added to the bound system will occupy the lowest energy available quantum state and minimise the interaction energy by filling the least occupied spin-orbital (Hunds rule).
- Computationally solving the time independent Schrodinger equation is futile without a central field or effective field approximation.

The Hamiltonian operator of an eigenvalue spectrum depends on both the atomic system and quantum mechanical formalism; the normal starting point is Schrodinger's time-independent equation, but many approximations have to be made in choosing an appropriate wavefunction and many-body potential in the Hamiltonian [15]. In the next section we derive the necessary theory to understand a proper labelling of the nuclear and electronic energy eigenvalues, so we can evaluate the probability of transitions between them. An important point to remember is that these states have a well defined angular momentum and the angular momentum operators invariably commute with the Hamiltonian

$$[H, J^2] = [H, J_z] = 0 \quad (1.8)$$

1.2.1 Atom Energy Levels

Essentially the NEEC problem is an atomic one, so long as the nuclear aspects remain only PT invariant as described in chapter 2. As such, we focus much of our theoretical attention on the atomic perspective.

The simple 1 electron Hamiltonian is written as

$$H_{1e^-} = -\frac{1}{2}\nabla^2 - \frac{Z}{r} \quad (1.9)$$

where there is a kinetic energy term and an attractive potential term between the electron and the nucleus. The one electron wavefunction has the form of 1.7. Each energy state is described purely by the principle quantum number n and angular momentum quantum number l and so there are degenerate spin-orbitals for each subshell and degenerate subshells in each shell. This degeneracy is lifted once the many electron Hamiltonian is applied, and each subshell contains these spin-orbits resulting in the configuration label $\underline{\alpha} := nlm_l m_s$. A shell thus describes quantum states with the same n , and a subshell describes quantum state with the same n, l , and j and a spin-orbital describes a quantum states with the same n, l, m_l and m_s .

j is the total angular momentum of an electron and can take the values $|l + s| \dots |l - s|$. The magnetic projections m_l and m_s can cause a splitting in a subshell.

Contributions that define the many electron energy eigenvalues are defined in the atomic Hamiltonian [13]

$$H_{atomic} = \sum_i H_{1e^-} + H_{res} + H_{SO} \quad (1.10a)$$

$$= - \sum_{i=1}^N \left(-\frac{1}{2} \nabla^2 - \frac{Z}{r_i} \right) + \sum_{j>i}^N \sum_{i=1}^N \frac{1}{r_{ij}} + \sum_{i=1}^N \xi_i(r_i) (l_i \cdot s_i) \quad (1.10b)$$

where the Hamiltonian contains a single electron Hamiltonian for each electron along with a residual term H_{res} (describing many-body electron repulsion) and a spin-orbit term H_{SO} describing the interaction between the orbital and intrinsic angular momentum of any unpaired electrons. The importance of these terms are paramount when calculating the electronic excitation spectrum of the atom as they determine the extent of coupling between unpaired electrons. They are of less importance in calculating the ground state energies of the atom, as (in general) all electrons except the valence electron are in closed shells.

The many electron wavefunction ϕ_{atom} can be seen as similar to a product of all the possible 1e- wavefunctions (so long as residual and spin-orbit interactions are ignored), although this would not preserve the anti-symmetry of the fermionic statefunction.

The actual many electron wavefunction requires a matrix formulation of quantum mechanics along with a central field approximation to allow for the many-body interactions in equation 1.10 [13] and to preserve the wavefunction anti-symmetry. Slater determinants are used to represent the many electron statefunction, which when combined with the many electron Hamiltonian allows for 2 dimensional permutations of coordinates of the electrons. Slater determinants are insufficient on their own to account for all permutations of electron coordinates in describing the full many electron eigenvalue spectrum; linear combinations of Slater determinants are required to describe a configuration state-function (CSF). There is no general way of defining CSF's across the periodic table of elements, without the use of machine learning techniques that are just coming into fruition [16].

$$\phi_{atom} = \phi(\mathbf{q}_1, \dots, \mathbf{q}_N) = \frac{1}{\sqrt{N!}} \begin{vmatrix} \phi(\alpha_1, q_1) & \phi(\alpha_1, q_2) & \phi(\alpha_1, q_3) & \dots & \phi(\alpha_1, q_N) \\ \phi(\alpha_2, q_1) & \phi(\alpha_2, q_2) & \phi(\alpha_2, q_3) & \dots & \phi(\alpha_2, q_N) \\ \vdots & \vdots & \vdots & & \vdots \\ \phi(\alpha_N, q_1) & \phi(\alpha_N, q_2) & \phi(\alpha_N, q_3) & \dots & \phi(\alpha_N, q_N) \end{vmatrix} \quad (1.11)$$

where \mathbf{q}_i describes the space and spin coordinates and α_i describes the spin-orbital configuration. The hydrogenic configuration of this determinant using a $1e^-$ Hamiltonian would only require the diagonal of this matrix as a product wavefunction.

$$1s2s2p3s3p3d4s4p4d4f5s5p5d5f5g6s6p6d6f6g6h7s\dots \quad (1.12)$$

This would describe the state of a many electron atom with a $1e^-$ Hamiltonian, i.e. the electrons are not interacting. Although this is unphysical in itself, this labelling is used to describe the closed shell configuration of any atom, since electrons in closed shells are considered inert other than their screening effect on the nuclear charge [13].

To this end, we make approximations using averages in the angular momentum eigenvalue in this work, which uses hydrogenic configuration labelling, in order to speed up the theoretical process. Averages are taken, especially in energies and many electron wave-functions (configurations) by adopting this hydrogenic labelling for the valence

NEEC resonance channel, labelling it $p = \{n, l, j\}$, with $j = l + s$ the total electron angular momentum of the valence electron in its hydrogenic configuration, and α_p the internal conversion coefficient in this configuration. We examine the impact of this, along with appropriately scaling α_p , comparing the resonance strength to a fully *ab initio* dataset in chapter 2 and 3.

Atomic ground states are defined by their lowest available energy eigenvalue due to a certain number of bound electrons, i.e. the lowest energy (highest binding energy), of the vacant spin-orbitals. Considering this energy w.r.t. a continuum, or zero energy, this allows the definition

$$E_{bind} = -V_i = |V_i| \quad (1.13)$$

where V_i is inherently negative compared to the zero energy; energies above zero will be kinetic and energies below zero will be potential.

1.2.2 Nuclear Energy Levels

In the nuclear system the Hamiltonian is described in a similar manner

$$H_n = \sum_{i=1}^A \left(-\frac{\hbar^2}{2m} \nabla_i^2 \right) + \sum_{i < j}^A (V_{coulomb}(i, j) + V_{strong}(i, j)) \quad (1.14)$$

where we have an independent particle part due to the kinetic energy of each nucleon, and a residual part to include many-body forces between nucleons [17]. The potential terms in the Hamiltonian are described by electromagnetic and strong nuclear interactions between each particle and all other particles along with permutations of many-body forces. For nuclear systems where $N > 4$ this is extremely difficult to compute in its entirety (*ab initio*) [18] and effective theories have to be employed, such as mean field theories, chiral effective theories or in heavier nuclei, density functionals.

Symmetries emerge when the nucleus is spherical. This allows the definition the commuting operators [9]:

$$[H, P] = [H, J^2] = [H, J_z] = [H, N] = [H, \Pi] = 0 \quad (1.15)$$

where P is the centre of mass momentum vector, J^2 and J_z are the total angular momentum operators, N the particle number operator and Π the parity operator. In a spherical nucleus we can describe the emergence of a shell model, with the nucleons moving in a mean field generated by all other nucleons, which has spin-orbit terms, similar to the atomic Hamiltonian [10]. A collective Hamiltonian can be defined when the structure of this core of nucleons changes its mode of oscillation via phonon's. Typically NEEC rates are only known to be calculated using these collective Hamiltonians.

$$H_n = \sum_{\lambda\mu} \Omega_\lambda B_{\lambda\mu}^\dagger B_{\lambda\mu} \quad (1.16)$$

where Ω_λ are the phonon frequencies, and $B_{\lambda\mu}^\dagger$ is the phonon creation operator [19].

So long as the electromagnetic transition decay rate is known for a nuclear transition, then we can assess its tendency to internally convert and as such, NEEC, in a model independent fashion.

1.2.3 Transition Multipolarity and Mixing - Nuclear

Gamma decay and internal conversion are electromagnetic processes that are strongly affected by the multipolarity of a nuclear transition. The multipolarity defines generally the change in the charge distribution of protons within the nucleus (E - electric), or the change in currents caused by the change in motion of the protons (M - magnetic). An electromagnetic nuclear transition is thus the redistribution of the Z protons, and their motion, in order to arrive at a lower (or inversely NEEC excited) energy state. Of course, proton and neutron numbers are conserved in such transitions and so the nucleus stays of the same type.

This classification via multipolarity of nuclear electromagnetic decay arrives from the semi-classical theory of radiation [20], and relies on conservation in the first of the axioms defined on page 17. A direct result of this proton redistribution in the decay is that the neutrons reorganise themselves, to minimise their interaction potential, generally in the strong field. We assert that the movement and location of the neutrons in an electromagnetic decay is irrelevant in this analysis, other than to define the nuclear excitation spectrum eigenvalues. In gamma decay the radiation is carried away with L quantized units of angular momentum, which is the difference in angular momentum between the

two quantized states of the nucleus. The resulting boson is called a photon. For example; $L=1$ dipole radiation is the spatial oscillation of the resulting EM field distribution caused by charge oscillating on a 2D line during the decay, causing a distribution in intensity of the emitted radiation that peaks twice in the angular distribution, due to the new spatial configuration of protons. There are higher order moments of this action that can result in quadrupole (E2), octupole (E3) etc. radiation fields, defined by the angular momentum change of the transition $= 2^L$.

There can however be a mixture of contributions due to the complex reordering of these motions, dictated by selection rules. Clearly the change in state of protons can be a mixture of their new movement and new position within the nucleus w.r.t. the motion of surrounding nucleons, and quantum mechanics makes this highly discrete if using an appropriate approximation in perturbation theory. The change in spin and parity of the nuclear state can take diminishing multipole types as the order of perturbation increases i.e.

$$|J_i - J_f| \leq L \leq |J_i + J_f| \quad (1.17)$$

The mixing ratio for an electromagnetic nuclear transition is defined as

$$\delta(\pi' L' / \pi L) = \frac{A_r(\pi' L')}{A_r(\pi L)} \quad (1.18)$$

where for two type mixing $L' = L + 1$ and π' is the multipolarity of the opposite type in table 1.1 [6]. The total radiative transition rate for a mixed transition is thus defined most accurately by using the electromagnetic decay rates defined for a known mixing ratio in equation 1.18.

Similarly the IC coefficient can also be defined for a non-zero mixing ratio:

$$\alpha = \frac{\alpha(\pi L) + \delta^2 \alpha(\pi' L')}{1 + \delta^2} \quad (1.19)$$

For a transition such as the deexcitation of the first excited state $J^\pi = \frac{3}{2}^-$, to the ground state $J^\pi = \frac{1}{2}^-$ in ^{57}Fe ; using equation 1.17, $1 \leq L \leq 2$. Hence there will be an $L = 1$ (M1) component and a smaller $L = 2$ (E2) component, and a vanishingly small M3

TABLE 1.1: Allowed mixing types, table from [6] $\Delta\pi = -1$ implies a change in parity

	$\Delta\pi = +1$			$\Delta\pi = -1$	
πL	M1	M1	M3	E1	E3
$\pi' L'$	E2	E2	E4	M2	M4
$\pi'' L''$	M3	E0	M5	E3	E5

component, by using table 1.1. Notably then

$$J_i = J_f + L \quad (1.20)$$

1.2.4 Transition Rates

When evaluating the transitions between stationary states, the time-dependant Schrodinger equation must be used. This manifests the requirement for an additional interaction term in the Hamiltonian, H' .

The transition probability (per unit time) between two eigenstates of an interaction Hamiltonian is expressed using first-order Dirac perturbation theory (also known as Fermi's golden rule) [14]⁴:

$$P^{i \rightarrow f} = \frac{2\pi}{\hbar} |\langle f | H' | i \rangle|^2 g(E_f) \quad (1.21)$$

where $g(E_f)$ is the final density of states. The basis $|i\rangle$ is the the action on the overall nuclear wavefunction $|i\rangle = |\psi_i\rangle |\dots n_\lambda \dots\rangle = |\psi_f\rangle |\dots n_\lambda + 1 \dots\rangle = |f\rangle$ for the creation of photons due to its decay.

Overall, using 1.21, one can evaluate the lifetime of a nuclear state electromagnetically [21] by using Weisskopf estimates for the reduced transition probability, and scaling by a factor in Weisskopf units. This avoids the difficulty in units conversion, so long as one has a table of Weisskopf estimates for the different multiplicities [14]. The lifetime via the Wigner-Eckhart (W-E) theorem is strongly dependant on the transition energy and matrix element of the transition.

⁴see appendix B4 in ref [14]

$$T^{i \rightarrow f} \propto |\langle f | T_\lambda | i \rangle|^2 / (\Delta E)^{2\lambda+1} \quad (1.22)$$

where T_λ is the electromagnetic transition operator. The transition rate depends then on the reduced transition probability using the transition operator matrix element. Which via orthonormality, can be expressed in terms of the matrix element of the electromagnetic operator between nuclear spin states:

$$B_{(M)\lambda, J_i \rightarrow J_f}^{(E)} = \frac{1}{2J_i + 1} |\langle J_f | T_\lambda^{(E)\lambda} | J_i \rangle|^2 \quad (1.23)$$

Via W-E, we can assert that the radiative transition rate of an unstable nuclear level is expressed as follows

$$A_r = \frac{8\pi(L+1)}{L((2L+1)!!)^2} \frac{Q^{2L+1}}{c} B_{(M)\lambda, J_i \rightarrow J_f}^{(E)} \quad (1.24)$$

This is our link between the quantum mechanical nature of the nuclear transition, and a macroscopically calculable excitation / decay rate. All of the nuclear parameters are contained within equations 1.23 and 1.24, and as long as we know the reduced transition probability ("B-value") then we can assess the nuclear transition rate between a two level nuclear system in a model independent fashion. B-value's are tabulated in the ENSDF database.

Normally an unstable system decays and emits its energy easily. In the reverse, of course the energy must be matched almost exactly to the energy of the transition, and this is commonly referred to as a resonance, but in our case, the resonance is inducing an ordered effect on a diminishingly small scale, from a macroscopic one, so one would expect the reverse of entropy to dictate the probability of this to be diminishingly small.

1.2.5 Transitions from the Electron Continuum

In 2006 the most detailed NEEC theoretical formalism was published by A. Pálffy et al [12], using the Feshback formalism, which arrives from the theory of dielectronic recombination (DR)⁵. As the nuclear analogue of DR, NEEC has an intermediate state of an excited nucleus, and so one must account for the photonic state as an extra subspace

⁵Excess energy from electron capture resonantly excites another electron

within the basis. In this formalism, projectors are defined between each of the electronic, nuclear, and photonic, subspaces and a completeness relation postulated:

$$P = \int d\varepsilon \sum_{\underline{\alpha}} |\underline{\alpha}\varepsilon\rangle \langle \underline{\alpha}\varepsilon| \quad (1.25a)$$

$$Q = \sum_q |q\rangle \langle q| \quad (1.25b)$$

$$R = \sum_q \sum_{\underline{k}\sigma} a_{\underline{k}\sigma}^\dagger |q\rangle \langle q| a_{\underline{k}\sigma} \quad (1.25c)$$

where $a_{\underline{k}\sigma}^\dagger$ is the photon creation operator, $\underline{\alpha}$ in this case is a multi-index used to represent the spin-orbital atomic quantum numbers, q is a multi-index to describe a newly bound electron and excited nucleus and ε is the kinetic energy of the electron being captured from the continuum.

In essence the postulate that the sum of the subspace projections in the Fock space $P + Q + R = 1$ in [12] may not provide the appropriate completeness to analyse atomic induced depletion scenarios, and although extra terms (such as electroweak interaction), should be analysed, the tools in this thesis at least can provide a yardstick for purpose of the extension of this theoretical postulate.

Some of the original NEEC theorists, in the early 2000s, initially proposed a simpler structure for the NEEC and IC rate using only the bound and continuum electronic wavefunctions and a two level nuclear system [5], which allows the use of Fermi's golden rule:

$$\lambda_{NEEC} = \frac{2\pi}{\hbar} |\langle \psi_f \phi_b | H' | \psi_i \phi_c \rangle|^2 \rho_b(E_b) \quad (1.26)$$

and similarly

$$\lambda_{IC} = \frac{2\pi}{\hbar} |\langle \psi_i \phi_c | H' | \psi_f \phi_b \rangle|^2 \rho_c(E_c) \quad (1.27)$$

with ρ_b and ρ_c the bound and continuum density of states respectively, ψ the nuclear statefunction and ϕ the electron statefunction. Essentially, the rate of IC and NEEC would be at a detailed balance if the Boltzmann relation holds:

$$\frac{\lambda_{NEEC}}{\lambda_{IC}} = \frac{2J_f + 1}{2J_i + 1} e^{Q/T_e} \quad (1.28)$$

The validity of this statement is examined in chapters 2 and 3, and we hope to answer the question as to the astrophysical conditions where this could occur.

Chapter 2

NEEC Resonance Strength

With NEEC being a resonance, one must understand the origins of such phenomena, and how they affect the equilibrium of a system which involves a plethora of interactions and final states, as entropy increases naturally. More unnaturally or perhaps, *unlikely*, IC and NEEC might exist in an equilibrium and be tilted in the reverse from an equilibrium where the rate of NEEC briefly outweighs the rate of IC, and the entropy could be forced to decrease. It is surmised in chapter 4 that the conditions required for a NEEC/IC equilibrium are non-terrestrial, and for NEEC to be observable terrestrially we must fine tune our conditions so NEEC may occur statistically. This said, assuming NEEC and IC could be at an equilibrium, then this allows us to put an upper limit on the quantum mechanical NEEC rate, which via the principle of detailed balance allows us to define a quantum mechanical reciprocity relation [3]:

$$w(i \rightarrow f) = w(f \rightarrow i) \quad (2.1)$$

where w is the microscopic rate of some quantum mechanical process.

This argument can be extended to the scattering matrices S_{if} and S_{fi} [3], which equate when the forward and reverse reactions are averaged by the total magnetic spin multiplicity of the quantum states available

$$\frac{1}{g_f g_i} |S_{if}^2| = \frac{1}{g_i g_f} |S_{fi}^2| \quad (2.2)$$

where the multiplicities g are defined as $2J + 1$, which counts the total m_J projections, where J is the total angular momentum quantum number. This relationship is implicit to

equation 1.23.

Internal conversion is known to be entirely electromagnetic in nature [6], so to make assumptions about its inverse, we rely on two main axioms of particle physics in the electromagnetic regime.

- Translational and rotational invariance (that is, conservation of linear and angular momentum)
- Symmetry in parity and time-reversal (PT-symmetry... a reaction behaves the inverse way in reverse and obeys spatial symmetry).

We are essentially using a particle physics perspective to treat ions as massive particles which obey the above two axioms and exhibit internal conversion and γ decay.

One of the main requirements of this thesis is to lay out a method for constructing viable experiments which could observe NEEC. Based on the single "observation" [22] that has occurred, the method proposed is more robust via brute-force elimination and provides a grounding for the future of observing the process. We stand in the middle of the theoretical and experimental perspectives and try and engineer a connection between the two, hoping the rate of useful NEEC experimental proposals increases. Similarly we are able to advise, via this method, candidate systems that are in need of further theoretical study to get the maximum NEEC rate out of an environment.

One only knows truly what has been observed in nature, and we hope to use this as a way to circumvent theoretical complications and complexities and computational limits. No doubt internal-conversion is a good place to start in ascertaining a natural understanding of NEEC/IC balance, since IC has been well observed and well tabulated, to a similar extent as gamma-decay.

On the nuclear and hadron scale there could be some significant asymmetries in time reversal if not considering the the above axioms correctly. Significantly, to use the PDB the continuum electrons must not be polarized [3], and even more pressingly the interaction must not exhibit interactions that are also CPT invariant [20]. Effectively here, one assumes there is no electro-weak component to this inverse decay.

2.1

Resonances

We review in this section the concept of resonance, purely as an introduction. The analogy used should not be used to infer anything other than an understanding of resonant systems and the shape of a resonant curve.

A resonance in nature occurs frequently, and is observed in systems that involve vibrations. Technically one can consider a resonant system when a driving force is at the resonant frequency of an oscillatory system that has a restoring force back to equilibrium. A good example is when a pendulum is pushed towards the center at its maxima ($v=0$) at every instant this occurs (i.e. at the correct frequency), and thus it is driven into resonance. The frequency of this driving force must match the natural frequency of the resonant state; in this case defined by the length and mass of the pendulum, the frequency at which there is never any net resistance to driving the system back to the center. Evidently then there is a well defined frequency ω_0 that such a driving force can induce a resonance on a pendulum, and one can extend this example to all systems that are resonant [23]. One must make a distinction here, the difference between the forced frequency and the natural frequency of a driven resonant system. A system reaches its maximum amplitude at the natural frequency, and close to this frequency the system is still driven, but to a much lesser extent. The amplitude, or 'response', of such a system is characterised by the response function

$$Response \propto \frac{f}{(\omega - \omega_0)^2 + (\Delta\omega/2)^2} \quad (2.3)$$

with f referred to as the oscillator strength; the strength at which the driving force affects the oscillator to a maximum extent. The driving frequency ω and natural frequency ω_0 of the oscillator can mismatch slightly, but the response will be reduced. The damping $\Delta\omega$ is the frequency range for which the response drops to half its maximum, indicated in figure 2.1.

Once the driving force is removed, the amplitude of the system will decay exponentially, until the amplitude is $1/e$ of its original value, after the mean lifetime τ . The damping of the system will decay the system to its next lowest energy eigenvalue in quantum

mechanical systems (which with a simple pendulum would be zero energy). The damping is well characterised with macroscopic variables:

$$\text{amplitude} \propto e^{-t/\tau} \quad (2.4)$$

In the pendulum case, the frequency band $\Delta\omega$ is related to the lifetime τ , through the relationship $\Delta\omega = \frac{1}{\tau}$, and is a property of the damping of the resonator (such as friction applied to a pendulum).

There is no doubt that, for an energy conserving set of interacting swings of a pendulum, a larger amplitude will mean a shorter lifetime.

We move quickly away from this analogy, but the concepts remain the same.

In nuclear physics, the resonant cross-section σ ¹ varies just like this oscillator response function, as a function of the center of mass energy of the collision. This is analogous to the amplitude response of a pendulum pushed into resonance. When slightly off resonance, the response is lower than the maximum and falls off sharply

$$\sigma \propto \frac{\Gamma_a \Gamma_b}{(E - E_{res})^2 + (\Gamma/2)^2} \quad (2.5)$$

This is the well known Breit-Wigner formula and accounts for the lineshape (known as a 'Lorentzian' lineshape) of resonant atomic phenomena. The width of the resonant system, Γ is similarly related to the mean lifetime of the resonant state, through the uncertainty principle in quantum mechanics

$$\Gamma \approx \frac{\hbar}{\tau} \quad (2.6)$$

where the analogue of the oscillator strength is $f = \Gamma_a \Gamma_b$ which are derived from the force laws of the resonance interaction, a.k.a. the product of the matrix elements. The total width Γ_{neec} , or *damping* $\Delta\omega$, in this resonant system is composed of widths from nuclear and atomic damping, i.e. it is dictated by the partial widths of all open decay channels in the process

$$\Gamma_{neec} = \Gamma_{nuclear} + \Gamma_{atomic} \quad (2.7)$$

¹a cross section is a viable area of interaction per particle pair which essentially provides a probability when combined with macroscopic experimental conditions

A good way of judging the efficacy of a resonant system is via the resonance strength, also known as the integrated cross-section, in which the effective cross section magnitude is integrated over the continuum electron impact energy distribution function. The cross-section of a resonant reaction varies with the impact energy due to a three parameter Lorentzian, $Lor(E, E_{res}, \Gamma_{neec})$.

$$Lor(E, E_{res}, \Gamma_{neec}) = \frac{\Gamma_{neec}/(2\pi)}{(E - E_{res})^2 + (\Gamma_{neec}/2)^2} \quad (2.8)$$

For brevity, we normally represent this Lorentzian as just $Lor(E, \Gamma_{neec})$ or $Lor(E)$, since the resonance energy and width of a resonance is implicit. Such a function is represented in figure 2.1.

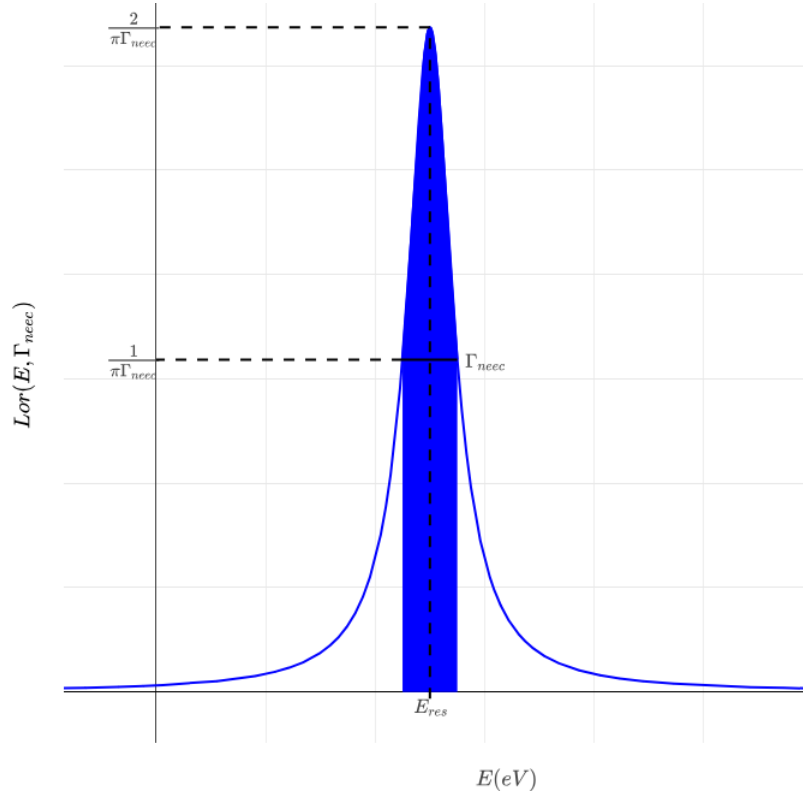


FIGURE 2.1: A Normalised Lorentzian lineshape peaked at the resonance energy E_{res}

2.1.1 Resonance Strength

In this section, and all computations of the resonance strength, atomic units are used. In atomic units, a rate $[\frac{\hbar}{E_h}]$ is equal to an energy width $[E_h]$, where $[E_h]$ is an atomic unit expressed in number of Hartree energies. Once the resonance strength is calculated it is

converted to [beV] and then [$\text{cm}^2 \text{eV}$] allowing subsequent reaction rates to be expressed in SI units.

By definition, the resonance strength is the integral of the cross-section of a resonant interaction, over the collision energy:

$$S = \int \sigma(E) dE \quad (2.9)$$

and at a specific energy one uses the Lorentzian to evaluate the magnitude of the cross-section

$$\sigma(E) = S \text{Lor}(E) \quad (2.10)$$

The resonance strength for NEEC can be calculated according to [12]

$$S = \int \frac{2\pi^2}{p^2} \frac{A_r^{d \rightarrow f} Y_{neec}^{i \rightarrow d}}{\Gamma_d} \text{Lor}(E - E_d) dE \quad (2.11)$$

where $Y_{neec}^{i \rightarrow d}$ is the microscopic NEEC rate, and is calculated *ab initio* by evaluating the product of the probabilities (matrix elements) of the nuclear and atomic subsystems interacting, using overlap integrals of the nuclear and atomic wavefunctions.

For NEEC to be detectable, the excited nuclear level \mathbf{d} must decay electromagnetically, and so this is accounted for in the term $\frac{A_r^{d \rightarrow f}}{\Gamma_d}$ where $\sum_f A_r^{d \rightarrow f} = \Gamma_d$ in atomic units. These terms will be discussed in more detail shortly, especially as a measurable of a NEEC figure of merit (FOM).

In the first instance of a narrow resonance approximation, it is assumed [12], if the resonant nuclear state E_d has a width in the range $10^{-8} - 10^{-5} \text{eV}$, then the electron momentum p and the microscopic NEEC rate $Y_{neec}^{i \rightarrow d}$ can be considered constant. Therefore, the resonance strength can be written as

$$S = \frac{2\pi^2}{p^2} \frac{A_r^{d \rightarrow f}}{\Gamma_d} Y_{neec}^{i \rightarrow d} \quad (2.12)$$

The $\frac{2\pi^2}{p^2}$ term arrives from taking the physical size of the captured particle, it is essentially the area of the electron wavepacket using the deBroglie relation. It is the absolute maximum size the interaction area can take, due to the size of the electron²[24].

²remember we are using atomic units

$$\frac{2\pi^2}{p^2} = \frac{\lambda_e^2}{2} \quad (2.13)$$

where λ_e is the deBroglie wavelength and p is the momentum of the captured resonant electron, which for a resonant collision its required energy is dictated by equation 1.1 and a relativistic energy momentum formula described in section 3.2.3.

The total electromagnetic decay width of the resonant nuclear state is expressed below. The electromagnetic decay rate, equal to the width of the resonant nuclear state (in atomic units), is just the sum of the gamma plus IC decay rates

$$\Gamma_d = \sum_f (A_r^{d \rightarrow f} + A_{IC}^{d \rightarrow f}) \quad (2.14a)$$

$$= \sum_f (A_r^{d \rightarrow f} (1 + \alpha_{tot}^{d \rightarrow f})) \quad (2.14b)$$

Indubitably then one must have an idea of all the final levels, gamma rates and ICC's in order to get a good idea of the measurable NEEC resonance strength

$$\frac{A_r^{d \rightarrow f}}{\Gamma_d} = \frac{A_r^{d \rightarrow f}}{\sum_f A_r^{d \rightarrow f} (1 + \alpha^{d \rightarrow f})} \quad (2.15)$$

where $A_r^{d \rightarrow f}$ is the electromagnetic (EM) transition rate from the resonant state d to the final state f , which depends on the EM decay we chose to observe as a signature of NEEC, and itself can include IC electrons, and so 2.15 is sometimes expressed as unity, assuming one has both electron and photon detectors.

We must define certain computable parameters of the microscopic NEEC environment, to make a link between microscopic and macroscopic, but first we define the resonance strength using the principle of detailed balance.

2.1.2 Resonance Strength from the Principle of Detailed Balance

One can calculate the limit of the size of the resonance strength by using the principle of detailed balance [12], which is a postulate of PT symmetry described above. The microscopic NEEC rate (Y_{neec}) is, at a maximal equilibrium, some statistically weighted fraction

of the IC rate $A_{IC}^{d \rightarrow f}$. Rearranging equation 2.2 we can equate the microscopic NEEC and IC rates:

$$Y_{neec}^{i \rightarrow d} = \frac{(2J_{at} + 1)(2J_d + 1)}{(2J_c + 1)(2J_i + 1)} A_{IC}^{d \rightarrow i} \quad (2.16)$$

where J_{at} is the atomic capture level total angular momentum, and J_i and J_d are the initial and resonant nuclear angular momentum respectively (sometimes referred to as spin and represented with I_i), and J_c is the continuum electron angular momentum that will be captured, and typically $J_c = 0.5$. Thus we can produce an upper limit for the microscopic NEEC rate by estimating the IC rate using the IC coefficient defined above, and the ratios of the multiplicities of the initial and final angular momentum states.

One can use the Wigner-Eckart theorem to evaluate the radiative transition rate A_r , which is formulated based on a theoretical or measured value of *reduced transition probabilities* $B(\pi L)$. This depends on the matrix element of the nuclear transition: the overlap integral of the the two nuclear wavefunctions, as shown in equation 1.23.

So combining 2.16 with 1.2 we have a way of estimating the NEEC resonance strength within an order of magnitude (...or as an absolute upper limit, since one would have to violate PT symmetry to get more than this). The microscopic NEEC rate, using the principle of detailed balance is:

$$Y_{neec}^{i \rightarrow d} = \frac{(2J_d + 1)(2J_{at} + 1)}{2(2J_i + 1)} \alpha_p^{d \rightarrow i} A_r^{d \rightarrow i} \quad (2.17)$$

Overall in our calculations, the NEEC resonance strength is defined as

$$S_{pdb} = \frac{2\pi^2}{p^2} \frac{(2J_d + 1)(2J_{at} + 1)}{2(2J_i + 1)} \alpha_p A_r^{d \rightarrow i} b^{d \rightarrow f} \quad (2.18)$$

where the branching ratio $b^{d \rightarrow f}$ is set at unity if one assumes we can detect every type of decay from the depletion level.

With a view for evaluating a figure of merit of a NEEC environment, when introducing an electron flux on this single resonance channel, arrives the generalised NEEC probability

$$P_{neec}(E) = \frac{N_{neec}(E)}{N_{coll}(E)} = \frac{\int \phi_{res}(\mathbf{E}, \mathbf{t}) \sigma_{neec}(E, t) dt}{N_{coll}(E)} \quad (2.19)$$

where the numerator is the number of NEEC's that occur, and requires a double integral over collision energy and time during the NEEC environment. The demoninator is the total number of electron-ion collisions that could occur.

Over the collision energy explored in the experiment we thus define a time dependant resonance flux, in which a distribution function of impact energies varies over time

$$\phi_{res}(E, t) = n_{coll}(E, t)v(E, t)F(E, t) \quad (2.20)$$

where v is the relative velocity of the ion-electron collision in the COM frame, n_{coll} is the collision density, or can be expressed as an ion-electron density n_{i-e} (an intrinsic property of the experimental system), and $F(E, t)$ is a distribution function of ion-electron collisions that varies over time, such as a Maxwell-Boltzmann distribution or a Gaussian distribution. As already defined, we can remove σ from the energy and time integral, since it is such narrow resonance.

$$N_{neec} = S_{neec}Lor(E_{res}) \int \int \phi_{neec}(\mathbf{E}, \mathbf{t}) dt dE \quad (2.21)$$

We will thoroughly examine the most compact and accurate way of computing the NEEC probability and rate in chapter 3.

2.2

Accuracy of Our Resonance Strength Technique

There were some calculations of the resonance strength for fully stripped ions carried out using the *ab initio* NEEC theory first published in 2006 [12], which provided a microscopic NEEC rate using the Feshback formalism to estimate the overlap integrals (equation 1.25) within the Born approximation. Here we compare these values to calculations using IC coefficients using the PDB prescribed in equation 2.18.

Very recently the accuracy of the PDB method has been improved upon in [11], by suggesting a scaling of neutral ICC's

$$\alpha_p = \left(\frac{|V_i|}{E_b^{q=0}}\right)^a \left(\frac{n_h}{n_{max}}\right)^b \alpha_{IC}^{q=0} \quad (2.22)$$

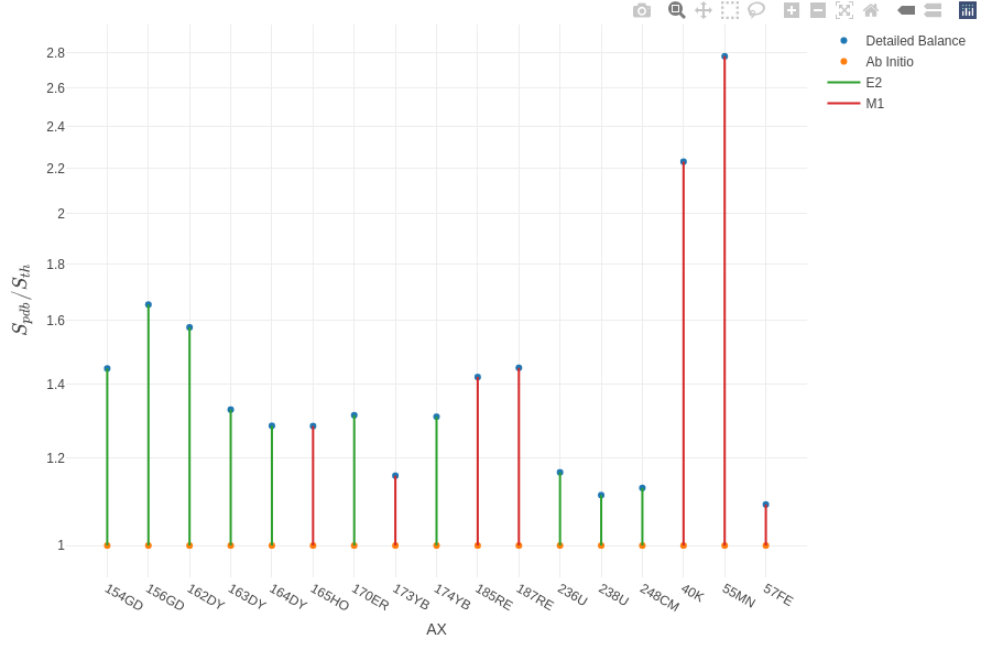


FIGURE 2.2: Comparison of the detailed balance resonance strength to the theoretical calculation using the Feshback formalism by A.Pálffy [12]. This is for capture into the ground state atomic orbital of fully stripped ions

where $a=b=1$; $|V_i|$ and $E_b^{q=0}$ are the valence electron ionisation energy and equivalent spin-orbital binding energy in the neutral atom respectively; n_h and n_{max} are the number of subshell holes in the charge state q and maximum number of subshell holes respectively; $\alpha_{IC}^{q=0}$ is the neutral subshell IC coefficient. Note in some references [25] $a=2$ for the K shell, but we affix $a=b=1$ in our analysis. Using this scaling, and equation 2.18, one can check the ratio of our PDB resonance strengths for fully stripped ions, to the resonance strengths computed by A. Pálffy in [19], and check that the detailed balance resonance strength both holds as an upper limit, and an order of magnitude estimate. This is shown to be true in figure 2.2, in which it was noted that the calculations were scaled by a two level branching ratio of type in equation 2.15; it was only assumed photons are to be detected.

Looking at the resonances across different charge states in figure 2.3, for larger i and thus nl , the scaling procedure overestimates by greater than an order of magnitude. We make use of this fact to account for the excited state resonance channels becoming more numerous for higher nlj . An overall accuracy in the NEEC rate due to this scaling, is surmised in chapter 3.

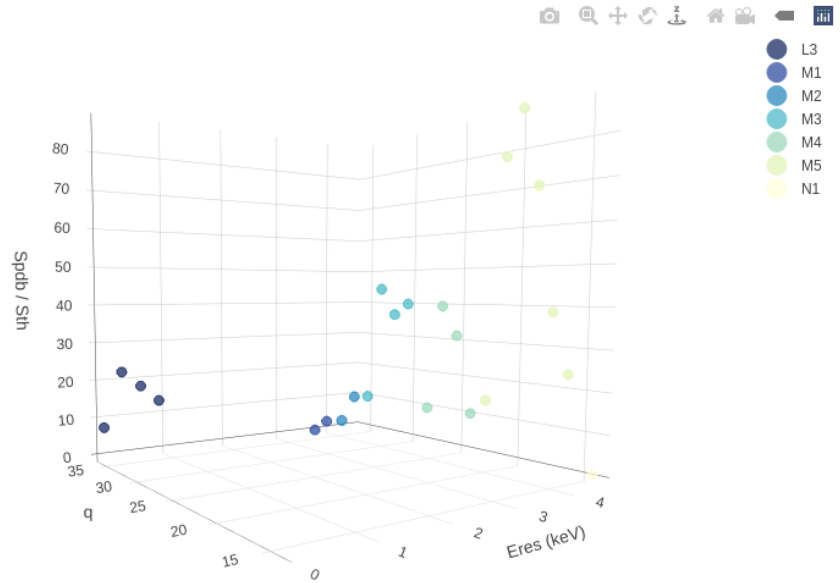


FIGURE 2.3: Comparison of the detailed balance resonance strength to the theoretical calculation using the Feshback formalism by A.Pálffy [12] for the ground state atomic capture channels in ^{93m}Mo in different charge states

One can conclude at this point that it is wise to come up with a naming scheme for these different types of resonance channel.

2.3

Different Microscopic Candidate Systems - Defining the State of the Ion and its Constituents

The NEEC resonance strength can be computed using the general formula 2.12, and then applying the principle of detailed balance to calculate Y_{nec} with equation 2.17. There are however distinct initial and final states of the ion, which one should define uniquely, certainly as the experimenter might want to optimise their experimental setup based on the ability to produce a certain initial species, or the ability to detect a NEEC signature from a particular resonant ion state.

2.3.1 Nomenclature and Different NEEC Cases

The initial nuclear level is either the ground or isomeric state of a nucleus, the capture level refers to the atomic level into which the electron becomes bound.

The depletion level refers to a level just above an initial level (which could be isomeric) which has a much shorter mean lifetime, and excitation to which will ‘deplete’ the isomeric population. The extent of depletion is cause for concern in high neutron flux astrophysical environments where the population of isomers affects the final abundances of nuclides after the ‘freezout’ (becoming transparent to neutrons) of high neutron flux events (such as core collapse supernova) [26].

Triggering (sometimes referred to as depletion) is the act of depleting an isomeric population causing the useful release of energy in terrestrial environments. One might wish to use an isomer as a way of storing energy and releasing it on command via NEEC [27].

Evidently there are two cases for the nuclear level scheme that will involve different computations for the NEEC cross section depending on how we detect the NEEC depletion. Similarly there are many cases for the atomic system.

To compute the viability of our constrained candidate system, it is wise to label each case with a compact nomenclature. We can define different types of NEEC cases that depend on the initial state of the atomic and nuclear systems, and the type of atomic capture that occurs. The NEEC probability (and rate) can be modified and summed depending

on the case one chooses initially, and those which come into existence within the experimental scenario, and we thus label them as follows in order to keep track of what could happen. Note one chooses imposing an upper limit on the NEEC rate per unit time as much as possible, as we would like to always assess how large the number of NEEC's could ever be.

2.3.2 Case A(0)-N0

Case A(0)N0 is the simplest case and involves electron capture into the atomic ground state of a fully stripped atom (A0), exciting a nuclide from its ground state (N0). This is shown in figure 2.4.

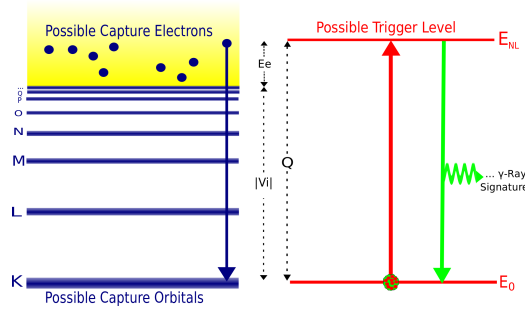


FIGURE 2.4: Schematic of the energy balance between the atomic (left) and nuclear (right) systems for the case A0N0

So in this case, assuming no intruder states between state i and f , and that all photons and conversion electrons can be detected:

$$S = \frac{2\pi^2}{p^2} Y_{neec}^{i \rightarrow d} \quad (2.23)$$

Effectively in this case the IC decay channel is closed, and so $\frac{A_r}{\Gamma_d} = 1$. If there are intruder states between the ground state and depletion level, then one multiplies this resonance strength by the relative gamma intensity, I_γ , of the gamma signature we would like to measure.

2.3.3 Case A(i)-N0: Different Charge state of the atom

A(i)N0 is capture into an ion with ' i ' electrons in their ground state occupying the atom shown in figure 2.5. Ideally an ion will be fully stripped, i.e., in a charge state $Z+$. As

the charge state $(Z-i)^+$ decreases, and the atom becomes more occupied with electrons; $|V_i|$ also decreases, and one would expect there is less chance of finding an energetically suitable nuclear candidate, since nuclear transitions are typically $\sim 1\text{MeV}$ (although can be much less). Not only that but the nuclear wavefunction will less likely overlap with the radial part of the electron wavefunction, as typically the radial wavefunctions become less penetrating in outer electron shells. One always notices a smaller IC coefficient (and thus NEEC rate) for high n shells.

Conversely though, there are still a large number of very low energy nuclear transitions $\lesssim 10\text{keV}$, which involve a band or inter-band transition (typically its collective behaviour changes rather than its nuclear shell model occupation) which could satisfy even a value of $(|V_i| + E_e) < 1\text{keV}$. Therefore it is important we have access to the entire ENSDF nuclear database to search for possible candidate systems, and subsequently all cases.

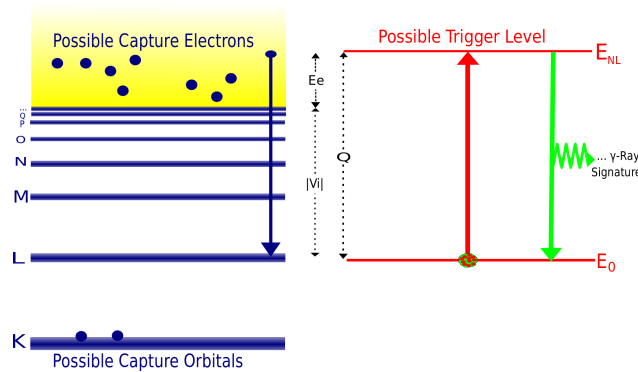


FIGURE 2.5: Schematic of the energy balance between the atomic (left) and nuclear (right) systems for the case $A(i)N0$; specifically $A2N0$ as there are $n=2$ electrons already bound

The resonance strength, assuming we can detect γ -rays as a measurable of NEEC depletion is defined

$$S = \frac{2\pi^2}{p^2} \frac{A_r^{d \rightarrow f}}{\Gamma_d} Y_{neec}^{i \rightarrow d} \quad (2.24)$$

$$\frac{A_r^{d \rightarrow f}}{\Gamma_d} = \frac{A_r^{d \rightarrow f}}{A_r^{d \rightarrow f} (1 + \alpha_{tot}^{d \rightarrow f})} \quad (2.25a)$$

$$= \frac{1}{1 + \alpha_{tot}^{d \rightarrow f}} \quad (2.25b)$$

This accounts for the resonant state (depletion level) having a decay rate that could also IC. If the depletion level were very short lived and the IC coefficient large, one would expect the captured electron to be quickly returned to the continuum of electrons, appearing in a plasma as indistinguishable from the original electron. Furthermore, it is worth noting here that the electromagnetic nuclear lifetime, and thus the NEEC resonance width, can be highly sensitive to the number of electrons on the ion.

Assuming we only want to detect photons, the ratio $\frac{A_r}{\Gamma_d}$ evaluates as in equation 2.15, where we have assumed the only final level after excitation is the ground state.

$$\alpha_{tot}^{d \rightarrow f} = \sum_{1,1,1}^{n,l,j} \alpha_{n,l,j} \quad (2.26)$$

where we include the IC coefficient up to and including the outermost occupied subshell n,l,j .

It is useful therefore to include a branching ratio in the NEEC resonance strength, since it seems the type of measurable, the charge state, and number of final states can strongly affect the overall NEEC cross section.

$$b^{d \rightarrow f} = \frac{A_r^{d \rightarrow f}}{\Gamma_d} \quad (2.27)$$

2.3.4 Case A(i)-Nj: Isomeric Triggering, and how this motivates the work

The existence of metastable (*isomeric*) nuclear states allows us to extend the number of nuclear candidates available, assuming such an isomer can last long enough to pass through the NEEC collision and signature detection apparatus. Thus Case A0-Nj pertains to nuclear excitation from a metastable nuclear state (Nj, being the *j*th isomer in a nuclide) due to capture into the ground state of a fully stripped Atom (A0).

This case is possibly the most interesting and useful. Not only is there a potential for a large amount of energy release as the trigger level (E_{NL}) de-excites, but this energy

leaves the possibility for an easily identifiable signature, which is unique from relaxation of the isomeric energy back to the ground state to E_0 . This is represented in figure 2.6.

The resonance strength for an isomeric species is given in [12] as:

$$S_{neec} = \frac{2\pi^2}{p^2} b^{d \rightarrow f} Y_{neec}^{i \rightarrow d} \quad (2.28)$$

where $Y_{neec}^{i \rightarrow d}$ is the NEEC rate from the isomeric level to a level just above, typically with a much shorter half-life. $b^{d \rightarrow f}$ is the branching ratio between the depletion level back to the isomer, and now involves an additional summation due to there being multiple final levels.

$$b^{d \rightarrow f} = \sum_f \frac{A_r^{d \rightarrow f}}{A_r^{d \rightarrow f} (1 + \alpha_{tot}^{d \rightarrow f})} \quad (2.29a)$$

$$= \sum_f \frac{1}{1 + \alpha_{tot}^{d \rightarrow f}} \quad (2.29b)$$

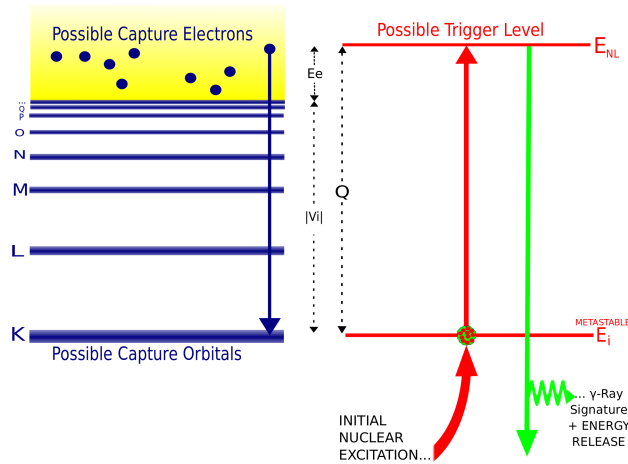


FIGURE 2.6: Schematic of the energy balance between the atomic (left) and nuclear (right) systems for the case $A0N_j$. N_j is the j th metastable state in a nuclide

We then have to sum the IC coefficients over all bound electrons and all final nuclear levels. To avoid this, we can assume we only want to detect the depletion level returning to the isomeric state, so we can use the overall half-life to produce this and if necessary use the relevant conservation equation $1 - I_\gamma$ from the relative intensities that are already measured and tabulated.

2.3.5 Case A(i)-X-Nj: Capture that produces an excited atomic state

A. Pálffy *et al* ([28], 2008) have suggested a further case in which NEEC occurs into an excited atomic orbital of the ion (coined "NEEC-X"). One can assume excitation to such a state is defined as usual, except that there is now a doubly excited atomic and nuclear state.

$$S_{neec} = \frac{2\pi^2}{p^2} b^{d \rightarrow f} Y_{neec}^{i \rightarrow d_1} \quad (2.30)$$

with a branching ratio that is also via an intermediate resonant state d_1 due to the excited atomic state

$$b^{d \rightarrow f} = \frac{A_r^{d_2 \rightarrow f} A_{x-ray}^{d_1 \rightarrow d_2}}{\Gamma_{d_2} \Gamma_{d_1}} \quad (2.31)$$

The captured electron then decays into a lower atomic state, emitting an X-ray, providing a further signature of the capture, shown in figure 2.7. This relaxation will have a much shorter lifetime than the nuclear relaxation, due to the approximation from Heisenberg's uncertainty principle:

$$\Gamma_{d_1} T_{\frac{1}{2}} \sim \hbar \quad (2.32)$$

Since atomic energy widths are typically many orders of magnitude larger than nuclear widths, the atomic half-life is typically shorter.

This NEEC resonance case also introduces an increase in the total resonance width Γ_{neec} . Using the definition of the resonance width 2.7

$$\Gamma_{neec} = \Gamma_{d_1} + \Gamma_{d_2} \quad (2.33)$$

Where d_1 is an additional atomic level width, which in previous cases was infinitesimally small due the stability of the atomic capture level in its ground state. Here Γ_{d_1} could be as large as 1eV and we place this upper limit on future calculations.

The overall resonance strength may not necessarily increase, but the width of the Lorentzian certainly will, allowing a larger probability of overlap with the continuum electron energy distribution.

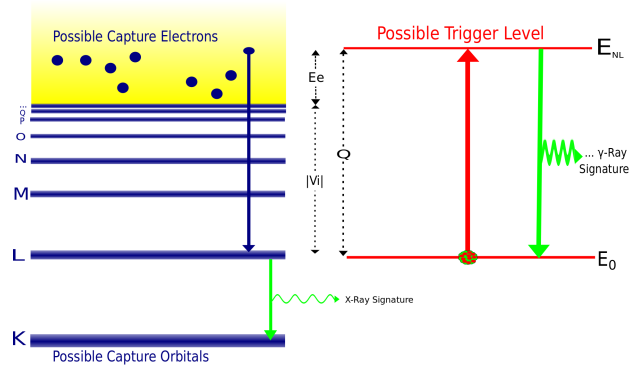


FIGURE 2.7: Schematic of the energy balance between the atomic (left) and nuclear (right) systems for the case A0-X-N0

If the candidate system is moving quickly enough, then the X-ray signature will be spatially separated from the γ -ray signature, allowing for coincidence in detection of the overall NEEC signature. Detrimentially, if the capture system is localized, then the X-ray and γ -ray signatures will be difficult to resolve temporally, due to dead time of the detectors, decreasing the overall detection efficiency.

In this (A0-X-N0) situation, as mentioned by Pálffy *et al* ([28]), the fast X-ray relaxation closes the IC decay channel in the nucleus; often K-shell IC is energetically forbidden as the atomic binding energy is too great for the nuclear transition, but also the nuclear transition is too slow. This might be of some use in explaining the unexpected lifetimes of certain nuclides in high electron density astrophysical plasmas.

2.3.6 X-NEEC: NEEC into an already excited atomic state

This additional case was originally suggested by Pálffy *et al* [29] and recently further investigated theoretically by Gargiulo *et al* [11] (and referred to as NEEC-EXI), in which there could initially be any number of holes in the inner atomic orbitals up to the outermost occupied electron. We would expect these states to be short lived, and unlikely to exist in large enough quantities to affect the NEEC rate. However, if by making the resonance channels more numerous by a factor of $\sim Z^2$, one could expect an increase of one or more orders of magnitude in the NEEC rate. We do not consider this case implicitly in our analysis as the ability to calculate the abundance of these initial states in an environment is still in its infancy. However, when we consider the NEEC rate using α_{tot} and an

effective impact energy, we can be sure the extent to which we overestimate the NEEC rate will include the X-NEEC channels, so long as select the correct effective energy.

Clearly we can combine cases, and so there might be a Candidate System which involves $A0N2$, $A1N2$ and $A1-X-N2$... capture into the atomic ground state of the second isomer of an atom with 0 and 1 electrons; charge states $(Z)^+$ and $(Z-1)^+$, and all excited atomic states above.

2.4

Motivation of the Work, Origins of Isomerism and its Importance for NEEC

Although an interesting academic exercise, there must be a broader use to characterising and understanding NEEC. Most notably, is the application of NEEC in the field of nuclear isomers.

First proposed by Frederick Soddy in 1917, isomers are meta-stable nuclear excited states, above the ground state in energy, which last a hundred nanoseconds or much more before decaying electromagnetically, albeit more slowly than usual due to being hindered, into a less energetic arrangement. Most energy levels (or states) within a nuclide decay promptly (typically within ps or less) and so do not affect the course of decay back to the ground state [30] when observing with a clock that counts 10's of femtoseconds.

In a hot-dense astrophysical environment (such as in a core-collapse supernova remnant) there is a high flux of neutrons and electrons colliding with a wide distribution of heavy ions in various charge states. Such an environment is responsible for the production of the heavy elements past Fe, where a complex balance between neutron capture and alpha/beta-decay ferment the production of larger nuclear masses thanks to the strong force binding them together. Typically, via the R(rapid)-process, the neutron capture events continue until the neutron capture cross section diminishes on the neutron drip line, known as neutron capture 'freeze-out'. The isotopes decay then back to stability quite unimpeded once the neutron flux has diminished. However, if still within the recent-supernovae environment, there is a balance of neutron capture and beta-decays, which heavily affect the final distribution of stable isotopes. In this environment, rarely considered are the effect of electron flux on these final abundance pathways. Since this

cross section varies depending on the excited state of a nuclide, depopulation of isomers via NEEC could have a notable effect on the final abundance of heavy nuclides in nature, depending on the route the (neutron *and* electron moderated) decay pathway took. More interesting in a terrestrial sense, is the concept of being able to deexcite an isomeric nuclear state quickly, allowing it to release its energy quickly. By definition, an isomer is long-lived, and its population will only decay very slowly, and its radiation intensity cannot be made use of. Coherently exciting the isomer to a shorter lived level just above the isomer will cause a massive energy release.

A highly topical example of such an isomer is in the nuclide ^{93}Mo shown in figure 2.8. We see the $17/2^+$ level is much shorter lived than the isomer, and one can quickly depopulate the isomer by exciting to this level, causing its prompt decay.

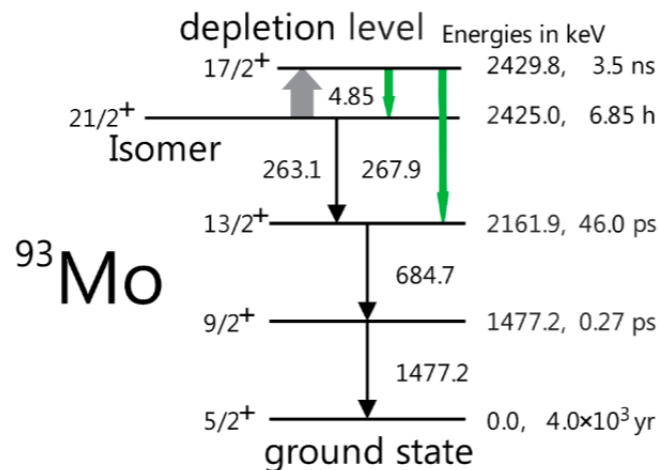


FIGURE 2.8: Part of the ^{93}Mo level scheme. The isomer has a lifetime of roughly 6 hours, though triggering from the level above via NEEC can promptly depopulate (deplete) the isomeric level, releasing its energy on command via a promptly decaying state above. Figure from [31]

This triggering pathway has been the subject of theoretical calculation over recent years [27] and there was reported an observation of NEEC in the depletion of the isomer via the beam-foil technique in [22] although a recent repeat of the experiment [32] and theoretical calculation [33] sheds doubt on this.

Thinking about NEEC overall how can this process ever be useful if there is reasonable doubt that it is observable, given 44 years since it was proposed? There is a possibility that PT-symmetry is insufficient to describe the axioms of the interacting subsystems.

2.4.1 Types of Isomers

We avoid going into too much detail about the physics of isomerism, as the literature on the matter is extensive and informative. A thorough historical review is provided by Walker and Podolyak [30], whilst an atlas of all the known isomers and their properties up to c.2015 is collated in [34], which we use as our isomer database in chapter 4. It would be a thesis in itself to go into full detail of the fundamental importance of isomerism studies, and Dracoulis, Walker and Kondev have done this in [21].

We note topologically that for an isomer to be astrophysically significant it must have a half-life greater than 1ns and generally a level is considered to be isomeric if it has a half-life greater than 100ns, and that its decay is hindered by quantum numbers, within one of the five categories [21] [34]:

- Spin (J^π) - large multipolarity transitions
- K - A collective decay in a rotational collective band is hindered
- Shape - Nucleons find themselves within a local minimum of the liquid drop model
- Fission - Competing shape and fission decay paths
- Seniority of intruder orbitals near magic numbers³.

Discussion: For NEEC to occur from an isomer we would like to be in a state with a high level density and many possible isomers. This is especially true of K-isomers that have odd numbers of protons and neutrons [35], a good example of such is ^{178}Ta .

2.4.2 Motivation to Select Prevalent Isomer Triggering Pathways

Many people are heavily invested in this process existing, so we need to define a method that is independent yet an amalgamation of past and current methods, both in their influence and end goal. One way to start is to search through what we already know about nuclei and atomic levels, and present a method for an upper limit estimate of all experimental NEEC scenarios. Thus less time will be wasted overall through poorly informed approaches.

³numbers of protons and neutrons that form closed shells

Chapter 3

How Much NEEC?

Building a bridge between nuclear and atomic physics is paramount for the development of new energy storage technologies [36], elemental in our understanding of nuclei, and their formation in the cosmos. As is evident in the state-of-the-art theoretical NEEC literature [12], computing the NEEC resonance strength is difficult *ab initio* and is time consuming and less informative when trying to build a tabulated understanding of this scale change. Without a collective model for the nuclear excitation, as relied upon in [12]; the *ab initio* problem becomes quickly intractable, unless one has an initial basis for both tabulating, approximating and thus calculating the interaction of all the nuclear and atomic subsystems. We have so far circumvented the calculation problem by applying the principle of detailed balance, which relies on PT symmetry, from which we assume the extent of the inverse-processes of internal conversion, namely NEEC, must be entirely electromagnetic. As more experiments occur over the coming years, we aim to summarise in this chapter a way in which one can calculate an absolute upper limit of the experimental NEEC rate, and find via a candidate search where one should compare this to a maximal theoretical estimate for the NEEC rate.

Furthermore, being able to rule out an un-viable NEEC experiment ahead of time would be very useful to the current NEEC community, who met officially for the first time *en masse* in late 2019. It was evident there that NEEC identification requires a well connected ensemble of interdisciplinary researchers; notably, it was difficult to conclude what should be done to achieve repeatable NEEC observations in the next few years, other than that we should distinguish all excitation mechanisms from NEEC (a job which is extremely complex), and possibly reconvene in around '2 years'.

We must be meticulous in how we define how much NEEC occurs via a macroscopic

situation, and it should be presented in a way that is comparable across an ensemble of interdisciplinary researchers.

We can no doubt define a mathematically rigorous way of notating and defining the experimental NEEC probability, summarising what has already been done, and applying it to the three main experimental approaches, which are summarised in this chapter.

3.1

The Generalised NEEC probability

Using the principle of detailed balance as described in chapter 1, one can place an upper limit on the NEEC resonance strength, which we will use in the proceeding derivations. First, we will examine how one overlaps macroscopic parameters energetically with microscopic NEEC resonances.

3.1.1 Generalised NEEC Probability for a Single Capture Channel - energetic tabulation

Originally supposed by Goldanskii *et al* in [1], if there is a time-reversed process of internal conversion, then energy must still be conserved. The NEEC energy balance is expressed as follows, and one must engrain this in one's mind.

$$E_{res} + |V_i| = Q \quad (3.1a)$$

$$\text{Energy gained by electron at correct impact energy} = \text{Nuclear transition energy} \quad (3.1b)$$

That is, the sum of the impact energy and the energy gained by the electron becoming bound into the atom must equal the nuclear transition energy. Of course, considering this as an electromagnetic interaction, the nucleus keeps the same number of protons and neutrons, they just jiggle about to a different extent. The electron-ion impact energy is the same as the residual kinetic energy that came from the IC energy balance in equation 1.1.

E_{res} is the required resonance energy of the electron in the nuclear rest frame; the amount of energy we need to put in to induce the resonance, and thus excite the nucleus. In general the lab frame is considered as the frame of reference, otherwise the stationary species becomes the frame of reference via a conversion factor. In a plasma environment,

the lab frame and ion rest frame are expected to be equivalent due to the ions moving considerably more slowly than the electrons. The fraction of continuum electrons with the resonance energy is loosely defined by the ratio:

$$\frac{\Gamma_{neec}}{\Delta} \quad (3.2)$$

This is known as the resonance fraction, and gives us a way to evaluate the efficacy of a macroscopic parameter (e.g. longitudinal beam energy distribution, or a laser irradiance) Δ is the effective width of the experimental electron-nucleus impact energy distribution, and Γ_{neec} is the width of the resonance at the collision energy, and is composed of contributions due to broadening of the capture-electron orbital energy and nuclear-excited state energy [19]. Effectively there is a width in both $|V_i|$ and Q due to the instability of the levels.

$$\Gamma_{neec} = \Gamma_{V_i} + \Gamma_Q \quad (3.3)$$

Put more succinctly, the macroscopic probability of NEEC in an experiment will be dominated by the maximisation of 3.2 by tuning the electron nucleus impact energy distribution macroscopically for the best overlap of Γ_{neec} with Δ energetically and temporally, whilst also the resonant cross section σ_{res} is maximised by choosing the correct nuclear-atomic species. For now, the resonance fraction is accurate if Δ is the width of a square probability function, as is $\sigma(\Gamma_{neec})$, so 3.2 remains a fraction. In actual fact E will have a statistical distribution, so the actual resonance fraction will require folding of the impact energy distribution with the cross section shape (integrating the product over energy, for each instant in time).

The resonance width Γ_{neec} , for a capture channel into the electronic ground-state, will be the width of the excited nuclear level $\Gamma_{neec} = \Gamma_Q$, since the atomic ground state is always stable and hence of infinitesimal width in energy. Typically such a value is $\Gamma_Q \sim 10^{-7} \text{eV}$ [29].

For a capture channel into an excited electronic state, the atomic lifetime is much shorter than the nuclear lifetime, and so the atomic width is dominantly large. Thus the resonance width is dominated by this $\Gamma_{neec} \approx \Gamma_{V_i} \sim 1 \text{eV}$ [29]. It is shown in this chapter that the NEEC width is irrelevant when calculating the NEEC rate due to the continuum

electron energy varying slowly across a NEEC resonance.

The resonant cross section σ_{res} [Length²] is an effective area that will permit the interaction between an ion and an electron should they come into proximity. Macroscopically, when evaluating how many times a reaction has occurred, we multiply this area per particle pair by the number of particle pairs that come into proximity; so the cross section gives us a way of tabulating how well a macroscopic parameter will be affected by the microscopic area i.e. "how effective is our resonant NEEC flux, ϕ_e [m⁻²s⁻¹] according to QED", or at least in our case according to the principle of detailed balance.

Let us be more careful with the definition of the resonance electron-nucleus impact energy and assert that the effective resonance energy E_e is the resonance energy and remains constant within the width of the Lorentzian centered on E_{res}

$$E_e = E_{res} \pm \frac{\Gamma_{neec}}{2} \quad (3.4a)$$

$$\sigma_e = \sigma_{res}(E) \Big|_{E_{res}-\Gamma_{neec}/2}^{E_{res}+\Gamma_{neec}/2} \quad (3.4b)$$

and so for simplicity we can say σ_e is the effective cross section and is some square Dirac-delta-like function that is the resonant cross section within the resonance width, and zero elsewhere. We call this the narrow resonance approximation¹. The subscript 'e' implies a range of some variable that is effective within the resonance width, and is applied to the function or variable to which this subscript is applied.

The NEEC probability (or by association the NEEC yield N_{neec}) must be proportional to the product of these microscopic and macroscopic factors:

$$N_{neec}(E_e) \propto \sigma_e \times \frac{\Gamma_{neec}}{\Delta} \quad (3.5)$$

or as given in [1] for a plasma in a steady state over lifetime τ

$$N_{neec}(E) = n_{i-e}(E)v_e(E)\sigma_e(E)\tau \quad (3.6)$$

¹This approximation is explored in section 3.1.2, shown to be accurate for a wide and slowly varying continuum energy and any possible value of Γ_{neec}

where v_e is the velocity of the impacting electron within the resonance width. The concentration of collisions per-ion in the plasma at the resonance energy is defined in [1] as $n_{i-e} \approx n_{elec}\Gamma_{neec}/T$ in this case (and thus appears the resonance fraction), with T the electron temperature ideally $\sim Q \approx \Delta$; though it is noted there is not a proper consideration here to the number of ions in such a plasma. Here we see the resonance fraction is implicitly expressed as the product of a mean interaction density and velocity, since a plasma is essentially a mixture of charged fermions [colliding in a complex varying electromagnetic field exchanging electromagnetically only photons and W-bosons (virtual photons)], and can be characterised as spending some time τ in a characterisable steady state. The product $n_e v_e$ is the effective electron flux [$cm^{-2}s^{-1}$] impacting a nucleus at rest. It is represented as ϕ_e .

$$\phi_e = n_e v_e F(E_e) \quad (3.7)$$

with $F(E_e)$ the fraction of impact energies within the resonance width, defined implicitly by integrating some statistical distribution function over Γ_{neec} .

One asserts a definite integral upon defining the macroscopic situation

$$N_{neec} = \int_{t_i}^{t_f} \int_{E_{min}}^{E_{max}} \phi(\mathbf{t}, \mathbf{E}) \sigma(E) dE dt \quad (3.8a)$$

$$= \int_{\tau} \phi_e \sigma_e dt \quad (3.8b)$$

integrated over the total time $\tau = t_f - t_i$ the NEEC environment exists for and bounded by the energetic distribution experienced over this time, $\Delta = E_{max} - E_{min}$. For a single resonance ϕ_e evaluates the energy integral with the effective notation described in equation 3.4. The time integral remains indefinite, until we introduce real macroscopic environments, or a temporal dependence of the effective electron flux, $\phi_e(t)$, is defined.

To design an experiment we must optimise ϕ_e in the lab frame by maximising the resonance flux for as long as possible. We must also find a nuclear-atomic system whose total resonance cross section is large and accessible by the flux available in an experimental environment. Remember σ_e is an effective area for NEEC (geometrically) per particle pair, chosen *a priori* by the ion species.

3.1.2 Cross section and Resonance Fraction - The Narrow Resonance Approximations

As already discussed in chapter 2, considering the resonant nature of NEEC, we have defined the resonance strength, S . The resonance cross-section varies sharply within Γ_{neec} , peaking at the resonance energy E_{res} . We have introduced a resonance line-shape function of the cross section, $Lor(E, \Gamma_{neec})$, as expressed in the Breit-Wigner formula in equation 2.5, also referred to as a Lorentzian lineshape, and rewritten here for reference.

$$Lor(E, \Gamma_{neec}) = \frac{\Gamma_{neec}/(2\pi)}{(E - E_{res})^2 + (\Gamma_{neec}/2)^2} \quad (3.9)$$

The magnitude of the variation of the Lorentzian w.r.t. to a realistic Gaussian distribution of electron beam energies in an electron beam ion trap (EBIT) is shown in figure 3.1. The example given is a real and simplistic system of exciting a ground state ^{57}Fe nucleus NEEC'ing to the 14.41keV M1(+E2) transition that would require $E_e = 5.14\text{keV}$. As can be seen, the distribution of impact energies is constant within a ground state NEEC capture channel (labelled as an A1N0 type case " $^{57}\text{Fe}(1)\text{N}(0)$ ") and shows the reason for using a narrow resonance approximation.

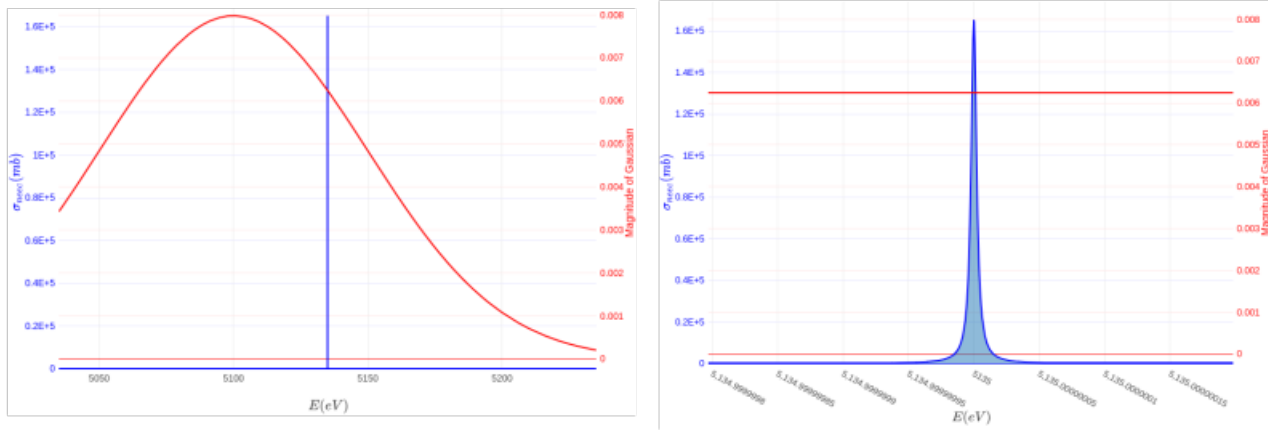


FIGURE 3.1: NEEC Cross section (blue) and Gaussian (red) for AiNj cases where $\Gamma_{neec} = \Gamma_{nuclear} = 5 \times 10^{-9}$ eV

In the case $^{57}\text{Fe}(0)\text{-X}(2)\text{-N}(0)$, the broad atomic width of the capture channel sees the continuum energy vary across the resonance, though only by a small fraction of the total, and in a roughly linear fashion, as shown in figure 3.2. With this a limiting case seeing the width and macroscopic slope as an upper limit, we assert that a narrow resonance

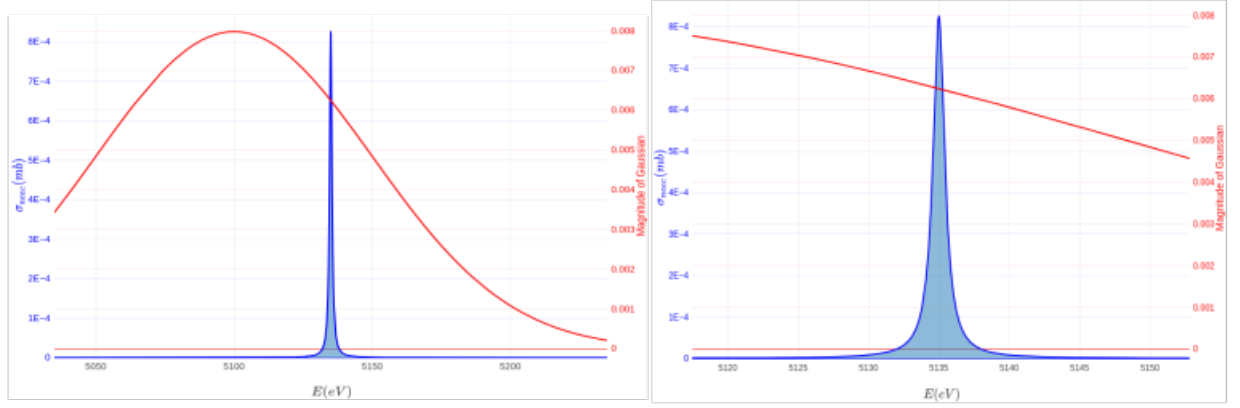


FIGURE 3.2: NEEC Cross section (blue) and Gaussian (red) for Ai-X-Nj cases where $\Gamma_{neec} = \Gamma_{atomic} \approx 1\text{eV}$

approximation is still valid, especially since the mean value of $F(E)$ would still be at the resonance energy.

Experimentally one always requires a cross section to evaluate the macroscopic reaction rate, and we use the peak value at E_{res} across the resonance width. $E_e = E_{res} \pm \frac{\Gamma_{neec}}{2}$ and as such assert a Dirac delta like Lorentzian, $Lor(E_e, \Gamma_{neec}) = \frac{2}{\pi\Gamma_{neec}}$, so the resonant cross section, within the effective resonance energy is

$$\sigma_{res}(E_e) = S_{neec} \frac{2}{\pi\Gamma_{neec}} \quad (3.10)$$

To summarise what we know so far, NEEC rate will be expressed as:

$$R_{neec} = \phi_e \sigma_e = n_{i-e} v_{res} \sigma_e \int_{\Gamma} F(E) dE = n_{i-e} v_{res} F(E_{res}) \cdot \Gamma_{neec} S_{neec} \frac{2}{\pi\Gamma_{neec}} \quad (3.11)$$

From Chapter 2;

$$S_{pdb} = \frac{2\pi^2 (2I_d + 1)(2J_d + 1)}{p^2 (2I_i + 1)(2J_i + 1)} \alpha A_r^{d \rightarrow i} \quad (3.12)$$

where S_{pdb} is estimated as an upper limit for S_{neec} , via the principle of detailed balance as in equation 2.17.

Alternatively, we can present the generalised NEEC probability which will be the rate per unit time divided by the total number of electron-ion collisions.

$$P_{neec} = \frac{S_{pdb} Lor(E_{res}, \Gamma_{neec}) \int \int \phi_e(E, t) dE dt}{N_{coll}} \quad (3.13)$$

In a frequentist approach to probability, N_{coll} will be the total number of collisions, and so in general pertains to the number of ions one introduces into the environment, which is normally very constant and controllable. As such, maximising the electron flux w.r.t. to the ion injection is the main problem.

Any experiment will require a large amount of control over the *resonant* flux of electrons, via the continuum electron distribution function, where one provides a careful choice of the spectrum of available atomic capture levels, for as long as possible.

3.1.3 The Total NEEC Resonance Strength - summing over capture channels introduced

In a dense environment containing energetic ions and electrons, the charge state of each ion is likely to change after a collision due to effects such as electron capture (resonant and non resonant) and impact ionisation [12]. Thus the charge state distribution will be changing over time, opening and closing possible NEEC channels. This is until an equilibrium is reached between capture and loss, allowing an empirically definable equilibrium distribution function, which will then evolve slowly as the experimental conditions evolve.

We sum over all possible NEEC capture channels and charge states, each represented by α_p and q respectively [33]:

$$P_{NEEC} = \sum_{\alpha_p, q} f_q P_{neec} \quad (3.14)$$

where f_q is the fraction of ions in that charge state and the equilibrium distribution of these fractional probabilities is somewhat characterisable as a Gaussian distribution about a mean charge state \bar{f}_q [33]. α_p represents the lowest available atomic capture orbital IC channel for that charge state, and is the same as a correctly over-scaled subshell IC coefficient.

Unfortunately only a few of the total charge states can be available within the equilibrium time, so the experimental resonance strength, S_{exp} is some small fraction of the

total resonance strength exposed S_{tot} depending on the available capture channels, defined by the CSD explored... i.e. not all capture channels will remain open for the entire experiment.

We define here some distinctions between the different resonance strengths.

If we use S_{tot} this is a theoretical upper limit defined by using α_{tot} at the impact energy E_{eff} from the mean atomic binding (ionisation) energy. Similarly this approximates an upper limit on all possible NEEC channels, including X-NEEC and NEEC-X channels, for which we estimate this to be on the order of Z^3 resonances.

$$S_{\alpha_{tot}} = \frac{2\pi^2}{p^2} \alpha_{tot} A_r > \sum_p S_{nec}(\alpha_p) > \sum_{i=1}^{Z^3} \frac{2\pi^2}{p^2} \alpha_i^q(n_i l_i m_{j_i}) A_r \quad (3.15)$$

S_{nec} for each capture channel is approximated by S_{pdb} .

3.1.4 The Calculated Resonance Strength

S_{nec} is the resonance strength into a specific capture channel. A capture channel is specified by the atomic charge state, and the available electron eigenstates within this.

This is a nonconvex problem, i.e. there are several local maxima to the figure of merit (P_{NEEC} , R_{NEEC} or N_{NEEC}). Though holistically we can apply upper limits to all scenario's and therefore find a place to start in searching for the actual global maximum over energy and time.

We must first analyse the NEEC flux and its time dependence in a simple scenario of a single available capture channel, to be able to ascertain which resonance strength is most appropriate.

3.2

Resonant Flux - Velocity and Density of Collisions

3.2.1 The Collision Flux

The collision flux is in the most general form,

$$\phi(\mathbf{t}, \mathbf{E}) = n_{i-e}(t, E) v(t, E) F(t, E) \quad (3.16)$$

which will require computation of a massive wealth of charge changing collisions within the interaction volume across the interaction energy distribution and experiment time. We are only interested in adding up the collisions of interest, which is those that occur within the effective NEEC resonance energy. But also one hopes not to spend weeks calculating the temporal evolution of the collision density via Particle in Cell (PIC) codes such as EPOCH [37]. The only way to do this is to introduce an absolute upper limit.

So the effective NEEC collision flux provided macroscopically is

$$\phi_e = n_{i-e}(t)v_e F(E_e) \quad (3.17)$$

Here we have highlighted a commonly made approximation that the energetic dependence of the resonance fraction is temporally static across the resonance width, Γ_{neec} , and the collision density is energetically independent across the resonance, via the dependant variables of $n_{i-e}(t)$ and $F(E_e)$ respectively. One must present a temporally static ion-electron collision density and a maximal energetic fraction

3.2.2 The Energetic Fraction - Probability of a collision at a certain energy

For every electron-ion collision energy there will be an probability associated macroscopically.

For a stationary ion (or electron), the moving species will be Gaussian distributed in energy once macroscopic control has been asserted at a facility, with standard deviation Δ . Typically this distribution is seen in the longitudinal energy of a charged particle beam.

$$F(E) = \frac{1}{\Delta\sqrt{2\pi}} \exp\left(-\frac{1}{2} \frac{(E - E_{mean})^2}{\Delta^2}\right) \quad (3.18)$$

For the two narrow resonance approximations made above we assert the simplification of its energy integral across any NEEC resonance, giving us a reliable formula for the effective resonance fraction:

$$\int_{E_{res}-\frac{\Gamma}{2}}^{E_{res}+\frac{\Gamma}{2}} F(E)dE = F(E_{res})\Gamma_{neec} = F(E_e) \quad (3.19)$$

3.2.3 The Collision Velocity $v(t, E)$ and Momentum $p(t, E)$

The velocity of the electron (in the ion rest frame, which is near the centre-of-mass (COM) rest frame) is purely a result of its kinetic energy. The required velocities for NEEC, especially in hot-dense plasmas, are relativistic, so we use the relativistic formula for kinetic energy to calculate the resonant velocity:

$$E_e = (\gamma - 1)m_e c^2 \quad (3.20a)$$

$$v_e = c \sqrt{1 - \frac{1}{\left(\frac{E_e}{m_e c^2} + 1\right)^2}} \quad (3.20b)$$

with m_e the mass of the electron and $\gamma = \frac{1}{\sqrt{1 - \left(\frac{v}{c}\right)^2}}$ the relativistic Lorentz factor.

The momentum is calculated by rearranging the relativistic energy momentum relation:

$$p = \sqrt{\frac{(E + m_e c^2)^2 - m_e^2 c^4}{c^2}} \quad (3.21)$$

The temporal aspect of these variables for each capture channel is binary - they either exist for some time or they don't.

3.2.4 The Ion-Electron Density - $n_{i-e}(t, E)$

The maximal possible density of collisions is defined generally as a density of ions and electrons within the interaction volume as [27]:

$$n_{i-e} = \int_{V_{int}} n_{elec} n_{ion} dV \quad (3.22)$$

with V_{int} the maximal volume of the interaction region.

Using the lab frame in a homogeneous electron-beam ion-trap,

$$n_{i-e} = n_{elec} n_{ion} V_{int} = n_{elec} N_{ion} \quad (3.23)$$

N_{ion} is the number of ions injected (or trapped) in the interaction volume, and n_e the number density of electrons [cm^{-3}] available in the interaction region.

Conversely, with an ion beam and stationary electrons, one would have

$$n_{i-e} = n_{ion}n_{elec}V_{int} = n_{ion}N_{elec} \quad (3.24)$$

where instead we have applied the volume integration over the number of electrons N_{elec} illuminated by a stored² ion beam. The term $\phi_{ion} = n_{ion}v_{ion}$ would be the flux of incoming ions, and then, multiplied by the stationary number of particles illuminated by this beam, becomes the luminosity

$$\mathcal{L} = \phi_{ion}N_{elec} = n_{ion}v_{ion}N_{elec} = n_{i-e}v_{ion} \quad (3.25)$$

This is the fixed target luminosity used to estimate as an upper limit the collision density over time.

The time dependence arises as the interaction region moves towards equilibrium collision densities, or stays constant over time in a static equilibrium. In the next section we will consider the simplest scenarios that involve equilibrium (temporally static) collision densities.

3.2.5 Summary of Generalized NEEC Probability - Temporally static equilibrium

So the NEEC probability from equation 3.13, can be split up into temporally static and temporally dynamic situations.

By temporally static, we mean the NEEC conditions can be turned on and off at will, affecting only the collision density (as a function of energy), which remains constant over time. We can thus define a NEEC rate for this situation and multiply it by the time τ the conditions exist for, to give a NEEC excitation number. When temporally static, this is always the figure of merit, and can also be referred to as the NEEC yield.

$$N_{nec} = \int \int v(E_{res})\sigma_{res}n_{i-e}F(E_e)dEdt \quad (3.26a)$$

$$= \int dt n_{i-e}v(E_{res})\sigma_{res} \int_{E_{res}-\frac{\Gamma}{2}}^{E_{res}+\frac{\Gamma}{2}} F(E)dE \quad (3.26b)$$

$$= \tau R_{nec} \quad (3.26c)$$

²Note an ion beam in a storage ring is profoundly similar to an ion trap; the ion is kept at a prescribed energetic and temporal phase space provided by the accelerator magnets and cavity electric field. From the ions perspective, the upper limit flux of electrons appears the same

where R_{neec} is the equilibrium NEEC rate.

$$R_{neec} = n_{i-e} v_{res} \sigma_{res} \int_{E_{res}-\frac{\Gamma}{2}}^{E_{res}+\frac{\Gamma}{2}} F(E) dE \quad (3.27a)$$

$$= n_{i-e} v_{res} \sigma_{res} F(E_{res}) \Gamma_{neec} \quad (3.27b)$$

This is relevant in a scenario where we have an electron beam impinging stationary ions, or vice versa. The distribution of collision energies is the same for both cases in the COM frame, although a different conversion must be made for each to convert from COM to lab frame. We always express the problem in terms of COM energy and then make the conversion to the lab frame.

3.3

The Simple Scenarios

3.3.1 A Simple Example - An Electron beam impinging a stationary fully stripped ensemble of ions

In the simplest scenario possible, one can consider some confined and stationary fully-stripped ions being impinged by a stream of Gaussian distributed electrons. The central electron energy will be tuned to the atomic binding energy with the largest magnitude (thus requiring the lowest impact energy) $E_e = Q - |V_1|$, with $|V_1|$ being equivalent to the ionisation energy of the $(Z - 1)+$ ion. Using equation 3.27 and the second narrow resonance approximation, the NEEC rate for a centred Gaussian distribution would be:

$$R_{neec} = n_{i-e} v_{res} S_{pdb} \frac{2}{\pi \Gamma_{neec}} \frac{\Gamma_{neec}}{\sqrt{2\pi} \Delta} \quad (3.28)$$

Interestingly, as already seen in equation 3.11, the rate is independent of the resonance width. This is true for a situation where the beam energy distribution is tuned exactly to the resonance energy (i.e. the peak of a Gaussian distribution of collision energies is centered on E_e), which might not be the case due to accelerator difficulties, or energy loss on transit through the target. This is also true for an off center electron energy distribution where we can use the narrow resonance approximation again, by assuming that

when not slowly varying for the widest atomic widths, the variation is still linear across the resonance, as in figure 3.2. Thus we state that in all cases, the macroscopic rate is independent of the resonance width, as the width cancels as in equation 3.28 above.

$$R_{nec} = N_{ion} n_{elec} v_{res} S_{pdb} \frac{2}{\pi} F(E_{res}) \quad (3.29)$$



FIGURE 3.3: Magnitude of a Gaussian (red) and Lorentzian function (green) with the same energy axis, for a typical EBIT electron beam longitudinal width and a $^{57}\text{Fe}(0)\text{N}0$ capture to excite the 14keV Mossbauer transition $E_e = 5\text{keV}$. The y axes are adjusted so their peaks match in height, so the green area also shows the resonant fraction for a normalised Gaussian

One notes the Lorentzian curve appears as a vertical line due to the narrowness of the NEEC width $= 1 \times 10^{-9}$ eV, and also the vertical line represents the energetic phase space area of resonant electrons. Integrating properly, the ratio of this narrow resonance area to the total area of the Gaussian is the resonant fraction $\sim 10^{-7}$.

In this simple situation, of a fully stripped ion, we could palpably use the neutral IC coefficient for the K electron shell to calculate the resonance strength of the ion where only K capture channels are being considered, especially due to the fact that many-body terms in the electron Hamiltonian are small. Using the associative relation defined in 1.4, the K shell contribution to the IC coefficient and thus the resonance strength can be averaged across the shell. For now this is reasonable upon summing the total shell resonance strength, whilst we withhold the fact that single capture contributions will be partitioned in a difficult way when we include all NEEC-X resonances as well. So in this situation, the idea that $\alpha_K^{q=Z} = \alpha_K^{q=0}/2$ is fine, since there are two holes in the K shell

AX	E_i	E_d	V_1	E_e	J_i	J_f	$B(\pi L)$	$B(\pi' L')$	δ	α_k	S_p
	keV	keV	keV	keV			w.u.	w.u.			beV
^{57}Fe	0.0	14.4	9.23	5.17	$\frac{1}{2}-$	$\frac{3}{2}-$	0.0078	0.37	0.00223	7.65	0.134

TABLE 3.1: Example $^{57}\text{Fe}(1)\text{N}0$ Resonance strength calculation **data structure** (w.u. are Weisskopf Units)

that can be occupied, and their energies and wavefunctions will not differ from neutral values significantly in such an inner shell, and their sum is equivalent to twice their average. We also assert that the continuum electron (in the beam) has only its intrinsic angular momentum, $J_c = 0.5$.

$$S_{neec}^{q=Z} = \frac{S_{pdb}^{q=0}(\alpha_K)}{2} \quad (3.30)$$

$$S_{pdb}^{q=0}(\alpha_K) = \frac{2\pi^2 (2J_d + 1)(2J_{at} + 1)}{p^2 2(2J_i + 1)} \alpha_K A_r^{d \rightarrow f} \quad (3.31)$$

So using typical values for ^{57}Fe from the ENSDF database and BrIcc calculation tool the microscopic parameters (un-scaled at this stage) are shown in table 3.1. This shows a typical data structure required to evaluate the resonance strength, the relational database structure is examined in chapter 4.

This produces a NEEC rate, $R_{neec} = 27.96s^{-1}$ using the second narrow resonance approximation in equation 3.27, which only differs by 0.0001 if we do not use the narrow resonance approximations. Thus we are able to calculate the NEEC rate in this type of environment without having to calculate the NEEC width.

3.3.2 A Simple Example - An isomeric beam in a storage ring

A very different yet highly related approach is to present 'stationary' electrons to a stored beam of ions, circulating around a ring of accelerator magnets, kept at the resonance energy with a single RF cavity, within a narrow longitudinal and transverse phase space area. The 'cooled'³ electron beam is injected at one place, effectively at rest in the ion rest frame. This is equivalent to a constant stream of ions impinging a bath of electrons.

³By 'cooled' we mean: as having a low spread in transverse energy relative the electron beam direction of motion; the longitudinal direction

Again, there is no time dependence here, so the NEEC probability energy dependence is purely within the resonance fraction.

$$R_{neec} = n_{i-e} v_{res} \sigma_{res} \int_{E_{res}-\frac{\Gamma}{2}}^{E_{res}+\frac{\Gamma}{2}} F(E) dE \quad (3.32)$$

Which using a Gaussian collision distribution is equivalent to:

$$R_{neec} = N_{ion} n_{elec} v_{res} S_{pdb} \frac{2}{\pi \Gamma_{neec}} \frac{\Gamma_{neec}}{\sqrt{2\pi} \Delta} \quad (3.33)$$

This is compared to the definition of the NEEC rate described in reference [19] (equation 3.12). Assuming all NEEC's are detectable, this was expressed as:

$$R_{neec} = \frac{N_{ion}}{\delta t} n_{elec} \delta z \sigma_{res} \frac{\Gamma_{neec}}{\Delta} \quad (3.34a)$$

assuming no energy loss in the ion-electron interaction time.⁴ The target thickness δz , was set as $100 \mu m$ and the interaction time taken a result of the target thickness. This definition of the NEEC rate works only for this type of setup, and should there be any energy loss or temporal fluctuation, one should start with equation 3.13 and integrate correctly.

The collision densities in this setup are somewhat more modest $n_{i-e} = 10^{15}$ collisions cm^{-3} however, ions are continuously fed into a storage ring and thus once an ion has NEEC'ed it can be detected and removed via fast switching of a dipole separator, from the ring.

The NEEC rate for ^{57}Fe in this scenario is $0.466 s^{-1}$. Although this is lower than the EBIT, the NEEC yield will be larger over an experimental run due to an increased detectable fraction and long experiment running times. This is also promising if the best isomer candidate beams can be identified.

⁴assuming the integral $v(E)dE = \frac{dz}{dt}(E)dE = \frac{\delta z}{\delta t} dE$ which again implies the acceleration is zero since $\frac{dz}{dt}$ is constant and thus $\frac{dE}{dz}$ in $\frac{dE}{dt} = \frac{dz}{dt} \frac{dE}{dz}$ must be zero.

3.3.3 A More Realistic Example - Exposing the best combination of charge states

The NEEC rate for a specific charge state and capture channel is:

$$R_{neec}^{q,\alpha} = S_{pdb}^{q,\alpha} \frac{2}{\pi\Gamma_{neec}} \phi_e(E, T_e, n_e) \quad (3.35)$$

where as usual we have used a narrow resonance approximation and defined $\sigma_{neec} = S_{pdb} \frac{2}{\pi\Gamma_{neec}}$. The electron temperature will define some temporally static equilibrium charge state distribution and electron energy distribution.

The total NEEC rate then involves a summation if one considers all the possible charge states and capture channels (note the capitalised "NEEC" subscript to indicate a total NEEC rate)

$$R_{NEEC} = \sum_{q,\alpha} f_q R_{neec}^{q,\alpha} \quad (3.36)$$

where f_q sits on some discrete Gaussian-like distribution function and is defined by some equilibrium. The charge state restricts and summarises the available space and spin coordinates via a labelling of 'q'. The mean charge state is taken as the maximally occupied equilibrium charge state due to a balance of charge changing collisions within the equilibrium plasma. This distribution can be defined by the Saha equation, yet we resist using the local thermodynamic equilibrium (LTE) approach due to the lack of accuracy without taking into account the considerable photon flux in the non-LTE approach, especially at terrestrial densities [38].

3.4

NEEC Probability for Equilibrium-Plasma and Ion-Beam-Foil Parameters

As mentioned in chapter 1, NEEC and IC can be at an equilibrium, but only in an environment where there are highly charged ions and electrons colliding regularly. As such, there will also be many other capture and ionising processes in equilibrium at the same time, and thus the environment must be at a general thermodynamic equilibrium. This is only approximately true in terrestrial plasma environments for some time during their

expansion and so one must approximate how long this occurs, otherwise one must constantly heat and contain the plasma, which will restrict the electron temperature and thus its flux (such an environment is an EBIT). A question remains in the NEEC problem as to whether one should create a few short lived high-electron-flux plasma environments, or a longer lived low-electron-flux plasma environment.

Within a plasma, there is a distribution of charge states that exist statically within some volume of the plasma at local thermodynamic equilibrium (LTE), involving a detailed balance of collisional process or non-local thermodynamic equilibrium (n-LTE), involving a detailed balance of both collisional and radiative processes [38].

3.4.1 Plasma Rate - Approximately Temporally Static

As expressed in [39] the NEEC rate and yield in a plasma at thermodynamic equilibrium lasting for τ_p seconds is:

$$R_{NEEC} = \sum_{q,\alpha} \int \sigma_e^{q,\alpha}(E) \phi_e^q(E) dE \quad (3.37)$$

$$N_{NEEC} = R_{NEEC} \tau_p^{tot} \quad (3.38)$$

where the NEEC rate, R_{NEEC} is temporally static and thus depends energetically on only the electron distribution function and available resonant cross section. The plasma lifetime thus is an important factor in the figure of merit; the total plasma lifetime over an experiment $\tau_p^{tot} = \tau_p \tau_{exp} f_{rep}$ is dictated by the laser rep rate f_{rep} , and is a separable aspect of the FOM.

For now we will look at the NEEC rate R_{NEEC} as the figure of merit over an experimental campaign, and not worry about distinguishing this from competing nuclear excitation mechanisms such as Coulex, which will be examined in chapter 5. It is important of course to evaluate the NEEC rate [s^{-1}] within some quasi-equilibrium phase of a plasma expansion. We now look at how we can compute the NEEC rate from a macroscopic perspective in the Thermodynamic-Equilibrium (TE) plasma.

The resonant flux can as usual be weighted by some distribution function, which for simplicity in the first instance, one uses the classical Maxwell-Boltzmann distribution. However, when confined to an extreme extent, the electrons in the continuum will start

to exhibit wave-like behaviour, due to being so confined. The quantum mechanical density of states then produces a limit on the 'closeness' of the electrons; the electron distribution function would peak at a very different energy and depends also on the chemical potential of the plasma. We analyse if this is necessary for increase in the accuracy of the high density plasma calculations in section 3.4.3.

We in general use for the electron distribution function the Maxwell-Boltzmann distribution.

$$F_{MB}(E, T_e) = \frac{2}{\sqrt{\pi}} \left(\frac{1}{T_e} \right)^{\frac{3}{2}} E^{1/2} \exp\left(-\frac{E}{T_e}\right) \quad (3.39)$$

normalised as

$$\int F_{MB}(E, T_e) dE = 1 \quad (3.40)$$

T_e is the hot electron temperature of the equilibrium plasma and corresponds to the average kinetic energy of an electron in the statistical ensemble of electrons stripped off by the laser pulse, and in some short lived but definable equilibrium.

We need to find a suitable electron temperature that can be produced in a plasma due to a laser interacting with some kind of NEEC'able target species, producing an electron distribution function $F(E)$ that is a corollary of the accessible CSD. The NEEC yield is calculated in the next chapter for a wide range of Laser facilities, and we try to reason a method for evaluating the most promising combination of facility and plasma species. Restricting the parameter space to laser irradiance and repetition rate allows us to find maxima in the observable NEEC probability. Certainly if we restrict ourselves to a certain T_e, n_e parameter space then the optimisation becomes much simpler and more astrophysically applicable. Nonetheless the effective flux and active resonance strength must be approximated well, with evidence of its effectiveness.

To evaluate the resonant electron flux for each species, we need to know the electron temperature T_e and thus the resonance electron number density n_e , assuming the ion density is just the number of viable ions in the volume of the TE region that a certain laser facility can induce, and the electron temperature is equivalent to the ion temperature within equilibrium. We thus rely on various plasma approximations and hydrodynamic laser scaling laws using the method for non-local thermal equilibrium plasmas in [40],

extending the scaling used to Beg scaling at the highest laser irradiances.

Furthermore, where the plasma is hot but not so hot that it is fully ionised, there will exist an equilibrium between atomic electron capture and ionisation, resulting in a charge state distribution. Where this is the case we can find a maximal induced NEEC rate by finding (T_e, n_e) that exposes the best and most numerous NEEC resonance strengths. Otherwise if the species is fully stripped the parameter space is $(\text{Irradiance}, f_{rep})$, as one is only exposing the total resonance strength S_{tot} . This would be pure A(0)N0 defined in chapter 2; and although simpler, does not always expose the best part of the resonance spectrum.

The effective resonance strength using the total neutral ICC is used as an absolute upper limit for NEEC

$$S_{tot} = \frac{2\pi^2}{p_{eff}^2} \alpha_{tot} A_r^{d \rightarrow i} \quad (3.41)$$

where p_{eff} is the relativistic momentum (equation 3.21) calculated from the effective resonance energy E_{eff} due to the mean electron binding energy available for NEEC.

The interaction volume V_p is given by an approximate plasma volume, assuming a cylindrical plasma that has been bored through the target by the laser interaction.

$$V_p = \pi R_{focal}^2 d_p \quad (3.42)$$

with the focal radius R_{focal} defined by the laser facility and the depth $d_p = c\tau_{pulse}$.

This volume can also be made into a bunch of smaller contributing volumes (with defined n_e and T_e) to the whole interaction volume, defined by a sum of equations of type 3.23, should one want to run thermodynamic simulations of the plasma.

3.4.2 NEEC Yield - Expanding the Parameter Space

There is a critical density and temperature where the NEEC rate peaks over the effective energy E_{eff} rather than peaking over the fully ionised E_e . The number of excitations (NEEC yield) also seems to produce a discontinuity across a change in order of magnitude in the density, which will be explore in chapter 4. This is confirmed here and the stage set to examine this over the full NEEC database.

The lifetime of a TE plasma can be expressed as the product of the average electron velocity and the plasma radius [40], until an electron has traversed such a distance:

$$\tau_p = R_{focal} \sqrt{m_i / (T_e \bar{Z})} \quad (3.43)$$

For the highest irradiance facilities this massively underestimates the plasma lifetime by a factor $<10^{-3}$ and so we affix our equilibrium plasma lifetimes at 100ps.

The number of free electrons thrown into the plasma by the laser pulse, and thus the electron number density due to V_p , can be estimated via a fraction of the absorbed laser energy, f_{abs} , which is typically in the range 10% to 20%, no larger than 50% [40], and is calculated empirically using [40]

$$N_e = \frac{f_{abs} E_{pulse}}{T_e} \quad (3.44)$$

$$f_{abs} = 1.2 \times 10^{-15} I^{0.74} \quad (3.45)$$

where I is the intensity in Wcm^{-2} [41]:

And thus a bulk-total electron number density can be defined using these empirical approximations.

$$n_e^{tot} = \frac{N_e}{V_p} \quad (3.46)$$

This total number density is multiplied by a fraction defined by the shape of our impact energy distribution. The ion-electron density is expressed as previous.

$$n_{i-e} = N_{ion} n_e^{tot} F(E_{res}) \Gamma_{neec} \quad (3.47)$$

$$N_{ion} = \frac{N_e}{\bar{Z}} \quad (3.48)$$

N_{ion} is the number of ions that that exist in the plasma due to the target composition. An upper limit on the number of ions can be described via an average charge state \bar{Z} assuming the plasma is in a non-local thermodynamic equilibrium (n-LTE). We use the data provided by FLYCHK to assess the average charge states of all elements using the

data available between electron temperatures 0.5eV to 100keV, and number densities 1×10^{12} to $1 \times 10^{24} \text{ e}^- \text{ cm}^{-3}$, in chapter 4.

With these laser-plasma interaction approximations in place we provide an assumption that

$$R_{tot}(S_{tot}) \approx R_{NEEC} \quad (3.49)$$

when there is no charge state data available.

The NEEC yield over an experimental campaign using τ_p^{tot} is

$$N_{NEEC} = R_{NEEC} \tau_p \tau_{exp} f_{rep} \quad (3.50)$$

We must expand and analyse the approximations on R_{NEEC} to ensure the extent of its accuracy and calculability.

3.4.3 Quantised Regime of Electron Distribution Function

The resonant flux is weighted by some distribution function, which in a very dense, but not so hot plasma, one uses the Fermi-Dirac distribution f_{FD} [41], defined by the temperature of the electrons T_e , as well as the chemical potential μ .

$$\phi_{FD}(E)dE = g_e(E)f_{FD}(\mu, E, T_e)v(E_e)dE \quad (3.51)$$

where the total ion-electron density, via the laser parameters and average n-LTE charge state, at a specific impact energy, is evaluated as a product of the density of continuum electronic states g_e multiplied by the Fermi-Dirac function [40].

Here a normalisation is applied to give a bulk average electron number density n_e^{tot} over the entire impact ion-electron energy range in the plasma

$$\int_{\Delta} g_e(E)f_{FD}(\mu, E, T_e)dE = n_e^{bulk} \quad (3.52)$$

with the Fermi-Dirac distribution f_{FD} defined as:

$$f_{FD}(E, T_e) = \frac{1}{e^{(E-\mu)/T_e} + 1} \quad (3.53)$$

In combination with the average atom model [5], one can use the Fermi-Dirac statistics of the continuum to then assert details of the charge state of the average atom (via conservation of space). The proportion of empty sites on the atom is thus defined as

$$P_b = 1 - f_{FD}(-V_i) \quad (3.54)$$

We elect to use a full n-LTE calculation using FLYCHK to calculate this, which will be considerably more accurate.

In equation 3.58 the density of continuum electron states is defined as [38]:

$$g_e(E)dE = \frac{4}{\sqrt{\pi}} \left(\frac{2\pi m_e}{h^2} \right)^{3/2} (E)^{1/2} dE \quad (3.55)$$

To evaluate the necessity of this model, the degeneracy factor is a good measure of the extent of overlap between the electron wavepackets [38]

$$\theta_d = \frac{T_e}{E_F} \quad (3.56)$$

where E_F is the Fermi energy. When $\theta_d \ll 1$ the average distance between electrons is much smaller than their deBroglie wavelength and a degeneracy pressure will be exerted on the electrons, decreasing the overall flux from the MB value. This only occurs in plasmas with $n_e > 10^{28} \text{e}^- \text{cm}^{-3}$, which is beyond the densities considered in this work. An example of the MB compared to the FD electron flux is shown in figures 3.4 and 3.5. As a limit for lower temperature, so long as the electron temperature remains above 50eV and the electron number density below $10^{24} \text{e}^- \text{cm}^{-3}$, the degeneracy factor will always be > 1 . It is unlikely an atom will be charged enough to induce NEEC at $T_e < 50\text{eV}$ and so we assert that in a terrestrial plasma, using the MB distribution is accurate.

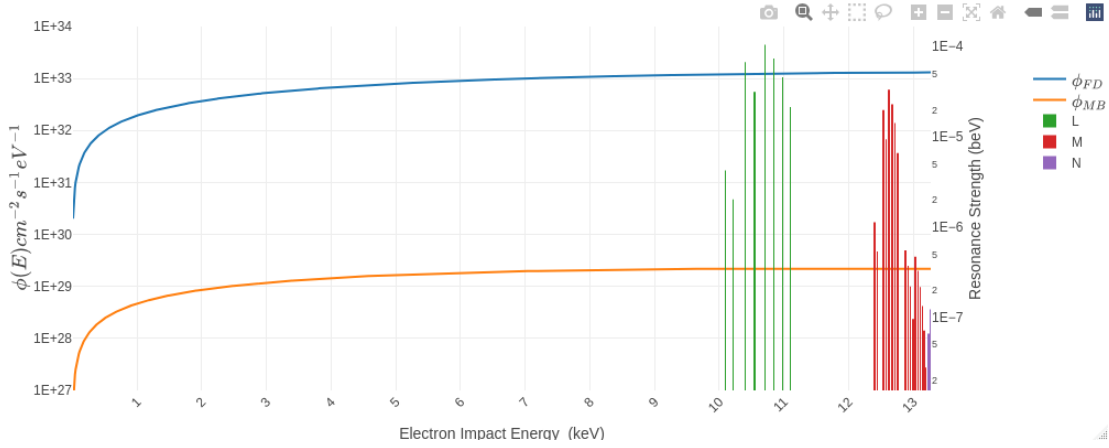


FIGURE 3.4: Electron Flux at $T_e = 12\text{keV}$ and $n_e = 10^{24}\text{e}^-\text{cm}^{-3}$. The degeneracy factor in these conditions is $\theta_d = 329$

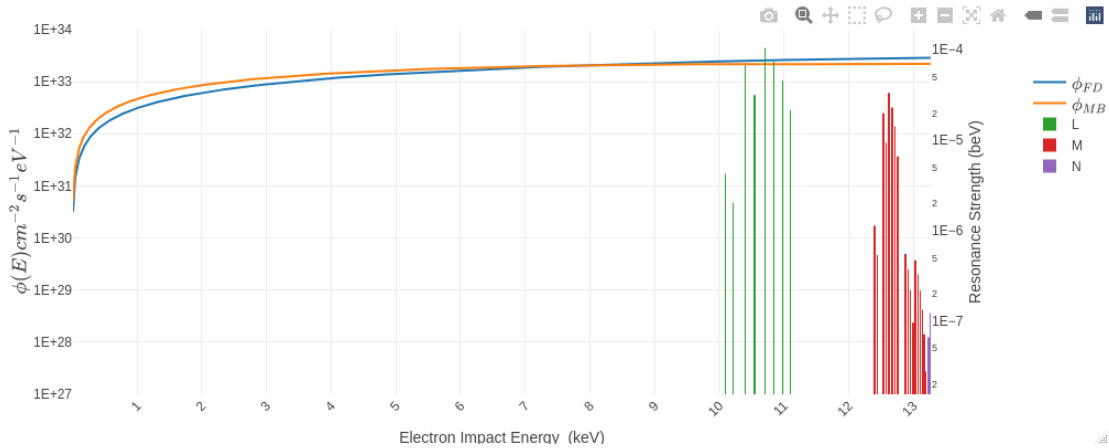


FIGURE 3.5: Electron Flux at $T_e = 12\text{keV}$ and $n_e = 10^{28}\text{e}^-\text{cm}^{-3}$. The degeneracy factor in these conditions is $\theta_d = 0.709$

3.4.4 Electron Distribution Function at Equilibrium - Hot Dense but not too dense plasma's - $T_e \gg |V_1|$

In a laser-solid interaction, the electron temperature produced by the interaction is approximated with various scaling laws, that are appropriate depending on the laser parameters. The intensity and wavelength of a laser are defined for each facility, and thus is the laser's irradiance, $I\lambda^2$ (with λ defined as the wavelength of the laser in μm and I the intensity in Wcm^{-2}), which is proportional to the electric field amplitude of the laser (hence the strange units $\text{Wcm}^{-2}\mu\text{m}^2$). This scales to the maximal electron temperature which we can reach via a laser pulse. The number of electrons that we can ionise is approximated empirically via 3.44, yet their average kinetic energy must be defined

by a further scaling law. In [41], for a cold-dense plasma with sharp edged profiles, the electron temperature is approximated using the ponderomotive scaling law, which is appropriate for an XFEL laser-solid interaction irradiance $<10^{15} \text{ Wcm}^{-2}\mu\text{m}^2$ [40].

$$T_e \approx 3.6I_{16}\lambda_\mu^2 \text{keV} \quad (3.57)$$

where the intensity of the laser I_{16} , in units [10^{16} W/cm^2], is defined by the energy of the laser divided by the product of the temporal pulse length τ_{laser} and the focal spot size πR_{focal}^2 . Each laser facility will have a defined maximal value of these parameters.

More valid across a wider range of intensities is the short-scale length profiles approximation, which we use for irradiances $< 3 \times 10^{16} \text{ Wcm}^{-2}\mu\text{m}^2$.

$$T_e \approx 8(I_{16}\lambda_\mu^2)^{1/3} \text{keV} \quad (3.58)$$

Finally for the highest irradiances we use the scaling suggested by Haines *et al* (also referred to as Beg scaling), for irradiances $> 3 \times 10^{16} \text{ Wcm}^{-2}\mu\text{m}^2$ [42]:

$$T_e \approx 215(I_{18}\lambda_\mu^2)^{1/3} \text{keV} \quad (3.59)$$

As the electron density increases one has to impose more and more limits on the ability of the plasma to exchange heat locally, due to effects such as plasma mirroring. Thus although for irradiances above $10^{18} \text{ Wcm}^{-2}\mu\text{m}^2$ Beg scaling is not necessarily accurate, but undoubtedly it remains an upper limit.

The main high power laser facilities have been tabulated via their maximum Irradiance and repetition rate (shown in figure 3.6) which will allow us to compare the maximum NEEC yield for a fully ionised plasma.

The electron temperature considered for these facilities is presented along with the scaling laws in figure 3.7.

So using the above definitions, and the assumption that at these high-power facilities the plasma is hot enough to be fully ionised, one can affix the summation 3.36 to over $A(0)N_j$ and all of the excited state $A(0)-X-N_j$ channels (fully stripped and the j th isomer). This will provide Z possible resonance channels. The lowest available will be into the $A(0)N_j$ and all others will be into excited states that are approximated as an upper limit

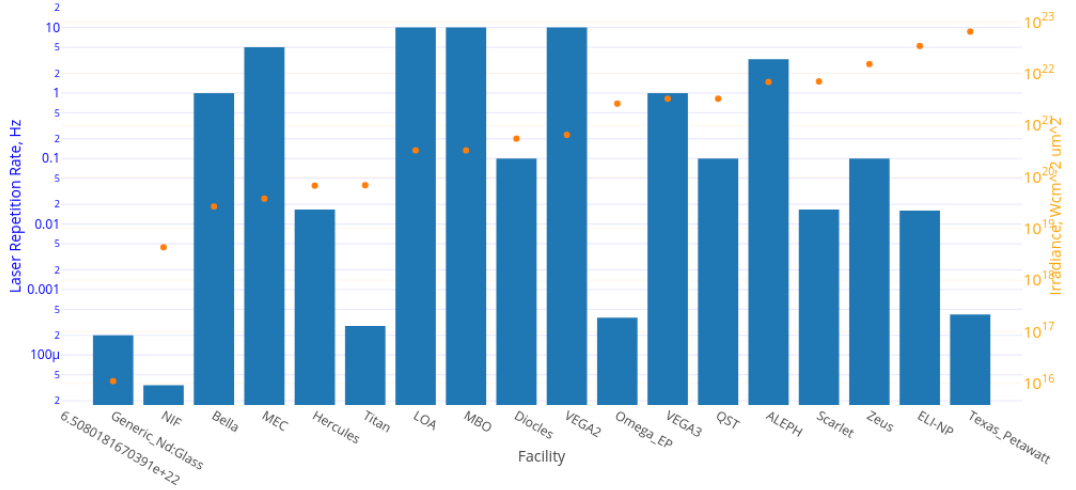


FIGURE 3.6: High power laser facilities considered, left axis: Repetition Rate. Right axis: laser irradiance. For each of these laser induced plasmas, one expects a maximum plasma lifetime of 100ps

as $A(i)N_j$ resonances. Notably, with the narrow resonance approximations used, the Γ_{neec} term cancels in the calculation of the NEEC rate, so we are unaffected by the increase in NEEC width for $A(0)-X-N_j$ cases. The NEEC rate can be separated into a microscopic part and the facility only affects the macroscopic part. The available spectrum for the ^{57}Fe 14keV M1 nuclear transition is shown in figure 3.8. Note although the resonant fraction is $\sim 10^{-10}$ the total upper limit NEEC's per week for an irradiance at a Beg scaling facility considered is $\sim 10^{12}$, assuming a maximal possible number of ions using equation 3.48.

$$N_{neec} = \left(\frac{f_{abs} E_{laser}}{T_e}\right)^2 f_{rep} \frac{\tau_p \tau_{week}}{V_p Z} \sum_{\alpha_i}^Z F(E_{res}^\alpha) v_{res}(E_{res}^\alpha) S_{neec}^\alpha \quad (3.60)$$

$$\sum_{\alpha_i}^Z F(E_{res}^\alpha) \approx F_{MB}(T_e = E_{eff}) \quad (3.61)$$

We can then use a linear approximation on the increase in the electron distribution across the atomic resonance spectrum, and take the value of the distribution function that is at the mean impact energy across this range. One can assert that this completely separates macroscopic and microscopic and we are able to select the best facility by a purely macroscopic factor: one can then choose macroscopic and microscopic cases separately, as the former has a constant effect on all the latter.

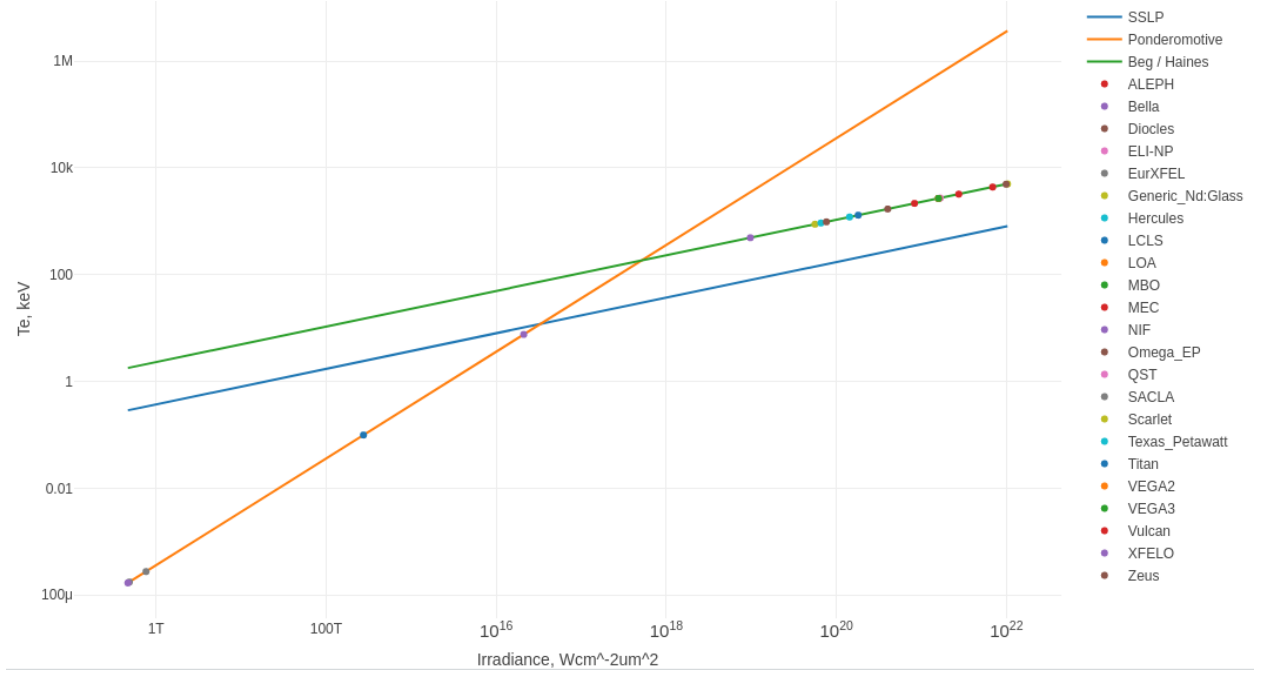


FIGURE 3.7: We see the XFEL Irradiances that have already been analysed by Pálffy *et al* [43] which use Ponderomotive scaling, and the highest irradiance facilities (Beg scaling) which we consider in our (T_e, f_{rep}) analysis

We can therefore define a time integrated NEEC flux, which can be calculated as a figure of merit without having to calculate the NEEC resonance strength. From this we can quickly make a conclusion on the best laser facility required for each nuclear transition.

$$\Phi = \left(\frac{f_{abs} E_{laser}}{T_e} \right)^2 f_{rep} \frac{\tau_p \tau_{week}}{V_p} \frac{2\sqrt{T_e}}{\pi D} \exp(1/D) \quad (3.62)$$

where $D(=1)$ is the chosen divisor for electron temperature, assuming it is tuned to E_{eff} . The implications of this will be discussed in chapter 4.

We will analyse in chapter 4 the irradiance region $\sim 10^{17} \text{Wcm}^{-2} \mu\text{m}^2$ where the plasma will be only partially ionised, and thus there will be a charge state distribution, and a codependence of the microscopic and macroscopic parts of the NEEC rate. We will need to use a general upper limit approximation for all excited state atomic capture channels.

The atomic ground state capture channel is over-scaled so as to include the full spectrum of atomic excited state capture channels.

$$A(i)N_0 \geq \sum_i^Z A(0)X_i N_0 \quad (3.63)$$

The results of this are presented in chapter 4 as an experimental tool for designing

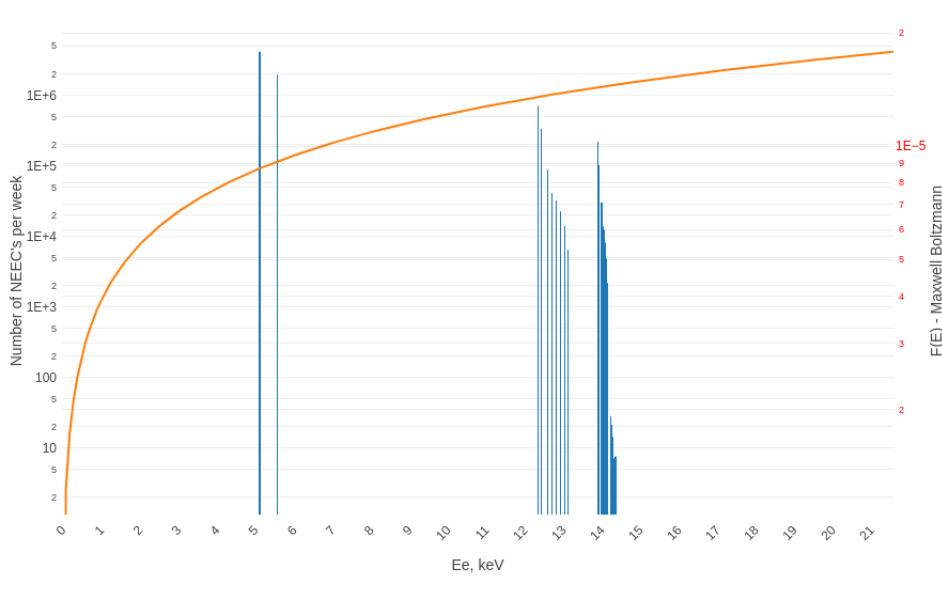


FIGURE 3.8: 26 NEEC resonances available for fully ionised ^{57}Fe . The lowest energy resonance will be $^{57}\text{Fe}(0)\text{N}0$ whilst the $^{57}\text{Fe}(0)\text{-X-N}0$ resonances are overestimated via $\text{Fe}(i)\text{N}0$ resonances. One notices the MB distribution must be increasing with impact energy, for the fully ionised simplification to be valid

a NEEC plasma experiment, along with the available candidate transitions one should consider. Note for the medium irradiance facilities, where the thermal population of electrons peaks within the ionisation energy range of the species, the introduction of a charge state distribution vastly increases the number of available resonance channels; which can outweigh the fact that the plasma won't be as hot and dense. Notably the macroscopic laser parameters will affect both the macroscopic factor Φ , and the actual number of microscopic resonances. Next we will examine an environment which is seemingly the most simple to design, yet as we see so far it is wrought with complexities.

3.4.5 Cooler Plasmas - $T_e \sim |V_1|$

As mentioned, if the peak of the electron distribution function is within the ionisation spectrum of the atom, then one will expect a thermodynamic equilibrium to exist in a local (collisional) or non-local (radiative) sense. This creates a charge state distribution.

We use FLYCHK in this section to calculate the charge state distribution of the plasma. This code uses a full collisional-radiative model (non-LTE) to calculate the balance of collisions and radiative atomic processes [44].

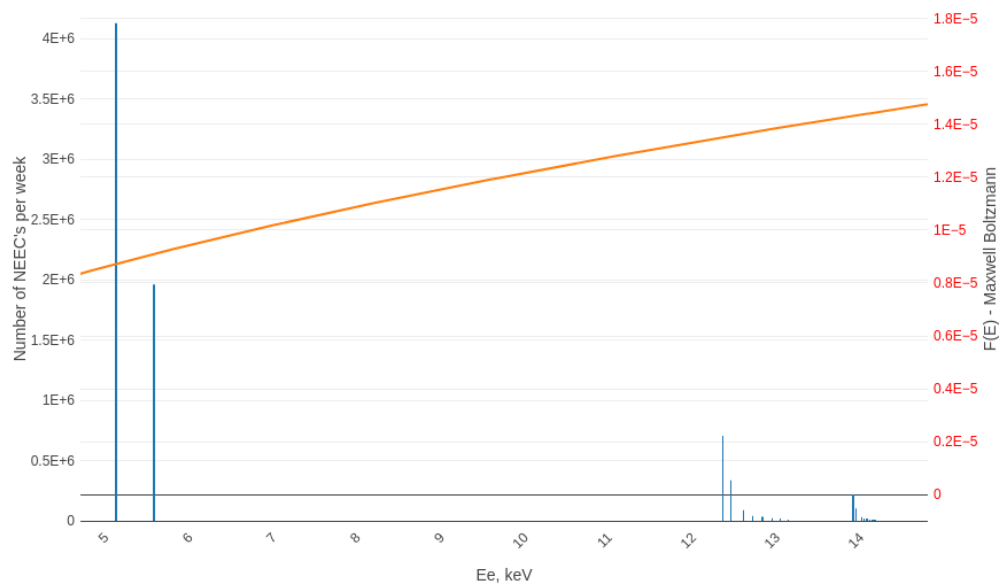


FIGURE 3.9: Linear scale of figure 3.8 to demonstrate the variation of the MB distribution across the resonance spectrum

A candidate example studied commonly is the pertinent NEEC case of ^{93m}Mo . There is a full data set of $^{93m}\text{Mo}(\alpha)$ and $^{93m}\text{Mo}(\alpha)\text{-X}$ data with *ab initio* NEEC resonance strengths and energies. Access to the raw data set has been kindly granted by A. Pálffy and Y. Wu, and has allowed some scope for sanity checking our macroscopic calculations.

The most prominent graph at this stage is figure 3.10, which shows a good agreement in our NEEC rates (calculated using the various levels of approximation detailed below) compared with those computed using the *ab initio* resonance strength data. The red data calculates the resonance strength using an equivalent hydrogenic type subshell at all 334 energies and resonance channels within the *ab initio* data. Clearly if all the resonance channels are identified in a dataset, a new type of scaling of the neutral ICC's for NEEC-X channels should be used.

The orange data is easy to calculate and uses α_{tot} and an effective energy E_{eff} calculated from the mean energetically available $|V_i|$

The yellow data is using the scaled subshell IC coefficients (using equation 2.22) for ground state atomic capture channels only, and although still an overestimate at the optimum temperature, it predicts the optimum temperature well (and supports the approximation 3.63). This NEEC rate is plotted across all FLYCHK densities in figure 4.16 in chapter 4.

The Green data is my calculation of the R_{NEEC} using the full *ab initio* dataset provided by Pálffy and Wu and matches the published values of R_{NEEC} in [33] and [40] for all densities calculated.

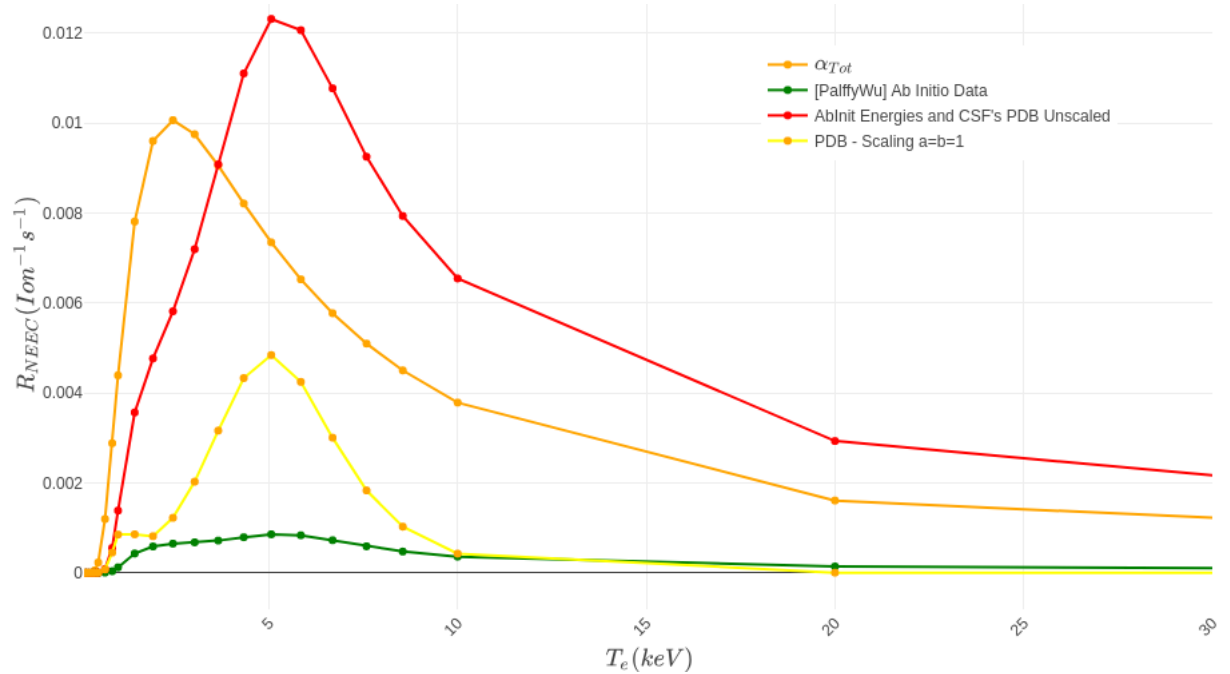


FIGURE 3.10: All the R_{NEEC} calculations overview for the plasma described above using the dataset provided via correspondence with Pálffy and Wu. The dataset is that used in [33] and rates consistent with those published [40]

Predominantly, one must note from figure 3.10 that although our scaling is most certainly appropriate using the theoretical data provided in this case [33] [40], more so it is very likely due to the PDB that our use of the total neutral ICC resonance strength (Orange line) is consistently an upper limit of our total atomic-nuclear excitation threshold, and so allows for a single calculation per candidate NEEC transition as the proper figure of merit for microscopic candidate selection over all proper plasma macroscopic scenarios. A further comparison of this *ab initio* data set is summarised for the Beam-Foil approach in the next subsection.

3.4.6 Nuclear Beam Impinging a Thin Solid Target - Temporally dynamic

If the bath of available electrons is at rest, then we can accelerate ions into them to provide the resonance collision energy. This was first proposed in 1989 as the so called "Nuclear Excitation by Target Electron Capture" [45], in which the target electrons were provided

as the weakly bound electrons experienced by a beam of ions travelling down a crystal channel (explored in detail in chapter 5). Let us first consider a simplistic version of events, with an ion travelling through an amorphous solid target, as compared to an under-dense stream of electrons in an electron beam. The capturable electrons in this scenario will be bound or weakly bound electrons in the solid quasi-continuum distribution of electron velocities.

For target electron capture, one provides the resonance energy as the beam energy, which we convert from the ion rest frame to a beam energy in the lab frame as [46]:

$$E_{ion}^{res} = \frac{M_{ion}}{m_e} E_{res} \quad (3.64)$$

Once the beam enters the target, ions in the beam will lose energy in a well approximated way, according to the Bethe-Bloch formula via the program SRIM [47]. The impact energy experienced by the beam a certain distance, z , through the target is:

$$E_{exp}(z) = E_{entrance} - \int_z^{z+\delta z} \left(\frac{dE_{ion}}{dz}(E) \right) dz \quad (3.65)$$

The thickness of the target for which the resonance occurs is δz , which requires a slow variation of the continuum energy w.r.t. the resonance width (another narrow resonance approximation)

$$\delta z = \frac{\Gamma_{neec}}{\left(\frac{dE}{dz}(E_{res}) \right)} \quad (3.66)$$

So for a stream of ions entering the target monoenergetically, at a specific time, the resonance flux is

$$\phi_{res}(t, E) = n_{i-e} v_{res}(t, E) \quad (3.67a)$$

$$= n_e \phi_{target} \frac{dz}{dt}(t, E_{res}) \quad (3.67b)$$

where $\phi_{target} = N_{ion}/\tau$ is the number of ions per second per unit area that enter the target volume (and is assumed to be constant, which may not be the case as discussed in section 3.4.7).

Using the generalised NEEC rate

$$R_{neec} = S_{exp} \frac{2}{\pi \Gamma_{neec}} n_e \phi_{target} \int_{\tau} \frac{dz}{dt} (E_{res}) dt \quad (3.68a)$$

$$= S_{exp} \frac{2}{\pi \Gamma_{neec}} n_e \phi_{target} \delta z \quad (3.68b)$$

$$= S_{exp} \frac{2}{\pi \Gamma_{neec}} n_e \phi_{target} \frac{\Gamma_{neec}}{\frac{dE_{ion}}{dz} (E_{res})} \quad (3.68c)$$

where we assess the probability per beam particle as $\frac{N_{neec}}{N_{ion}} = \frac{\tau R_{neec}}{\tau \phi_{target}}$ as in equation 2.19 and assume each ion impinging the target can only NEEC once, and that the target has a unit of area [cm²].

And so we end up with a probability per beam particle for each resonance channel (ignoring the factor $2/\pi$):

$$P_{neec} = n_e S_{exp} \frac{1}{-(dE_{ion}/dz)} \quad (3.69)$$

The total NEEC probability, summing over all possible charge states and capture channels, and converting to the collision energy to the ion rest frame in 3.64, is then⁵

$$P_{NEEC} = \sum_{q,\alpha} n_e S_{exp} \frac{M_{ion}}{m_e} \frac{1}{-(dE_{ion}/dz)} \quad (3.70)$$

where S_{exp} is the effective resonance strength experienced within the NEEC experiment time, τ . S_{exp} could vary broadly depending on the species and the type of environment introduced, and it will be less than the theoretical value due to the equilibrium charge state through the target. A summary of the relationship of the different resonance strength approximations is provided as:

$$S_{exp} < S_{NEEC} = \sum_{q,\alpha} S_{neec}(\alpha) \approx \sum_p S_{pdb}(\alpha_p) < S_{pdb}(\alpha_{tot}, E_{eff}) \quad (3.71)$$

My analysis of the ‘discovery’ experiment consists of using $\sum_p S_{pdb}(\alpha_p)$ to calculate the resonance strength. Here we have created an upper limit in the theoretical and experimental calculation of the NEEC depletion probability, by assuming all capture channels

⁵which was published for the first time in [33] although simultaneously surmised in [48], the second year report of this PhD, which has led to correspondence with the Max Plank institute.

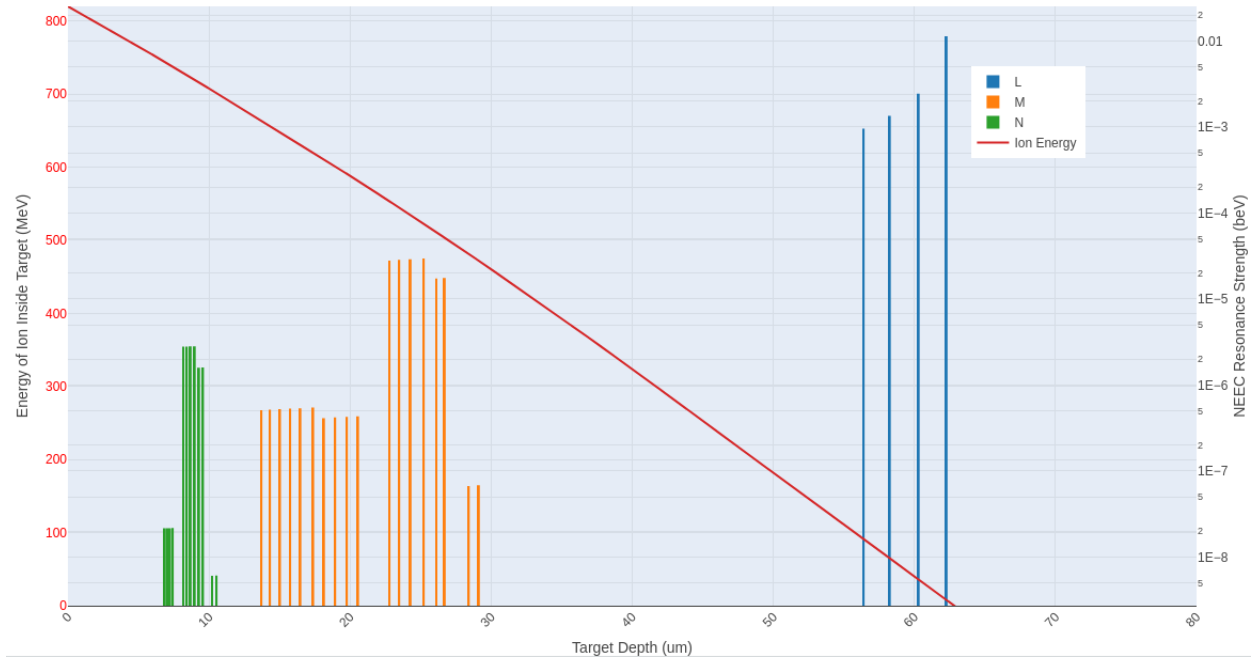


FIGURE 3.11: My upper limit is $P_{NEEC} = 9.38 \times 10^{-8}$. The energy of a beam particle is calculated using a grid of $\frac{dE}{dx}$ values provided by SRIM [47] for energies between 0 and 1GeV in steps of 50MeV

remain open during the passage of Mo through the C target (figure 3.11), and that all bound C electrons can be captured. This places an *absolute* upper limit on the NEEC probability of $P_{NEEC} = 9.38 \times 10^{-8}$. This probability using neutral ICC's allows for the possibility of X-NEEC occurring due to inner shell vacancies that could well be created during passage through the target.

In [22] it was stated that the coulomb excitation probability in this experiment had an upper limit between 3×10^{-6} and 2×10^{-4} which coincides with the depletion probability measured in [32] as 2×10^{-5} , in which the experiment was repeated by removing the ^{93m}Mo from its fusion evaporation reaction source, thus eliminating any background. This sheds further doubt that NEEC was the mechanism responsible for depletion, yet still the experiment remains fascinating since there is as yet no mechanism to account for the observed depletion probability of $P_{exc} = 0.01$.

3.4.7 A comment on luminosity

The luminosity in particle physics, especially where two beams (with well defined phase-space's) are colliding could be expressed as [49]

$$L = \frac{1}{\sigma} \frac{dN_{det}}{dt} \quad (3.72)$$

What they are saying here is that the rate of production of detectable particles is characterised by the luminosity of target particles by available injected particles and is larger for small cross section... The particles with high luminosity are good because they are effective. For the same detectable collision the cross section could be small but we still ascribe a large luminosity.

Which dimensionally is the same as our resonance electron flux ϕ_e times number of target particles illuminated. Luminosity though is rather a terse parameter in this situation, especially in trying to fine tune nuclear beams to interact with the atomic regime in a complicated electron target that involves solid state density functionals. The resonance flux arises and is defined independently to the cross section, and yet the detectable number is not necessarily a function of only the NEEC excitation number, due to many competing nuclear excitation mechanisms.

The particle physics experimentalist measures a slowly-varying cross section by rearranging equation 3.72 and integrating over time. The accelerator physicist will provide the integrated luminosity $L_{int} = \int_{\tau} L dt$ (which is the number of feasible incident particles), and the experimentalist the number of detected events (the integrated detectable rate... the number of detected events). One should be able to extract an average cross section from this by including detector efficiency:

$$\sigma = \frac{N_{events}}{L_{int}} \quad (3.73)$$

...this should be reevaluated since it was assumed the integrated luminosity was just the number of ^{93m}Mo particles generated by the incident beam. The accuracy of the NEEC depletion reported in this experiment still remains under question, and the experiment should be repeated by re-accelerating the Mo isomer into a controlled electron target (such as an electron cooler at a storage ring) so that L_{int} is implicitly measured in the experiment, whilst using the implantation technique used in [32] to separate the background.

3.5

Parameters for the Best Candidate Experiment

Considering conditions to be met upon a massive range of possible collisions, it is reasonable to commence an all inclusive search of the available nuclear and atomic states, under some upper-limit experimental constraints. There are several approaches experimentally as we have seen, and we will analyze the leading results of a candidate search across the nuclear chart in chapter 4.

We use the term '*candidate system*' to describe an isolated (relatively) stable system of nucleons (a nuclide), with some orbiting electrons bound to the nuclear system, and a separate continuum of intermittently available capturable electrons. This system will then be a candidate for this rare nuclear excitation, once a suitable electron is captured upon 'collision'.

We know that there are two cases for the nuclear level scheme that will involve different computations for the NEEC microscopic cross-section; ground-state and isomeric. Similarly there is the option of capture into ground and excited *atomic* states, which in combination with a distribution of charge states can change the number of available resonances by as much as $Z(Z-1)$. We have accounted for this by using over-scaled ground atomic state capture channels.

Irrespective of the case(s) we choose, to maximize the probability of NEEC from an experimentalist's point of view, we must satisfy as far as possible the following criteria:

- (i) Maximal capturable number of electrons energetically, $F(E)$, within a maximal collision density, for the longest amount of time.
- (ii) A non-vanishing total resonance strength that is as large as possible (this would require selection of the correct nuclide and distribution of charge states, accessible by the experimental energy space explored, available due to energy conservation in 3.1). This is difficult to balance with (i).
- (iii) Excitation via NEEC that is distinct from excitation via other mechanisms
- (iv) NEEC Excitation that is detectable.

It has become clear, that satisfying all these conditions simultaneously could be difficult and even contradictory in designing the best NEEC environment. At this point we are trying to construct a *method* for maximising the likelihood of a NEEC observation.

3.5.1 The Big Data Approach

By understanding the extent that a nucleus couples with its electron cloud, we can at least choose strong candidates that satisfy criterion (i) and (ii) simultaneously. Doubtless it is important to generate a figure of merit, so each candidate nuclear transition and experimental approach can be compared explicitly.

The proper FOM will have the form of a functional $F[i, ii, iii, iv]$, which one maximises in a high dimensional parameter space. Such an analysis is beyond the scope of this thesis, and we consider just the upper limit NEEC excitation number, and apply actual known facility values to place points in this parameter space. Eventually one can evolve this analysis into its proper mathematical form; but first one must be able to both predict and observe NEEC in a consistent repeatable fashion, which as yet there is no evidence of.

To maximise (i) and (ii) simultaneously we must write a data base framework which includes all observed atomic and nuclear data we know of, and theoretical where appropriate, yet make it accessible to the experimenter and the theorist. Both can then fill in the proper functional accordingly.

Chapter 4

Finding a not Knowingly

Over-promised NEEC Enviroment

As we have seen, a NEEC rate can be approximated as an upper limit via the PDB, and P_{NEEC} or more importantly N_{NEEC} , well defined as a result, using microscopic and macroscopic parameters that have been well tabulated. Namely, the ENSDF database [50] contains all exhaustively evaluated nuclear parameters, whilst NIST [51] and BrIcc [6] are instructive for observed and theoretically agreed upon electronic eigenvalues.

There have been both theoretical and experimental attempts to evaluate the NEEC rate with varying precision and success as described in chapter 3. Though understandably there has been little done as to expose what each of these calculations imply across the full range of known experimental parameters. Generally the focus of literature has been on methods from a single topology; exposing the most strong and numerous resonances for each ion charge state of a specific nuclear transition. To compute all possibilities without a large model-dependant computation, one must produce an upper limit and be able to search through all we know about an atom and its ionic states, via experimentally tabulated microscopic parameters. We must know, if using an upper limit estimate of all scenarios, is it viable to even try to observe NEEC terrestrially, and if it is, can we experiment on it in a way that can be compared to astrophysical, or at least theoretical data?

The only way we can unpick a way forward is to treat the theory as a black box and use the PDB as an upper limit. One can be pragmatic by using the energy balance in 3.1 and by using known IC coefficients that have been appropriately scaled in the previous chapters. Now we will present various trends in nuclear and atomic data, which will

provide evidence that our approximations are sound, and allow us to set up a global analysis of NEEC.

Previously, a survey was published on nuclides suitable to photoexcitation [52], and although it should be considered alongside the results in this chapter, the results were not of high enough energy for astrophysical plasma applications, since the survey was conducted for nuclear transitions below 30keV.

4.1

Trends in Nuclear and Atomic Data

4.1.1 Atomic Binding Energies - National Institute of Standards and Technology (NIST) Atomic Spectra Database

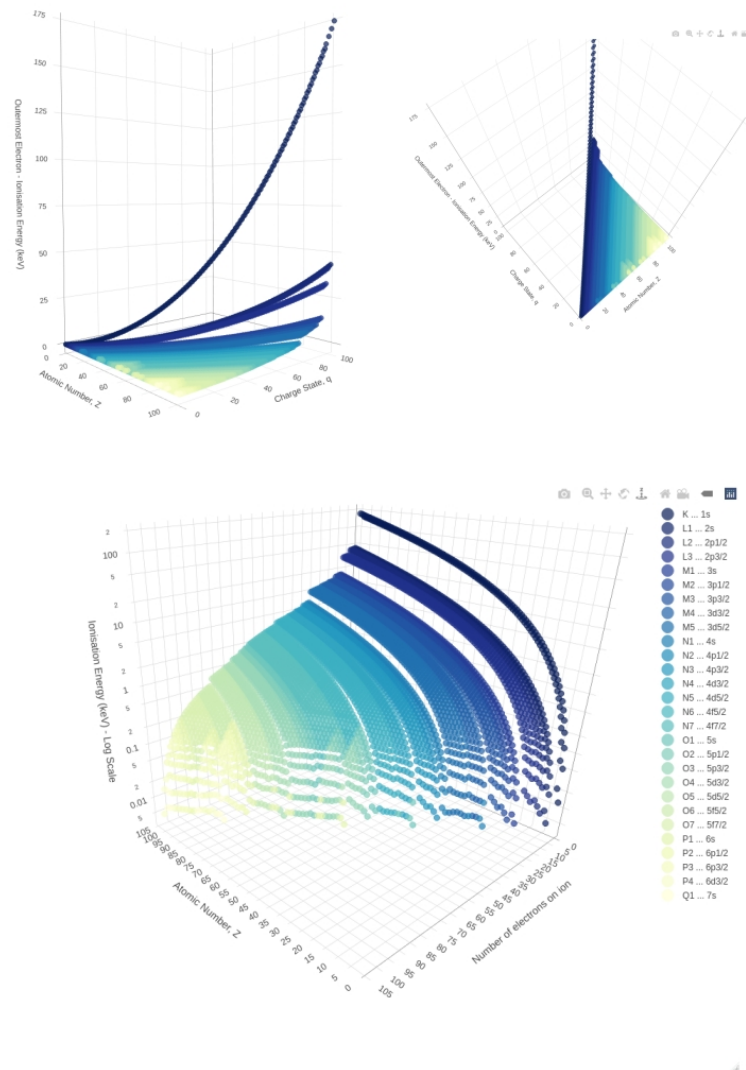
The atomic scale has such a prevalent affect on our existence that many names have been given to the different realms of atomic electron occupation, such as the transition metals or the alkali earth metals or "the Lanthanides", each indicating some leading effect of their natural configuration. The periodic table provides a good idea of the valence electrons that are responsible for an elements natural state.

The NIST database [51] is freely available and one can download all ground state binding energies with <20 clicks and some reasonably simple data wrangling code.

As already mentioned in the theory chapters the subshell splitting is averaged for each spin-orbital pair, although for heavy atoms the splitting is so extensive for outer shells it is impossible to define a consistent configuration sequentially in energy; due to configuration interaction ('Breit interaction' - which is a 'many-body' effect beyond Coulomb interaction of static point charges) and due to deviations from the $1e^-$ Aufbau principle using a non-Hydrogenic labeling basis.

The NIST atomic consecutive ionisation energies for $Z < 104$ are shown in figure 4.1, which we use as binding energies of the i 'th electron on the atom. This constitutes the $|V_i|$ 'th binding energy of all $AiNj$ cases in our analysis.

One sees a continuous evolution over the energy of the subshell filled, with the configuration averaged over the subshell. There are discontinuities in the configuration averages in the outer shells, where we would expect NEEC to be largely irrelevant.

FIGURE 4.1: All atomic ionisation energies from $1 \leq Z \leq 104$

In figure 4.2 we look specifically at 2 plots across the diagonal of the horizontal plane in figure 4.1. This shows a considerable staggering in energy for all elements for all the first ionisation energies; implying a strong many-body interaction in the Hamiltonian. This staggering is however considerably smoothed for all the 45th ionisation energies, implying the coulomb part of the Hamiltonian is dominant. It would be commensurate in the second case to label each configuration by only its subshell, even just its shell.

We look at consecutive ionisation energies (taken from NIST) of specific elements in figure 4.3 as well as neutral binding energies (extracted from the BrIcc tool) with the same hydrogenic configuration, the data structure used to calculate part of the the ICC scaling

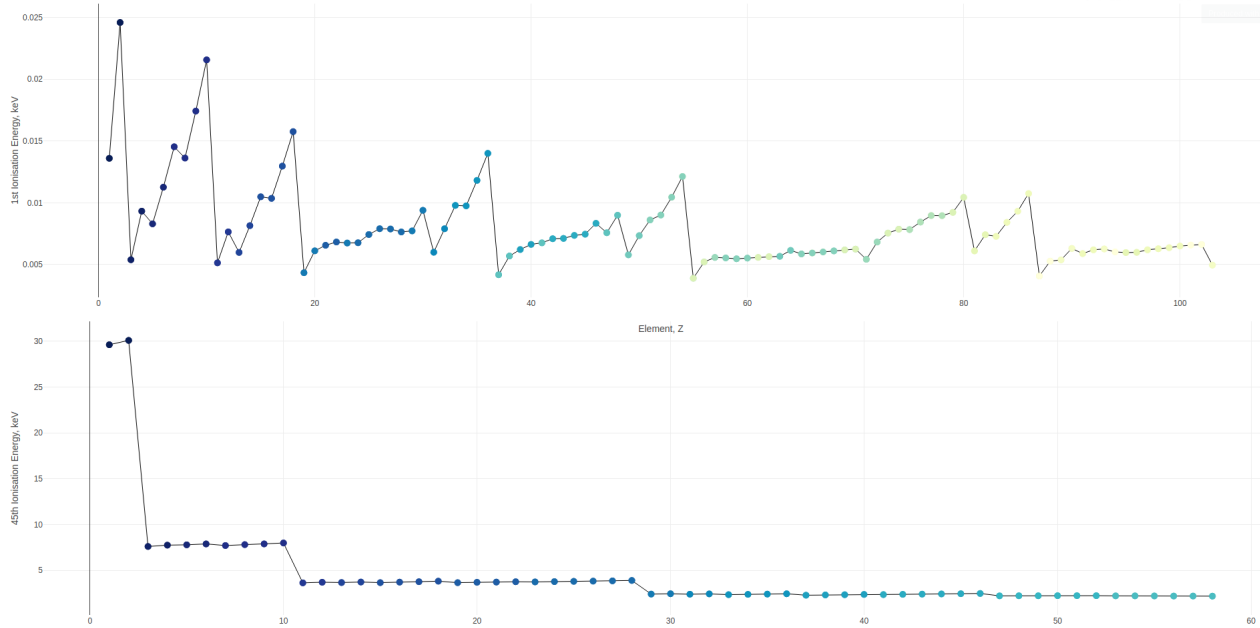


FIGURE 4.2: Top:1st (Z-1) and bottom: 45th (Z-45) ionisation energies across the elements

coefficient in equation 2.22. One can see a smooth variation across a subshell, with sharper variations when changing subshell. One also notes that by matching the data by its nlj configuration, consecutive ionisation data can be reliably matched to equivalent neutral binding energies. Where a neutral binding energy is unavailable for a configuration, it is made equivalent to the consecutive ionisation energy; so that the ICC is not scaled to infinity. When NEEC from an excited atomic state (X-NEEC) is possible, this will be due to the nuclear transition energy lying inbetween the green and yellow lines in a subshell (figure 4.3). By using an unscaled total neutral IC coefficient and the effective energy E_{eff} , one can expect the overestimate to included contributions due to X-NEEC.

For the candidate search program, constraints on the BrIcc calculator, and restraints on what we know about the heavy elements, we constrain the available elements in our search to $10 \leq Z \leq 104$.

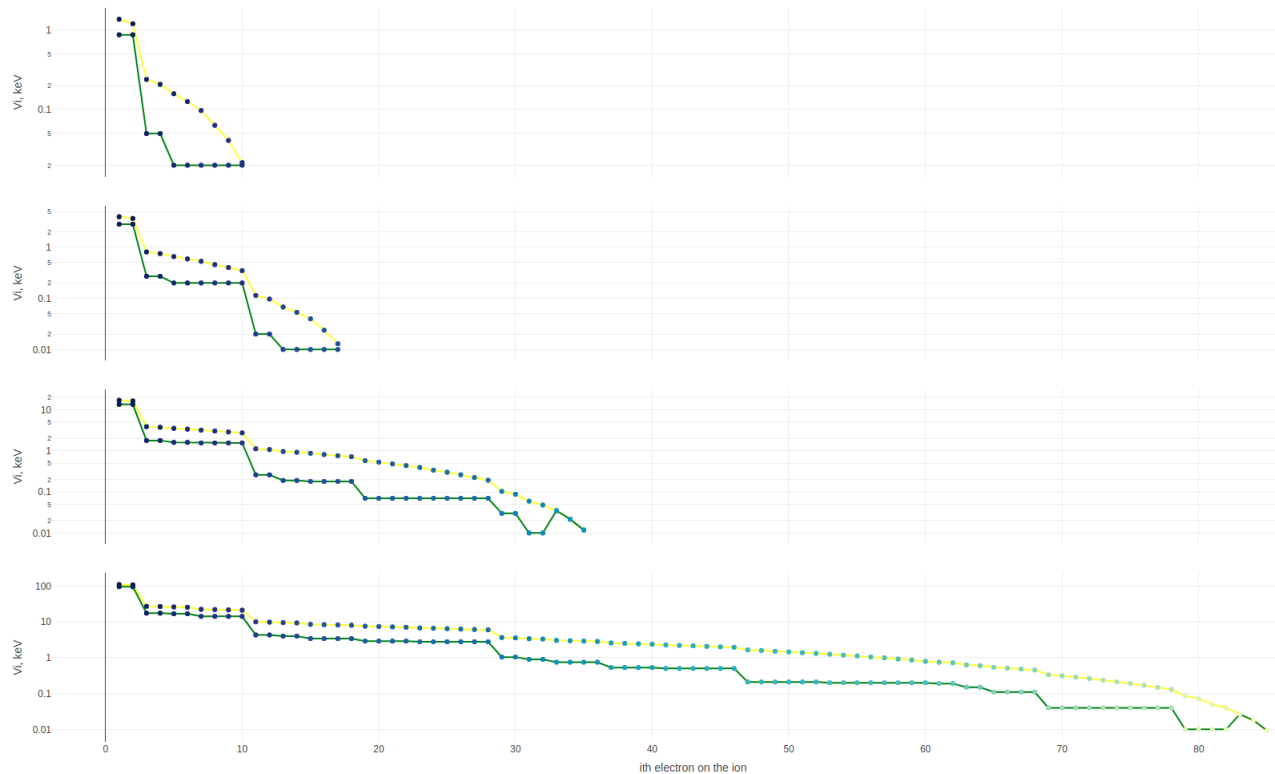


FIGURE 4.3: Consecutive ionisation energies and neutral atom binding energies of each electron in the elements, $Z=10, 17, 35$ and 85 respectively. The ratio of these values within an atom times the subshell occupancy ratio provides the multiplier to scale neutral IC coefficients. The legend colours are consistent throughout the atomic plots, and in this case the data connected with a green line is neutral atom data and the yellow line data is ionised.

4.1.2 Nuclear Level Data - Evaluated Nuclear Structure Data Files (ENSDF)

This raw database is written in the archaic ‘punch-card’ style format of 80 character card entries, which can be parsed by specifying which characters correspond to a certain variable, listed in the manual [53]. Often the number of observables for a nuclear parameter cannot fit on a single 80 character card and so each card is followed by one or more ‘continuation cards’, in which the data is not parsed, and so one must write text based pattern recognition code using tools such as ‘RegEx’ [54] to extract the data. All aspects of this ENSDF reading have been extremely challenging and time consuming, and it is only very recently from ENSDF that .csv files of the levels and gamma ray cards have become available, although still one can only download these .csv files for a single nuclide at a time. Although the ENSDF data presentation and interactivity is been updated at Brookhaven, it is expected this work has allowed a global analysis ahead of the curve, by extracting

the B-values from the raw database numerically, an immense task that is not yet known to have commenced anywhere else.

Both the spin and parity in the raw database can be highly uncertain. In our analysis tentative assignments such as $J_{\pi}=[3+]$ are included (and their character database inputs cleaned with ReGex) but multiple assignments (such as $J_{\pi}=(1+, 2+, 3+)$) are discarded. Half-life's are read as character streams such as "2NS" and then converted to numeric values via RegEx, which would become 2×10^{-9} s.

This task has taken $\sim 10^5$ clicks and thousands of lines of wrangling code. Although a laborious and highly time-consuming part of the analysis and establishment of the NEEC framework, having all the the ENSDF data at ones fingertips proves to be highly fruitful.

We present data read from the level database in figure 4.4. Regions of rotational nuclear structure are indicated by the ratio of the first 4^+ to the first 2^+ excitation energies, which for a rigid rotor should be $\approx \frac{10}{3}$ [10]. This shows we have wrangled the level data from the raw ENSDF. ¹.

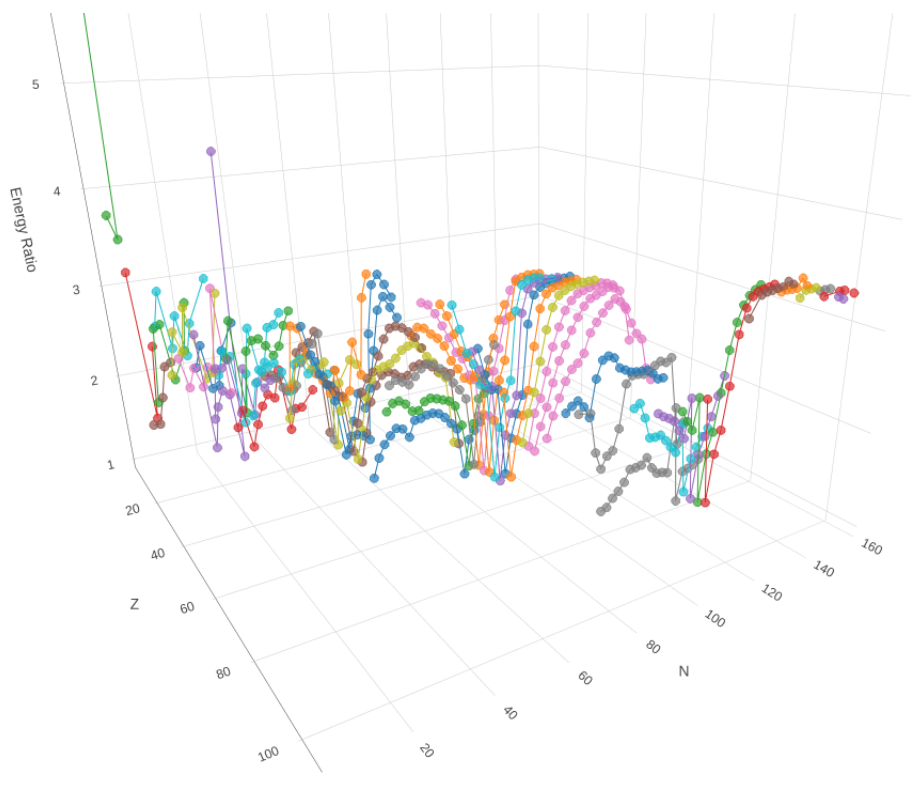


FIGURE 4.4: Ratio of the first 4^+ to the first 2^+ excitation energies of even-even nuclides from the raw ENSDF database

¹Please note: plotly is used as plotting tool in this chapter, although interactive, the 3D scatter plots do not yet allow LaTeX rendering so a snapshot has been taken, decreasing the resolution

Shown in figure 4.5 are all of the IC rates for known B-value gamma rays, calculated using equations 1.2 and 1.24, and the known B-values read from the ENSDF database. One cannot get more than these rates in a NEEC environment due to the principle of detailed balance, and conditions where the NEEC rates are this large are expected to be entirely astrophysical.

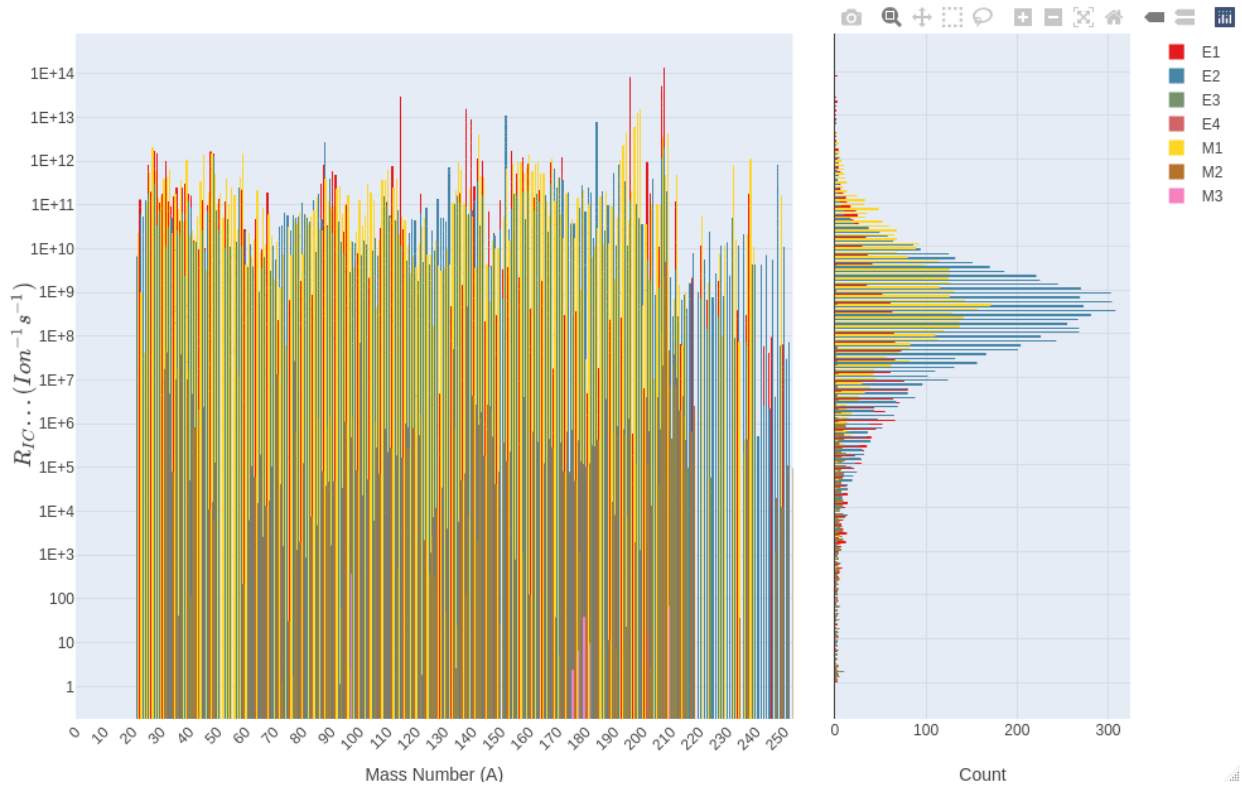


FIGURE 4.5: All of the Internal Conversion Rates $R_{IC} = A_{IC}$ (per atom per second) with negligible rates discounted, using all ENSDF gamma ray data with known matrix elements and the BrIcc calculation tool. Left: All rates plotted across mass number. Right: data from the left projected onto an aligned histogram in R_{IC} . There are 17,000 nuclear transitions in this dataset, with there being of course no restriction on the resultant state of the electron after IC.

4.1.3 Nuclear Gamma Ray Data - (ENSDF)



FIGURE 4.6: All of the radiative transition rates $R_{radiative} = A_r$ (per atom per second) with negligible rates discounted, using all ENSDF gamma ray data with known matrix elements. Left: All rates plotted across mass number. Right: data from the left projected onto an aligned histogram in A_r . There are $\sim 17,000$ nuclear transitions in this dataset, with there being of course no restriction on the resultant state after photon emission

Also available on ENSDF are the Gamma ray cards which contain $\sim 700,000$ gamma ray observations with $\sim 17,000$ reduced transition probabilities. These are plotted in figure 4.7, with the most common multipolarities shown on log-log plots in figure 4.8, with the radiative decay rates for all known B-values plotted in 4.6.

For candidate NEEC transitions in which the nuclear matrix element is unknown, we can use this matrix element database, filtered by multipolarity, to make an intelligent guess of the the B-value. Since the database contains a large number of transitions, we can see a distribution for each of the strongest transitions in figure 4.8. One would read off an appropriate value according to the energy of the transition, and filtering by similar mass numbers, to make a good estimate of a B-value if this is not known for a transition.

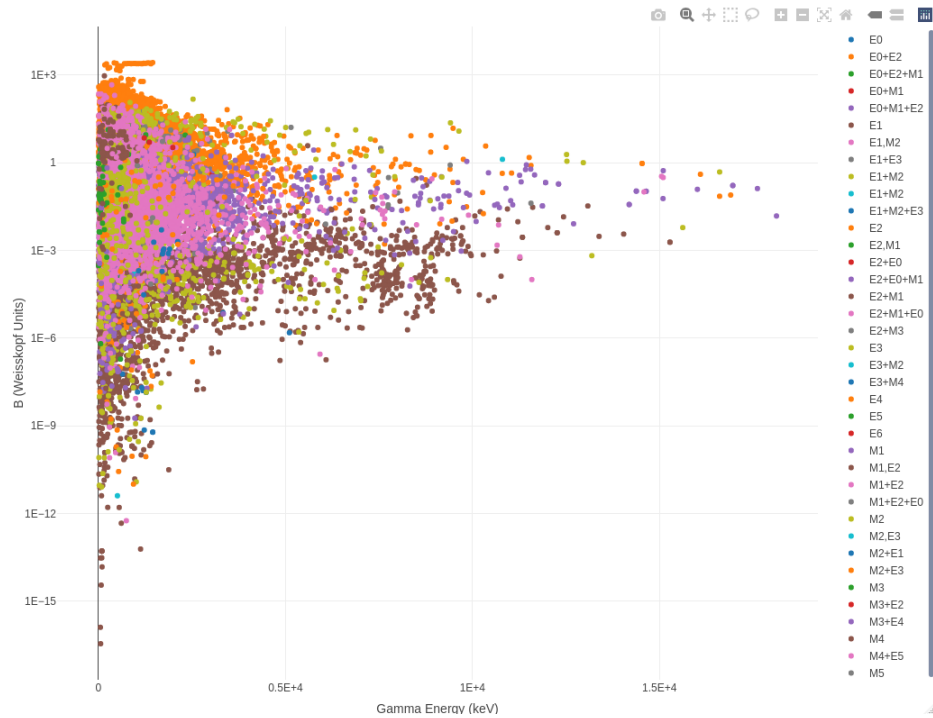


FIGURE 4.7: Gamma ray data produced by reading ENSDF Gamma continuation cards. B is the reduced transition probabilities for a gamma ray transition. These values are used in our analysis according to equation 1.23

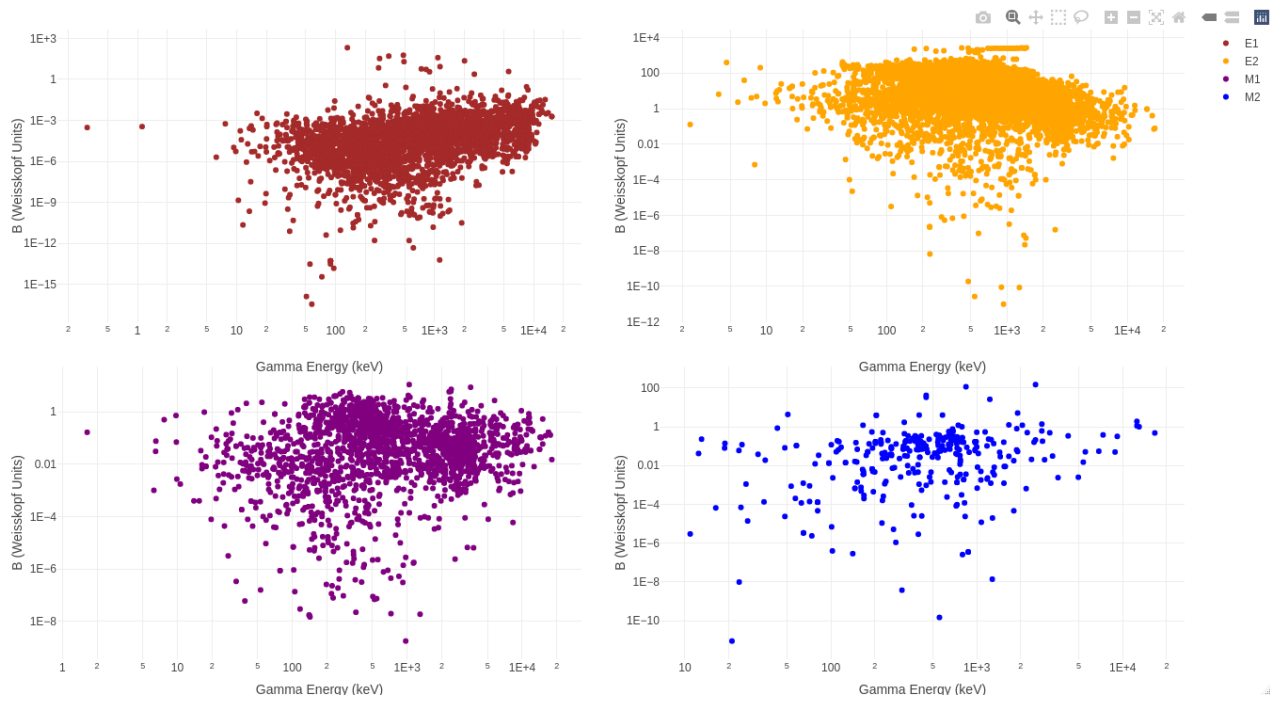


FIGURE 4.8: B-values for the most common multiplicities

4.1.4 Isomer Data - Atlas of Nuclear Isomers

As mentioned in chapter 1, the atlas of nuclear isomers is used as a database for isomeric states, as it is collated from both NUBASE, ENSDF and literature [34].

Isomer excitation energies and lifetimes are summarised in previous works [34][30] and available as a compilation known as the "Atlas of Nuclear Isomers" in [34], and again we present a collation of this data that we have wrangled in figure 4.9². Since often these isomers are not yet presented in the ENSDF database, one would have to make an intelligent guess of the nuclear matrix element, using the gamma database tool mentioned.

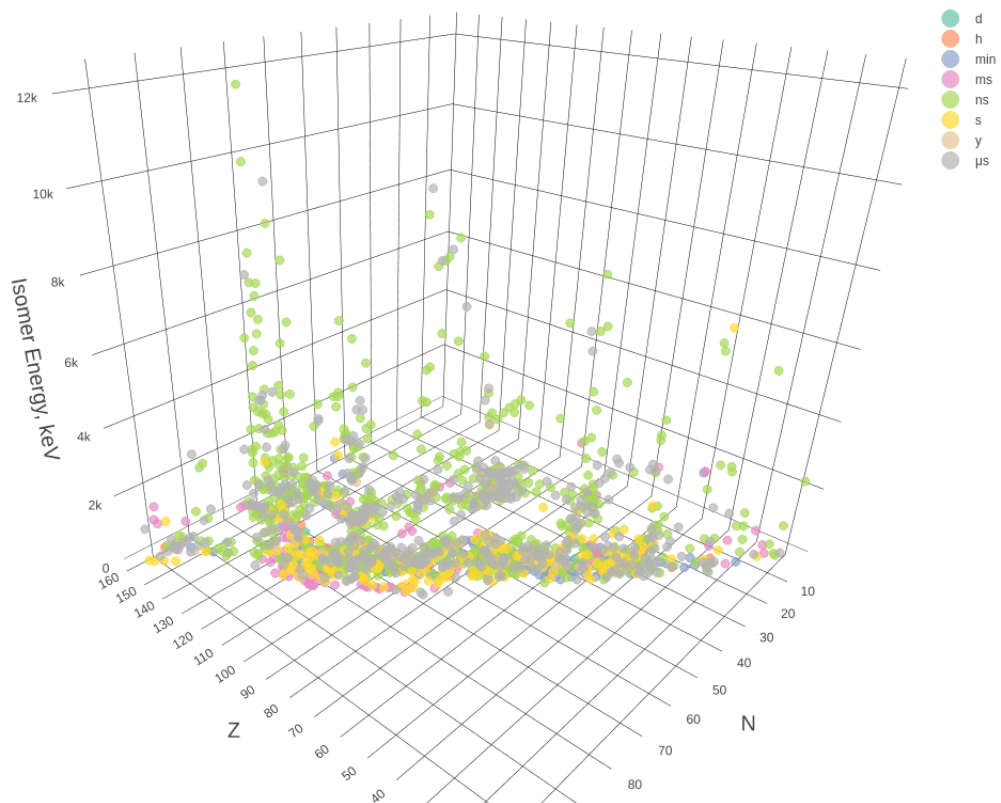


FIGURE 4.9: Energies and rough half-life of all isomers collated from the atlas of nuclear isomers [34]

²in this case taking around 10^3 clicks to extract data from PDF tables

4.2

General Search Algorithm with Energetic Constraints

In order to observe NEEC, we have adopted a systematic approach, in which we test all nuclides under all conditions, down selecting by applying experimental constraints. *This is powerful as now that NEEC has been observed in early 2018 [22], for it to be useful, we have to be able to ‘fine-tune’ our choice of candidate system and know that it is the best available for a certain purpose. E_e here is known as the experimentally accessible energy.*

The general set of conditions which can be accessed as in chapter 3, expressed more computationally is as follows:

- (i) Search through all nuclear transitions (Q) known to exist, which satisfy $Q = |V_i| + E_e$ applying a maximal constraint on E_e , given the best possible experimental apparatus, i.e., we will have an all-inclusive list of possible Q and $|V_i|$ which could match for an experiment; which are constrained accordingly depending on the facility. $F(E_e)$, must then be controlled via a user interface so that the continuum electron energy distribution Δ overlaps the resonance spectrum as much as possible.
- (ii) Down select to maximize the detailed balance resonance strength and the macroscopic cross section, so that the resonance fraction is non negligible; we roughly maximize the fraction $F(E_{eff})$.
- (iii) Compute resonance strength and typical NEEC probability that would require a 1 week long continuous experiment. So we are highly sensitive to the beam intensity or the laser pulse repetition rate, depending on the facility available.
- (iv) Down select depending on a detectable (or useful) NEEC signature relaxation. This goal has not yet been achieved in the NEEC database and should a priority in extending this work.

4.2.1 Map of the Database Structure

The relational database structure of the NEEC database is shown in figure 4.10. Each database source (represented as a cylinder) was first wrangled using modern relational database techniques and the R programming language. Once energetically viable candidates are ascertained, the BrIcc tool is used to calculate the resonance strength, along with the B-value used to calculate A_r . FLYCHK is used to then calculate the n-LTE charge state distributions and each scaled resonance channel is stored in the database. The database assumes Weisskopf estimates for an unknown B-value, but one can adjust this via the user interface to the database once one has made a more intelligent guess of the B-value.

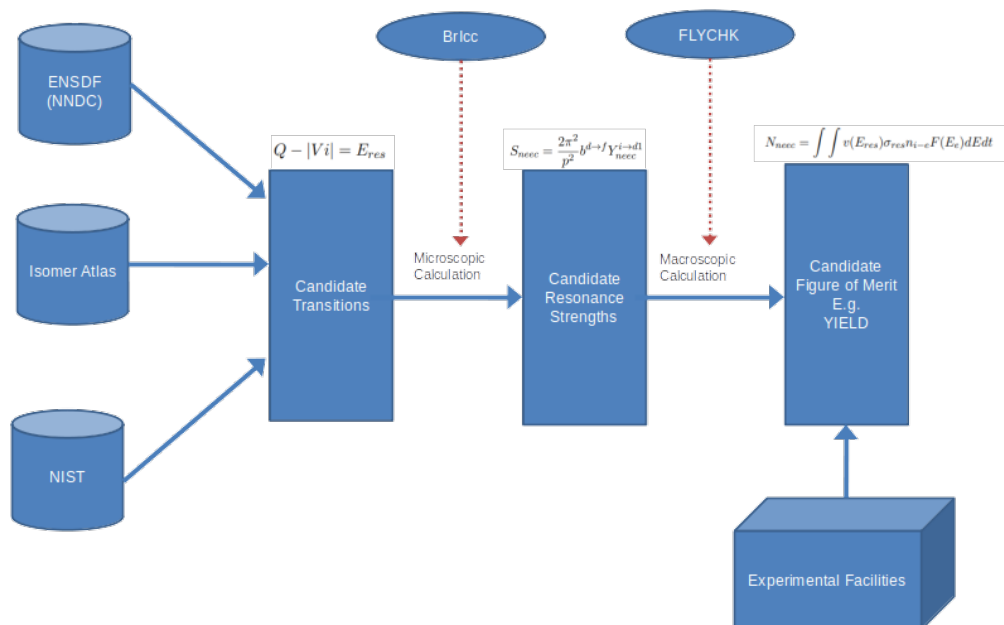


FIGURE 4.10: Structure of the NEEC Database, with the dimensionality implicit to the size of the analysis

4.3

High Powered Laser-Plasma

We present in this section a candidate search for the best NEEC plasma candidate systems. All rates in this section are expressed in $\text{ion}^{-1}\text{s}^{-1}$, as this eliminates a variable in what is an extremely high dimensional parameter space. One should order these candidates by the largest rates per ion, and only then an analysis of the enrichment of the nuclide in the solid will inform one of the final best approach. The results displayed are encouraging, but one might expect these rates to be larger, given how large the IC rate can be, and again one must bare in mind the difficulty in detecting a depletion signature in a plasma.

4.3.1 The Hottest-Densest Terrestrial Plasmas

AX	E_i	E_f	J_i	J_f	Type	T_i	T_f	Q	E_c	B	δ	α_{tot}	S_{tot}	R_{NEEC}
239PU	0	7.861	1/2+	3/2+	M1	24110 Y	36 PS	7.861	6.14	0.22	0.055	2550	39	7730000
208TL	0	39.858	5+	4+	M1	3.053 M	6.5 PS	39.858	35.4	2.1	0	23.3	29.2	2310000
249BK	0	41.805	7/2+	9/2+	M1	330 D	9 PS	41.805	35.7	0.26	0.13	98.4	26.9	2120000
244CM	0	42.957	0+	2+	E2	18.11 Y	97 PS	42.957	37	419	0	1051	12.3	952000
246CM	0	42.852	0+	2+	E2	4706 Y	123 PS	42.852	36.9	327	0	1064	9.74	754000
248CM	0	43.4	0+	2+	E2	3.48E+5 Y	122.5 PS	43.4	37.4	324	0	1000	9.62	739000
212BI	0	115.183	1-	2-	M1	60.55 M	8 PS	115.183	108	0.23	0	6.8	13.7	568000
240PU	0	42.824	0+	2+	E2	6561 Y	167 PS	42.824	37.1	287	0	905	6.9	533000
242PU	0	44.54	0+	2+	E2	3.75E+5 Y	158 PS	44.54	38.8	300	0	748	7	528000
237NP	0	33.19629	5/2+	7/2+	M1	2.144E+6 Y	54 PS	33.19629	28.2	0.06	0.13	129.2	5.58	500000
237NP	0	33.25	5/2+	7/2+	M1	2.144E+6 Y	54 PS	33.25	28.2	0.06	0.13	128.6	5.57	499000
238PU	0	44.065	0+	2+	E2	87.7 Y	175 PS	44.065	38.3	285	0	788	6.58	499000
238U	0	44.916	0+	2+	E2	4.468E9 Y	206 PS	44.916	39.4	281	0	610	5.4	404000
236U	0	45.244	0+	2+	E2	2.342E7 Y	234 PS	45.244	39.7	250	0	589	4.72	351000
234U	0	43.4981	0+	2+	E2	2.455E+5 Y	0.252 NS	43.4981	37.9	236	0	713	4.59	350000

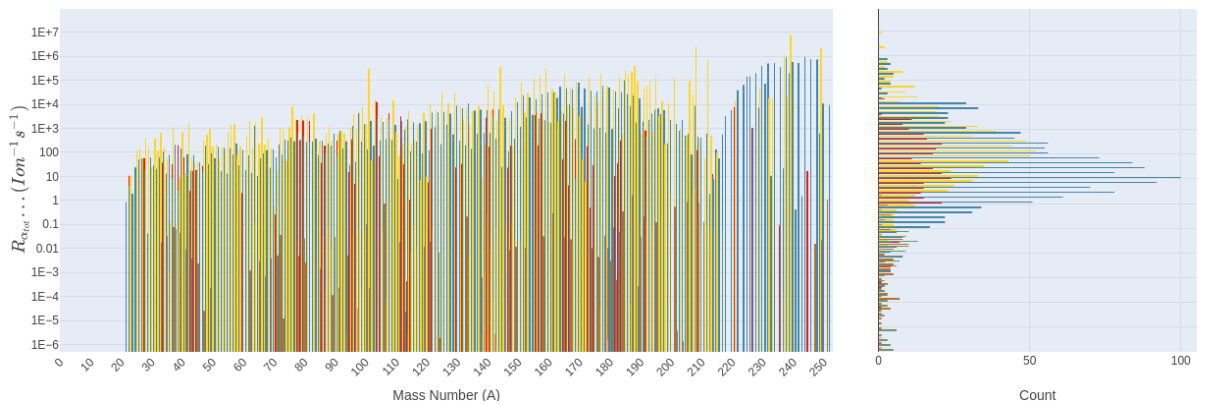


FIGURE 4.11: All the NEEC plasma rates assuming one can tune to $T_e = E_{eff}$. This is also assuming a maximal terrestrial electron density of $10^{24} \text{e}^{-}\text{cm}^{-3}$. All energies are in keV, B in w.u., S in beV, and rate in s^{-1}

A summary of the NEEC rates one can achieve terrestrially is displayed in figure 4.11. The results are slightly worrying, for even the highest NEEC rates of $10^7 \text{ion}^{-1}\text{s}^{-1}$,

one must for these rates create a total plasma lifetime of 1ns over an experiment and sustain 10^{11} candidate ions to get 10^5 NEEC events (with an optimistic detectable fraction of 10^{-3} and an overestimate factor due to using $S(\alpha_{tot})$ of 10). This highlights a possible need to inject electrons into the plasma and increase the electron density by several orders of magnitude. In getting as close as possible to these rates, one must maximise the macroscopic factor by choosing the best laser facility. The main goal of the NEEC tool is to assist with this task.

The modal IC rate shown in figure 4.5 is $\sim 10^9 \text{atom}^{-1} \text{s}^{-1}$. This is compared to a modal NEEC rate of $\sim 10^1 \text{ion}^{-1} \text{s}^{-1}$ expressed in figure 4.11 for terrestrial densities of $10^{24} \text{e}^- \text{cm}^{-3}$ and tuned electron temperatures. Evidently one would require electron densities $\gg 10^{32} \text{e}^- \text{cm}^{-3}$ in order for NEEC to be at an equilibrium with IC and for the Boltzmann relation to be challenged in equation 1.28. This would be an astrophysical plasma condition where ions are fully ionised and degeneracy factor in equation 3.56 $\ll 1$.

As defined, we can already evaluate an optimal figure of merit for the highest irradiance laser facilities using the macroscopic factor (time integrated NEEC Flux Φ), which is displayed in figure 4.12. One should choose the facilities with the highest macroscopic factor so long as the temperature is above a threshold to be fully ionised. Noticeably, the macroscopic factor varies proportionally with the repetition rate of the laser, so we can conclude that if the electron temperature is tuned to the effective impact energy of the resonance spectrum, and the plasma is fully ionised, then one must maximise the plasma lifetime available within the experimental run, by choosing the facility with the highest repetition rate and hot electron temperature closest to E_{eff} . Figure 4.12 shows us that it is not necessarily best to choose the highest irradiance facility. One can define a 3 or 4 dimensional surface to properly optimise the macroscopic factor, but it is beyond the scope of this project; although the data infrastructure to achieve this goal has nevertheless been provided with the NEEC tool. Φ should be maximised at a specific facility by tuning the electron temperature to be as close to the effective energy as possible.

Using FLYCHK n-LTE calculations, one can see the temperature required to fully ionise a plasma accross the elements. "Fully ionised" considered as having an average charge state of $(Z-0.5)^+$ as in a plasma the average charge state only tends towards Z: there will always be a small fraction of ions in a charge state $Z+1$. The $T_e^{q=Z+0.5}$ plot is shown in figure 4.13. Since we only have CSD data for $T_e < 100 \text{keV}$, we make an empirical

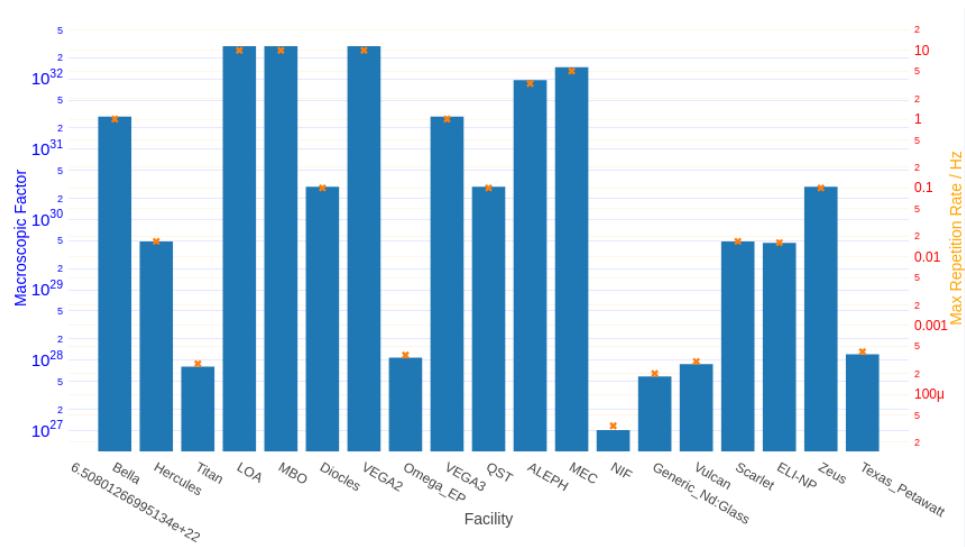


FIGURE 4.12: Macroscopic factor (left axis) and Maximum Repetition Rate (Right axis) for the high power laser facilities considered. The facilities are ordered from left to right in increasing irradiance (and thus electron temperature)

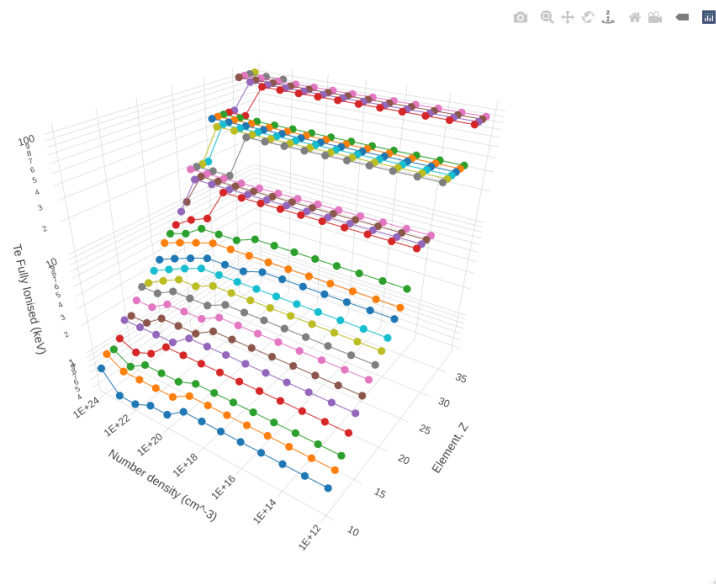


FIGURE 4.13: Temperature required to achieve a fully ionised plasma at n-LTE (average charge state data from FLYCHK [44]). A step like structure for higher temperatures is due to a lack of resolution in temperature values. More temperatures need to be calculated, but trends can still be seen. Colours are to help distinguish the different elements.

approximation that the plasma temperature must be above the total electronic energy of the atom (i.e. the energy required to remove every electron sequentially). This is shown to be a reasonable approximation in figure 4.15 whereas an underestimate would use the last electron binding energy, shown in figure 4.14

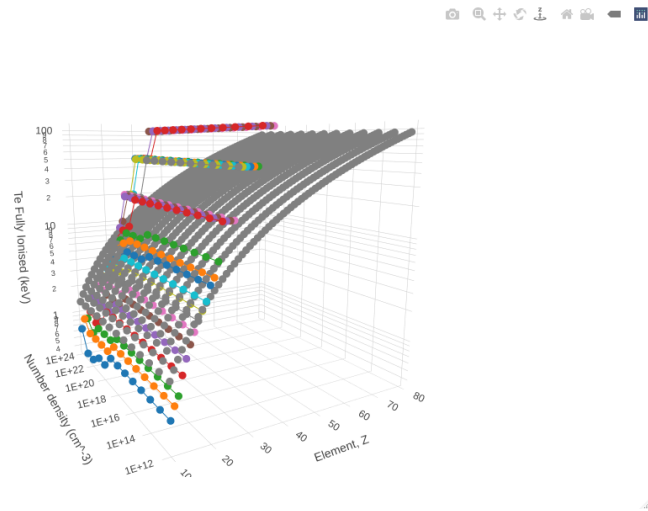


FIGURE 4.14: Fully ionised temperatures compared to the ionisation energy of the last remaining electron on the atom in the plasma

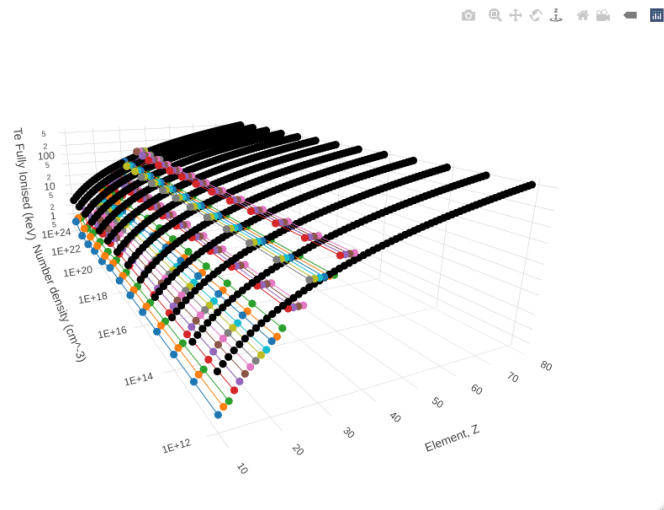


FIGURE 4.15: Fully ionised temperatures compared to the total electronic energy (sum of all ionisation energies)

The top 30 isomeric NEEC terrestrial plasma rates with known B-value are presented in table 4.1. One should adjust the electron density via the NEEC tool for these specific candidates and evaluate their astrophysical impact with the produced upper limit NEEC rate; this is proposed as an immediate extension to this work.

TABLE 4.1: TOP 30 viable calculable isomeric NEEC transitions for all plasmas assuming T_e is achievable by the laser. All energies are in keV, B in w.u., S in beV, and rate (R_{NEEC}) in $\text{ion}^{-1}\text{s}^{-1}$

Nuclide	E_i	E_f	J_i	J_f	Type	T_i	T_f	Q	E_{eff}	$T_e^{q \sim Z}$	B	δ	α_{tot}	S_{tot}	R_{NEEC}
101RH	157.32	181.78	9/2+	7/2+	M1	4.34(1) d	1.91 NS	24.46	22.7	130	0.788	0.02	20.1	2.84	285500
177TA	487.62	497.42	1/2+	3/2+	M1	26(3) ns	0.44 NS	9.8	8.82	424.6	0.07	0	157.8	1.07	175800
237NP	59.54092	102.959	5/2-	7/2-	M1	67.2(7) ns	80 PS	43.42	37.8	783	0.017	0.41	58.6	1.17	89400
161ER	189.42	217.34	9/2+	7/2+	M1	84(10) ns	0.55 NS	27.92	24.5	355.9	0.053	0.1	19.3	0.289	27960
151SM	4.821	168.402	3/2-	5/2-	M1	35(1) ns	39 PS	163.6	159	283.5	0.05	-0.15	0.421	0.289	9307
163YB	124	167.6	9/2+	13/2+	E2	~ 10 ns	2.37 NS	43.6	41.9	382.5	240	0	116.8	0.128	9267
103RH	39.753	93.036	7/2+	9/2+	M1	56.114(9) min	1.11 NS	53.28	50.4	130	0.043	0	2.08	0.111	7222
133CE	37.2	207.4	9/2-	11/2-	M1	5.326(11) h	52.7 PS	170.2	166	240.8	0.065	-0.16	0.266	0.187	5861
114SN	3087.37	3190.39	7-	8-	M1	733(14) ns	0.35 NS	103	99.7	167.9	0.06	0	0.517	0.122	5305
167ER	207.801	264.874	1/2-	3/2-	M1	2.269(6) s	1.47 NS	57.07	53.7	355.9	0.011	0.36	2.35	0.0695	4362
140CS	13.931	64.756	2-	3-	M1	471(51) ns	3.7 NS	50.82	47	211.6	0.0062	0	6.36	0.0503	3408
161DY	25.65136	103.0623	5/2-	7/2-	M1	29.1(3) ns	0.60 NS	77.41	72.4	330.6	0.0037	-1.05	5	0.0582	3071
98MO	734.75	787.384	0+	2+	E2	21.8(9) ns	3.47 PS	52.63	50	110.1	287	0	12.05	0.0464	3031
165DY	108.1552	158.5885	1/2-	3/2-	M1	1.257(6) min	1.8 NS	50.43	47.2	330.6	0.005	0.39	2.79	0.0291	1965
66GA	43.812	66.139	1+	2+	M1	18.0(9) ns	23.0 NS	22.33	20.6	52.86	0.0122	0.079	4.98	0.0174	1848
161DY	25.65136	74.56668	5/2-	3/2-	M1	29.1(3) ns	3.14 NS	48.92	45.7	330.6	0.0115	-0.056	3.05	0.023	1583
167OS	435.1	798	13/2+	17/2+	E2	672(7) ns	13.9 PS	362.9	357	469.4	112	0	0.0528	0.0861	1546
82BR	45.9492	75.0621	2-	1+	E1	6.13(5) min	7.2 NS	29.11	27.1	70.86	0.00049	0	3.08	0.0158	1448
132SN	4715.91	4919	6+	7+	M1	20.1(5) ns	62.0 PS	203.1	200	167.9	0.0369	0	0.0797	0.0413	1138
95TC	38.91	646.55	1/2-	3/2-	M1	61(2) d	0.44 PS	607.6	605	116.5	0.22	0	0.00268	0.0917	1067
77KR	66.5	245.32	3/2-	5/2-	M1	118(12) ns	37 PS	178.8	177	75.87	0.097	-0.09	0.0271	0.0353	1058
196AU	84.656	232.47	5+	7+	E2	8.1(2) s	1.65 NS	147.8	141	517.2	34	0	1.107	0.0245	854.5
151SM	91.532	167.75	9/2+	5/2+	E2	78(1) ns	0.38 NS	76.22	71.6	283.5	170	0	6.4	0.0154	819.4
187TL	334	996.34	9/2-	13/2-	E2	15.60(12) s	2.0 PS	662.3	656	550.8	29	0	0.01478	0.0719	781.1
79SR	177.3	329.81	5/2+	7/2+	M1	20(1) ns	107 PS	152.5	150	86.44	0.052	-0.22	0.0515	0.0232	775.7
194AU	107.4	244.6	5+	7+	E2	600(8) ms	2.6 NS	137.2	131	517.2	27	0	1.468	0.0191	702.1
152EU	77.2593	141.8259	3-	4-	M1	38(4) ns	2.5 NS	64.57	63.2	294.8	0.00085	0	6.52	0.012	685.7
109PD	113.4	291.4339	1/2+	3/2+	M1	380(50) ns	136.5 PS	178	175	137.1	0.0143	0	0.0776	0.0218	657.4
193IR	80.239	299.396	11/2-	7/2-	E2	10.53(4) d	0.19 NS	219.2	213	485	71	0	0.254	0.0249	655.6
194AU	107.4	278.2	5+	6+	M1	600(8) ms	1.1 NS	170.8	164	517.2	0.001	-0.6	1.582	0.0205	645.7

4.3.2 Cooler Plasma Results

When we produce plasma's that have an electron temperature $\sim |V_i|$, the macroscopic factor becomes highly convoluted with the microscopic resonance strength, since the plasma will have a charge state distribution. Candidate examples of the NEEC rate for temperatures and densities for which there is FLYCHK data, are shown in figures 4.16, 4.17 and 4.18. We see there is a typical shift in the optimum to lower temperature, as the electron densities are increased, this is since the the average charge state increases, exposing more resonances and thus shifting the optimum towards inner subshell capture channels. We see that in general the effective energy, E_{eff} (shown as a black line), is a good predictor of the optimum temperature.

In the case where CSD data is not available we must use the effective resonance strength $S(\alpha_{tot}, E_{eff})$ calculated in equation 3.41. One can estimate a LTE charge state distribution using the SAHA equation [38] or by running FLYCHK to higher temperatures - this is proposed as an extension to this work, yet, already the optimal temperature can be found to within 1keV up to a temperature of 10keV and to within ≈ 25 keV for temperatures between 10keV and 100keV with the CSD data provided. Above 100keV as it stands the calculation uses $S(\alpha_{tot}, E_{eff})$, i.e. the plasma is assumed to be fully ionised when this may not be the case, especially for $T_e < E_{tot}$, which is our approximate fully ionised temperature. More CSD data should be generated above 100keV and at more regular temperature intervals, using the appropriate type of equilibrium.

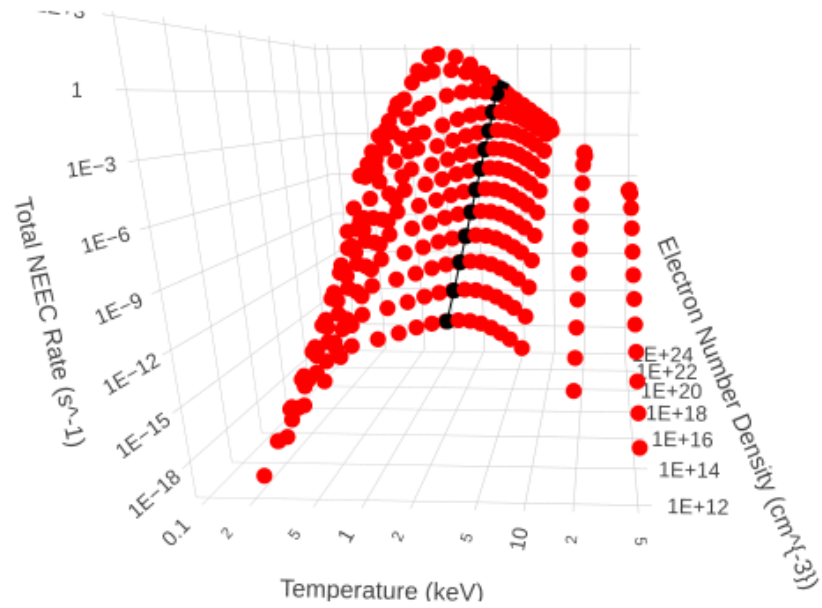


FIGURE 4.16: NEEC Rate for in ^{93m}Mo within the FLYCHK grid of temperatures and densities. Optimum temperature reproduces well the data from [40] and can be applied to all NEEC'able candidates in the database

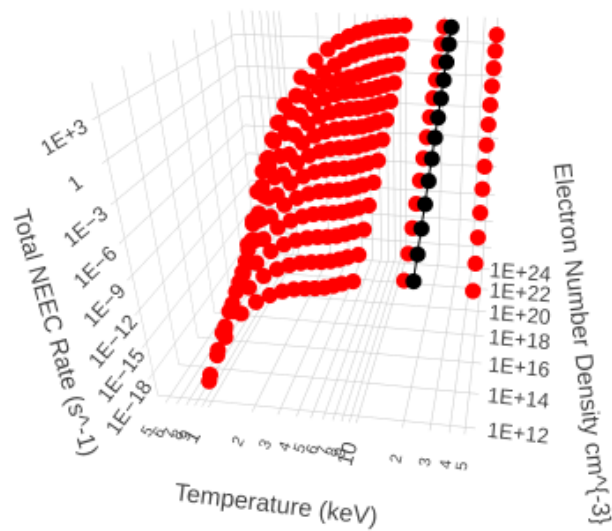


FIGURE 4.17: NEEC rates per ion calculated using the NEEC tool for the 24.46keV M1 transition from the 157keV isomer of ^{101}Rh . The effective electron energy is plotted in black

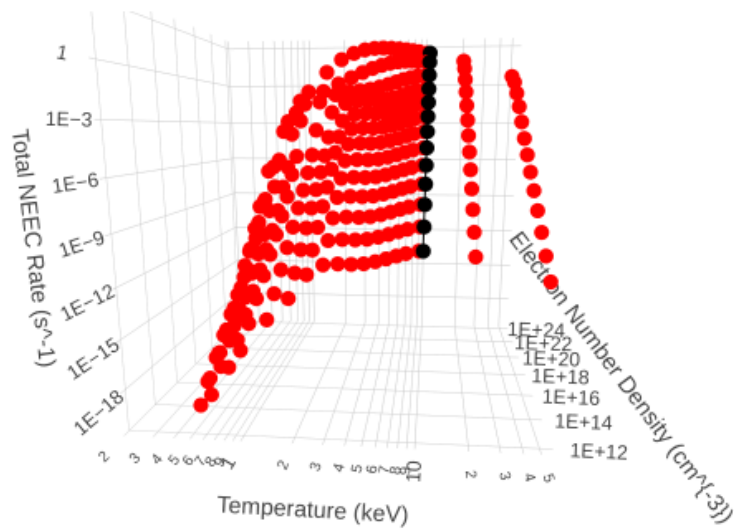


FIGURE 4.18: NEEC rates per ion calculated using the NEEC tool for the 12.81keV E2 transition from the 69.6keV isomer of ^{130}I . The effective electron energy is plotted in black

4.4

NEEC Companion Tool

The NEEC companion tool, developed over several years, allows an experimenter (or theorist) to change the electron temperature and density³ creating a n-LTE plasma which entails a charge state distribution. The tool is available via the link <https://shiny.york.ac.uk/nec>⁴. The password, if required, is available to the user on request to the author.

The NEEC tool is split into 3 Tabs.

- "Find Transition" Tab, shown in figure 4.19. This allows the user to search through all possible nuclear transitions with upper limit plasma and EBIT rates, calculated using $S(\alpha_{tot}, E_{eff})$. The user can search between a certain range of impact energies to see what kind of NEEC candidates are relevant in a certain environment. Once the user has selected a candidate transition of interest, they should move onto the third tab. If the "Weisskopf Estimate" variable is TRUE then the user must first go

³or a laser facility parameter

⁴The page can take a few minutes to load in your browser

to tab 2 to make a best guess of the nuclear matrix element. The user may also filter the results in tab 1 for isomeric only or known B-value only.

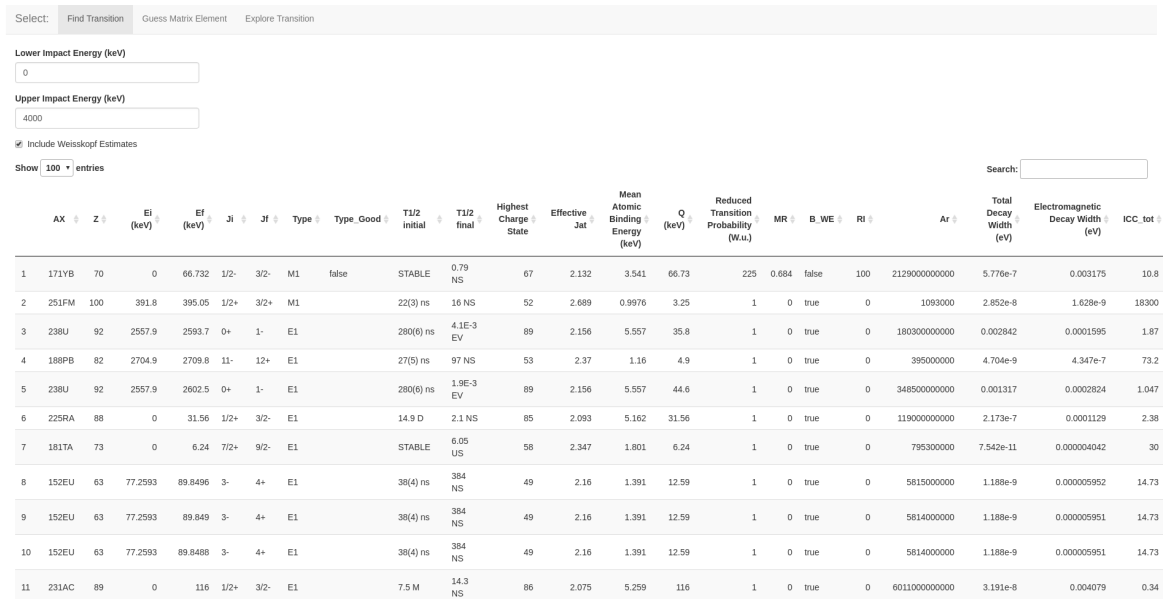


FIGURE 4.19: "Find Transition" Tab of the NEEC tool

- "Guess Matrix Element" Tab, shown in figure 4.20. When the matrix element is not known for the nuclear transition one can make an intelligent guess of the matrix element by filtering the simplified ENSDF gamma database. Double clicking on a certain multipolarity (creating a subplot like in figure 4.8) and filtering by mass will inform the user of an intelligent guess for the B-Value input for the "Explore Nuclide" tab.

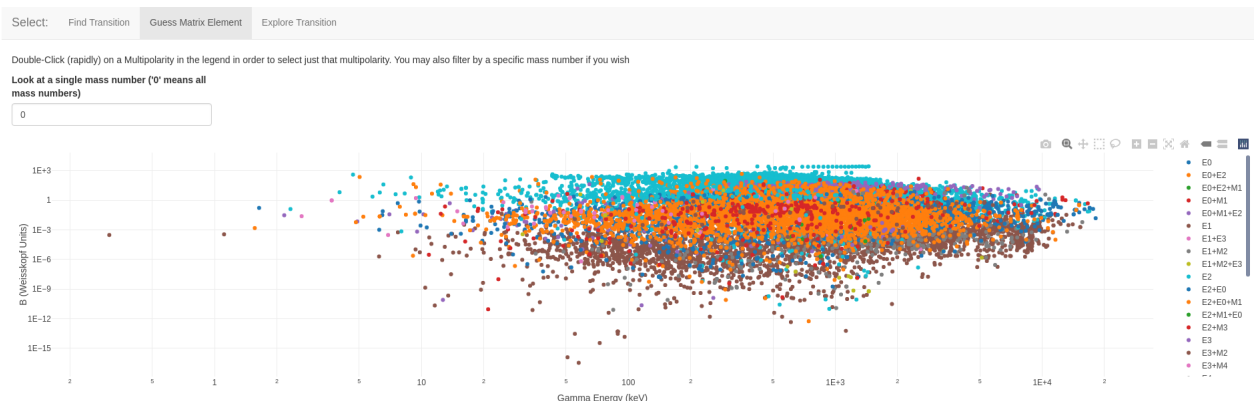


FIGURE 4.20: "Guess Matrix Element" Tab of the NEEC tool

- "Explore Transition" Tab, shown in figure 4.21. The user will then setup the parameters in the boxes to match their desired candidate and conditions (Either "Astrophysical" or "Facility"). Assuming the effective impact energy is less than 100keV, then CSD data can be generated and the optimal temperature and density can be calculated by pressing the "Optimise Temperature" button at the bottom of the left pane. Once the Rate data is calculated (this can take up to 20min), the user may download this data to complete their own astrophysical NEEC rate study with the candidate

The NEEC tool can be used as both an astrophysical tool to evaluate the impact of NEEC in a high electron density environment, as a candidate search tool for plasma and EBIT candidates, and as an optimisation tool for a proposed plasma experiment. The tool will increase in accuracy as more CSD data is added for higher electron temperatures. Also, using the Gamma B-value search and input aspect one can predict NEEC rates that are worth calculating in more detail in a model dependant fashion.

Select:
Find Transition
Guess Matrix Element
Explore Transition

Figure out what it is you need to calculate, set up the correct parameters in the boxes and sliders. Then click GO. Once you have generated the data with GO, you can then click OPTIMIZE TEMPERATURE. If you have pressed GO or OPTIMIZE TEMPERATURE once then you should refresh the app, before choosing a new candidate / change parameters.

n_e , T_e , τ and repetition rate are defined by the facility unless 'Astrophysical' input selected; then the user will input these

Note: can take several minutes to calculate NEEC rates and produce plots. If running T_e optimisation will take ~15m, longer for high Z. Once you've clicked OPTIMIZE TEMPERATURE just leave it and wait for the loading bar to fill. Have a cup of coffee.

If you want to have a look for a good B value do that first. B values are not plotted if the OPTIMIZE TEMPERATURE is running.

Input type?

Astrophysical
 Facility

Go

Which nuclide (element in caps)

130I

Initial Nuclear Level:

Isomeric

Select Nuclear Transition

12.8095

Enter B value

12

Output Type:

Rate

Enter Electron Temperature (keV)

10

Enter Plasma Number density (e-'s cm⁻³)

1e+24

Laser Facility:

ELI-NP

Plasma Lifetime (ps)

0.1 100 1,000

Length of Experiment (Weeks):

0.1 1 5

8000

7000

6000

5000

4000

3000

2000

Isomer Energy / keV

133(7) ns

8.84(6) min

The top plot shows NEEC Resonance Strength, S (beV) on a log scale from 1E-7 to 0.1. The middle plot shows NEEC Rate / s^-1 on a log scale from 1E-42 to 1, with a total rate of 289.08. The bottom plot shows Charge Fraction vs Number of Electrons on Ion - Pre Capture, with a peak at approximately 5 electrons.

The 3D plot shows Total NEEC Rate (s^-1) on the vertical axis (log scale from 1E+12 to 1E+3), Electron Number Density (cm^-3) on the horizontal axis (log scale from 1E+12 to 1E+24), and Temperature (keV) on the depth axis (log scale from 1E+12 to 1E+20). The data points form a curved surface.

Error: could not find function "wap_f2"

FIGURE 4.21: "Explore Transition" Tab of the NEEC tool. Sometime's Shiny will display an error message at the bottom, which can safely be ignored. The instructions for getting results from this tab should be followed carefully otherwise the tool may crash.

4.5

The Stockholm Electron-Beam Ion-Trap - Results

There are 311,655 possible species for this setup, which are spread over 6759 energetically viable nuclear transitions. The number of transitions which can be calculated due to known reduced transition probabilities is 1054, with the most promising rates expressed in figure 4.22.

These rates are calculated assuming the species can be fully ionised in the EBIT, with upper limit densities at the Stockholm super EBIT [55], $n_e = 1 \times 10^{11} \text{e}^- \text{cm}^{-3}$ and $n_{ion} = 1 \times 10^9 \text{ions cm}^{-3}$.

The candidates in table 4.2 one should consider for nuclear battery applications and development. One should select from this list an initial energy and long enough isomeric lifetime to last as long as one needs to transport and store the battery, and convert to electro-chemical energy on command via NEEC or a similar mechanism. The data in this table is presented alongside the upper limit NEEC plasma rate in the "find transition" tab of the NEEC tool.

The top 15 EBIT candidate species are presented in the tables of figure 4.22, as well as the distribution of the rates. It is notable that although there are much lower total rates in this scenario when compared to a plasma, one can run an EBIT constantly, and so one expects the yield to quickly outweigh that achievable in a plasma.

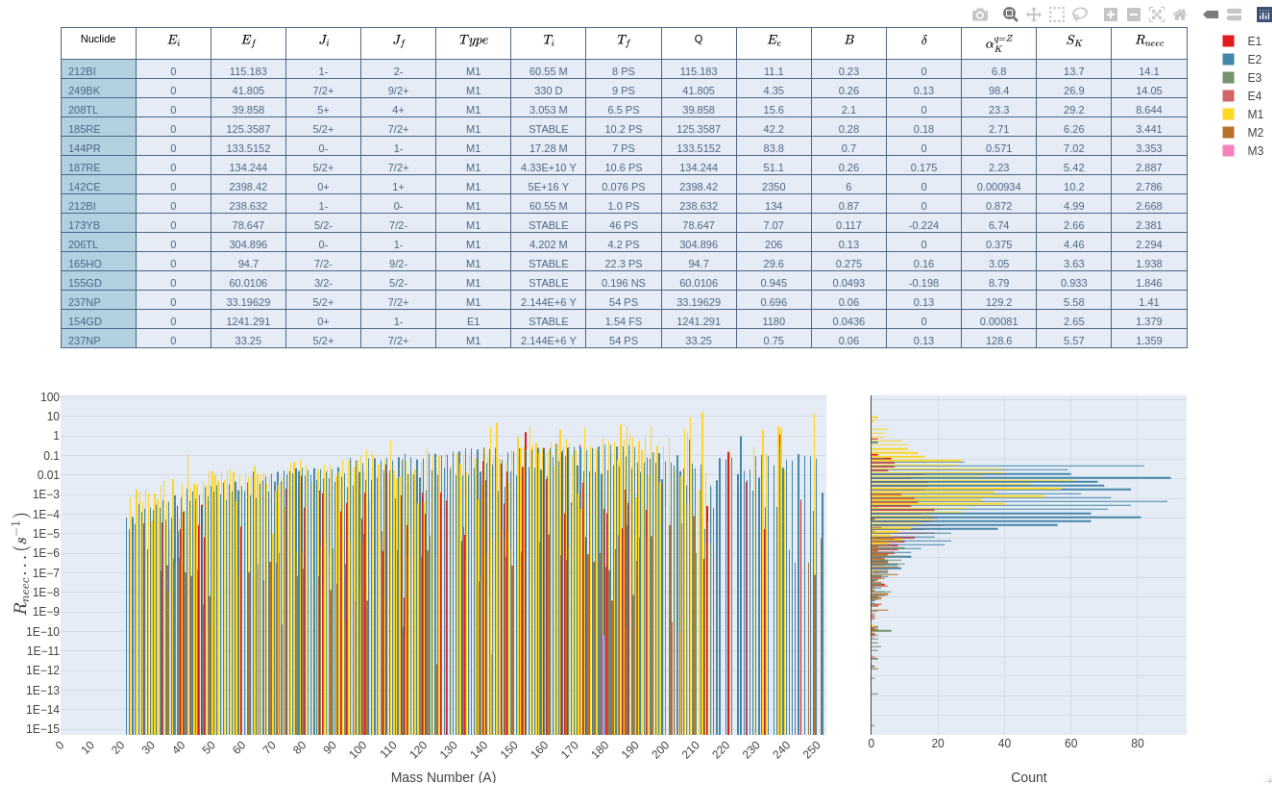


FIGURE 4.22: Viable calculable NEEC transitions from the nuclear ground state at the Stockholm EBIT. All energies are in keV, B in w.u., S in beV, and rate (R_{neec}) in s^{-1}

TABLE 4.2: Top 30 viable calculable isomeric NEEC transitions at the Stockholm Super-EBIT. Since these results are within the strongest single resonance channel, they have implications for nuclear battery possibilities. All energies are in keV, B in w.u., S in beV, and rate (R_{neec}) in s^{-1}

Nuclide	E_i	E_f	J_i	J_f	Type	T_i	T_f	Q	E_c	$ V_1 $	B	δ	$\alpha_K^{q=Z}$	S_p	R_{neec}
237NP	59.54092	102.959	5/2-	7/2-	M1	67.2(7) ns	80 PS	43.42	9.7	33.7	0.017	0.41	58.6	1.17	0.442
151SM	4.821	168.402	3/2-	5/2-	M1	35(1) ns	39 PS	163.6	108	55.2	0.05	-0.15	0.421	0.289	0.135
101RH	157.32	181.78	9/2+	7/2+	M1	4.34(1) d	1.91 NS	24.46	17.8	6.62	0.788	0.02	20.1	2.84	0.106
133CE	37.2	207.4	9/2-	11/2-	M1	5.326(11) h	52.7 PS	170.2	122	48	0.065	-0.16	0.266	0.187	0.092
161ER	189.42	217.34	9/2+	7/2+	M1	84(10) ns	0.55 NS	27.92	11.6	16.3	0.053	0.1	19.3	0.289	0.077
95TC	38.91	646.55	1/2-	3/2-	M1	61(2) d	0.44 PS	607.6	582	25.8	0.22	0	0.00268	0.0917	0.057
114SN	3087.37	3190.39	7-	8-	M1	733(14) ns	0.35 NS	103	67.8	35.2	0.06	0	0.517	0.122	0.054
103RH	39.753	93.036	7/2+	9/2+	M1	56.114(9) min	1.11 NS	53.28	25	28.3	0.043	0	2.08	0.111	0.044
161DY	25.65136	103.0623	5/2-	7/2-	M1	29.1(3) ns	0.60 NS	77.41	14.3	63.1	0.0037	-1.05	5	0.0582	0.037
167OS	435.1	798	13/2+	17/2+	E2	672(7) ns	13.9 PS	362.9	277	85.6	112	0	0.0528	0.0861	0.036
187TL	334	996.34	9/2-	13/2-	E2	15.60(12) s	2.0 PS	662.3	564	98.6	29	0	0.01478	0.0719	0.034
140CS	13.931	64.756	2-	3-	M1	471(51) ns	3.7 NS	50.82	7.91	42.9	0.0062	0	6.36	0.0503	0.033
132SN	4715.91	4919	6+	7+	M1	20.1(5) ns	62.0 PS	203.1	168	35.2	0.0369	0	0.0797	0.0413	0.021
167ER	207.801	264.874	1/2-	3/2-	M1	2.269(6) s	1.47 NS	57.07	40.8	16.3	0.011	0.36	2.35	0.0695	0.021
87SR	388.533	873.339	1/2-	3/2-	M1	2.815(12) h	1.7 PS	484.8	465	20	0.11	0.19	0.00282	0.0314	0.02
119SN	23.871	1089.44	3/2+	5/2+	M1	18.03(7) ns	0.21 PS	1066	1030	35.2	0.08	0.26	0.001355	0.0315	0.019
77KR	66.5	245.32	3/2-	5/2-	M1	118(12) ns	37 PS	178.8	161	17.9	0.097	-0.09	0.0271	0.0353	0.018
140SM	3652.8	4404.1	12+	14+	E2	15.2(21) ns	1.2 PS	751.3	696	55.2	45	0	0.00467	0.0288	0.015
98MO	734.75	787.384	0+	2+	E2	21.8(9) ns	3.47 PS	52.63	28.1	24.6	287	0	12.05	0.0464	0.014
85SR	238.79	1152.73	1/2-	3/2-	M1	67.63(4) min	0.13 PS	913.9	894	20	0.1	0	0.000679	0.019	0.013
79SR	177.3	329.81	5/2+	7/2+	M1	20(1) ns	107 PS	152.5	132	20	0.052	-0.22	0.0515	0.0232	0.012
113SN	738.4	1781.1	11/2-	9/2-	M1	86(2) ns	0.19 PS	1043	1010	35.2	0.08	-0.5	0.001422	0.0178	0.011
123CS	156.27	476.8	11/2-	15/2-	E2	1.64(12) s	40 PS	320.5	278	42.9	111	0	0.0353	0.0203	0.011
194AU	107.4	278.2	5+	6+	M1	600(8) ms	1.1 NS	170.8	77.5	93.3	0.001	-0.6	1.582	0.0205	0.011
109PD	113.4	291.4339	1/2+	3/2+	M1	380(50) ns	136.5 PS	178	148	29.6	0.0143	0	0.0776	0.0218	0.01
165DY	108.1552	158.5885	1/2-	3/2-	M1	1.257(6) min	1.8 NS	50.43	35.2	15.2	0.005	0.39	2.79	0.0291	0.009
178HF	1553.997	1636.727	6+	5-	E1	77.5(7) ns	0.4 NS	82.73	6.65	76.1	0.000068	0	0.586	0.00949	0.009
132SB	85.55	426.07	3+	2+	M1	15.62(13) ns	15.8 PS	340.5	304	36.7	0.029	0.2	0.0226	0.0143	0.008
193IR	80.239	299.396	11/2-	7/2-	E2	10.53(4) d	0.19 NS	219.2	131	88.1	71	0	0.254	0.0249	0.008
161DY	25.65136	74.56668	5/2-	3/2-	M1	29.1(3) ns	3.14 NS	48.92	33.7	15.2	0.0115	-0.056	3.05	0.023	0.007

4.6

Future Work

In order to make best use of the NEEC database and companion tool, various additions should be made, to keep the calculations at the forefront of isomer depletion:

- The NEEC candidate database must be extended to include nuclear excitation by muon capture (NE- μ C) experimental techniques [56], the setup required for this is likely similar to an EBIT, and NE- μ C has recently been reported theoretically as a promising alternative to NEEC, with larger resonance strengths due to the more penetrating orbits in muonic atoms. One should use the EBIT list as a starting point and evaluate the NE- μ C rates using the *ab initio* resonance strength.
- An enrichment study should be completed by evaluating the isomer production yield of the top 100 isomer candidates via all possible mechanisms.
- Develop the database into an overall depletion tool by incorporating all other depletion mechanisms such as nuclear excitation by electron transition (NEET) or photo-excitation, thus, one will have the ability to globally study and optimise nuclear battery techniques and isomer mediated astrophysical pathways.

Chapter 5

Exploration of the Beam Approach - Channeling Proposal and Developments

We have seen that the plasma approach can be optimised by using both the combination of rep rate and electron temperature for a very hot-dense plasma or for a cooler temperature we have designed a method to compute and analyse the optimal environment based on the charge state distribution. In any case the electron density needs to be maximised.

For the beam-foil approach, one can supposedly separate the distinct deexcitation signatures in space and time due to the ion species moving along a well defined path with a separate transverse and longitudinal velocity phase space and precise time signature. This certainly opens up the possibilities for detection, yet, unfortunately the probability of close nuclear encounters is increased without the plasma effects such as Debye shielding [38]¹. An ion will likely inelastically scatter via virtual photon exchange when within an impact parameter close to the nuclear radius.

¹in which free electrons in a plasma surround the ions inducing a quasi-neutrality at certain length scales

5.1

Detection Experimental Techniques

There are several detection methods available in the ion-beam experiment:

1. Gamma Detection
2. Conversion electron detection
3. Specific gamma detection via xray mirrors
4. Recoil Tagging for exclusion of Coulomb excitation
5. Triple coincidence detection

This chapter analyses whether an increase in the ion-electron density due to channeling, can increase the NEEC rate enough to be observable over Coulomb excitation (CoulEx). There is also the ability to vary the entrance beam energy, which would enable the experimenter to characterise CoulEx as part of the experiment.

5.2

Choosing a distinct NEEC Pathway

5.2.1 Triggering in a Beam-Foil geometry

If the NEEC candidate is traveling as a beam, there are a plethora of ways one can 'present' the capture electrons; such as the delta (ionized) electrons in a warm solid, or weakly bound valence electrons in a crystal as already mentioned. If the target is a randomly oriented solid, then the emergent beam will have experienced inelastic nuclear reactions, such as Coulex.

The beam will invariably lose energy in discrete steps as collisions occur as in the example given for ^{93m}Mo shown in figure 5.1. This experiment was carried out in early 2018 at Argonne, with positive evidence of depletion, that was not necessarily due to NEEC [22]. Although useful, supporting the existence of depletion, it is not necessarily the best or most useful candidate system for NEEC identification. Thus stimulating the need for an all inclusive search algorithm that was presented in the previous chapter.

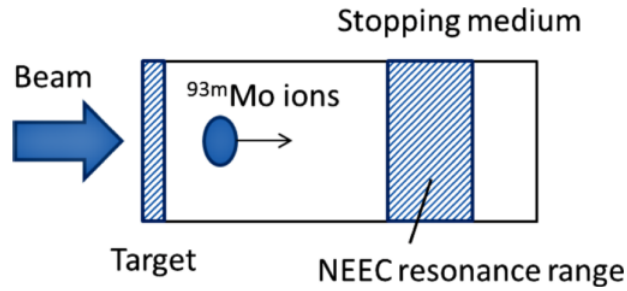


FIGURE 5.1: General schematic of a Nuclear Beam experimental scheme, from [57]. The 'target' is used to produce $A(i)N_j$ (charge state $(Z-i)^+$, isomeric) type ions via fusion evaporation reactions, which pass through the 'stopping medium' in which NEEC occurs. The thickness of the 'stopping medium' is chosen so that Coulex is suppressed and enough $A(n)Ni$ are NEEC'ed for detection. If one is confident in an estimate of the competing nuclear excitation rates, it is very likely any considerable increase in the nuclear excitation number is due to NEEC ... as in the successful experiment at ANU in which the stopping medium was largely solid C

We draw attention to calculations in [57], shown in figure 5.2 which was a precursor to the experimental setup used in [22]. Clearly a wider capture level width ($\Gamma_{neec} \approx \Gamma_{atomic}$) is preferable, and thus a case which allows the impact electron energy E_e to remain within the resonance width as long as possible is preferable. We showed though in chapter 3 that by applying the narrow resonance approximation, the NEEC probability is independent of the NEEC width.

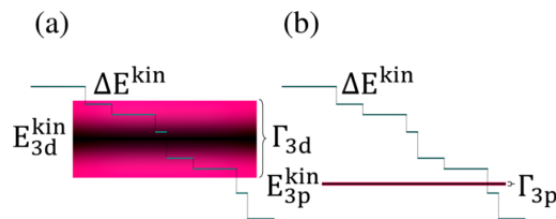


FIGURE 5.2: a) Stochastic energy loss through ^{93m}Mo 3d capture width b) Stochastic energy loss through ^{93m}Mo 3p capture width (very narrow!) [57].

5.3

Channeling: Selling Points and Theory

The high electron number density in a crystal channel $\sim 10^{23} \text{ e}^- \text{ cm}^3$ is comparable to plasma electron number densities. With a high enough beam intensity, one could equal

or even exceed the plasma ion-electron density. Coupled with the detection benefits, this method seems highly attractive. One must calculate the fraction of particles that are channeled.

Much of the early theoretical work on NEEC (1990s) was based around a fully stripped ion beam channeling scenario, which involved passage of a nuclear beam through the open 'channels' of a {110} crystal such as Si. A well channeled nucleus will experience correlated collisions with the most weakly bound electrons in the solid.

Thinking in terms of flow dynamics, the channelled particles become laminar (follow smooth paths in layers until scattered) and uncorrelated; the behaviour of an ensemble of entrance particles can be considered independently, and its motion is due to a string potential² of the aligned crystal lattice.

With the correct crystal alignment, thickness, and rectilinear beam dynamics, an ion can travel through a crystal with a suppressed nucleus-nucleus (collision and Coulex) interaction cross-section due to charge screening and 'see' mainly a dense electron gas.

Condensing the theoretical work of Datz *et al* in [58], to a good approximation, the transverse energy of a channeled ion (total energy E_{beam}) must be conserved, and be less than the thermal vibration amplitude of the crystal atoms.

$$E_{trans} = Z_{eff}U(r) + E_{beam}\theta^2 < qU(r_{th}) \quad (5.1)$$

$Z_{eff} = Z - i$ is the effective nuclear charge for an i electron ion, and $U(r)$ is the *axial* continuum potential. The critical angle of incidence (θ) for channeling, which must be obeyed to avoid fountaining of the beam, is

$$\theta < \theta_c = \left(\frac{Z_1 Z_2 e^2}{Ed} \right)^{\frac{1}{2}} \quad (5.2)$$

So the emittance of the incident beam and the temperature of the crystal should be chosen wisely so that the beam is *well-channeled*.

In channeling there are several excitation mechanisms which have been discussed in [60], [59], which generally involve capture into excited atomic orbitals and then residual

²potential of an aligned string of nuclei, which does not vary longitudinally

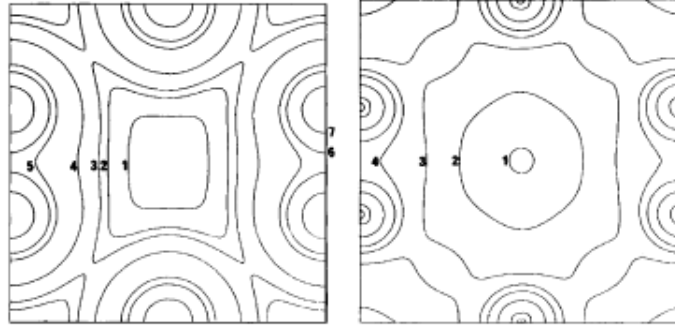


FIGURE 5.3: For Si viewed along the $\{110\}$ Miller Index. Left: Potential Map lines 1 - 7 \rightarrow 0 - 50eV. Right: Electron Density Map lines 1 - 8 \rightarrow 0 - $30 e^- \text{Angstrom}^{-3}$ [59]

energy excites electron transitions (figure 5.4), as well as direct nucleon-nucleon interactions involving close nuclear encounters (Coulomb Excitation), which are suppressed due to the limit on the impact parameter caused by channeling.

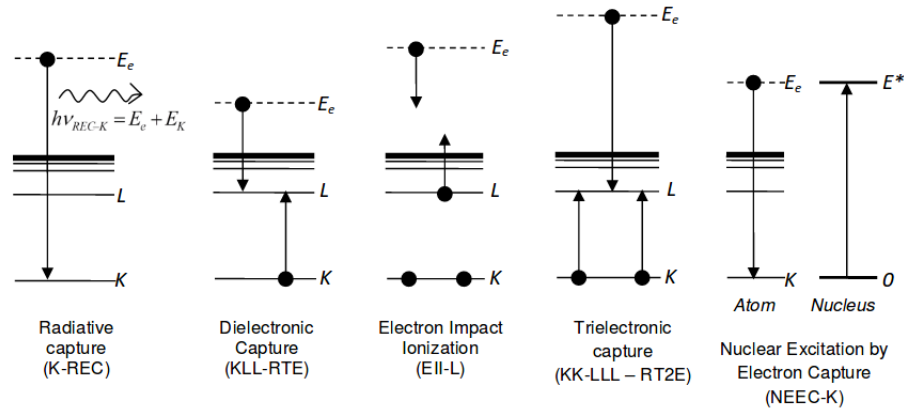


FIGURE 5.4: Competing Electronic excitation resonances [60]. These could interfere with the x-ray signature from NEEC-X

The resonance beam energy in the lab frame is calculated accurately with the expression [46]

$$E_{beam} \approx \frac{M_N}{m_e} E_e = \frac{M_N}{m_e} (Q - V_i) \quad (5.3)$$

5.3.1 Cross Section Estimates for Channeling scenario

The estimates of the cross section from this technique for some heavy nuclides are shown in table 5.1. These computations are based on approximations using partial radiative

TABLE 5.1: Differing orders of magnitude of σ_{NEEC} (which is an average cross section through the target) for some heavy nuclides, depending on the approximation used. [61]

Nucleus	J_i^{Π}	J_f^{Π}	U (MeV)	\mathcal{E} (MeV/ u)	u (MeV)	Γ_{fi} (μ eV)	Type of transition	σ_1 (mb)	σ_2 (mb)	σ^* (mb)
$^{165}_{67}\text{Ho}$	$\frac{7}{2}^-$	$\frac{9}{2}^-$	0.0947	54.2	0.0611	29.9	$E2$ $M2$	$0.48\text{E}-3$ $0.25\text{E}-3$	$0.39\text{E}-8$ $0.14\text{E}-2$	2.8
$^{173}_{70}\text{Yb}$	$\frac{5}{2}^-$	$\frac{7}{2}^-$	0.0786	12.6	0.0666	14.3	$E2$ $M1$	$0.16\text{E}-2$ $0.44\text{E}-3$	$0.11\text{E}-7$ $0.31\text{E}-2$	20.6
$^{185}_{75}\text{Re}$	$\frac{5}{2}^+$	$\frac{7}{2}^+$	0.125	76.5	0.0765	64.5	$E2$ $M1$	$0.42\text{E}-3$ $0.30\text{E}-3$	$0.70\text{E}-8$ $0.19\text{E}-2$	3.1
$^{187}_{75}\text{Re}$	$\frac{5}{2}^+$	$\frac{7}{2}^+$	0.134	92.7	0.0765	58.9	$E2$ $M1$	$0.26\text{E}-3$ $0.21\text{E}-3$	$0.67\text{E}-8$ $0.18\text{E}-2$	2.6
$^{195}_{78}\text{Pt}$	$\frac{1}{2}^-$	$\frac{3}{2}^-$	0.0989	14.7	0.0827	3.90	$E2$ $M1$	$0.21\text{E}-3$ $0.48\text{E}-4$	$0.19\text{E}-7$ $0.25\text{E}-2$	5.1

widths (σ_1), Weisskopf estimates (σ_2), and scaling of internal conversion lifetimes in [45] (σ^*).

The free electron parameters in this case are estimated for the capture of quasi free-electrons in the fermi gas of a Si {110}³ channel described above. The cross sections appear to differ vastly, and thus these approximations are too approximate, and lack information on the reduced transition probability.

5.4

Optimisation of the ^{84m}Rb experiment at TRIUMF: CouEx and Channeling

We have constructed a proposal for the channeling scenario using an ^{84m}Rb beam which was accepted by the experimental committee at TRIUMF in 2018. The original proposal is attached in appendix B, with more elaborate details calculated after submitting the proposal described in the next section. The calculations have been refined throughout the duration of this PhD as the state of the art theoretical approximations have been improved. The most up to date calculations are expressed in the progress report (composed with help from D. Jenkins and C. Murphy), which was accepted by the experimental committee in early 2022 and attached in appendix D. A visit to TRIUMF in 2019 allowed the experimental approach to be refined, and whilst there the author contributed to published work in Physical Review Letters, attached in appendix C. To properly analyse the order of events one should read appendix B, then the next 2 sections here, then appendix C and D. This may seem a little confusing but the focus of the PhD shifted drastically towards candidate searching due to COVID restrictions in 2020. We have presented this chapter in a logical manner, which is not in line with the order of events.

³this is a Miller index

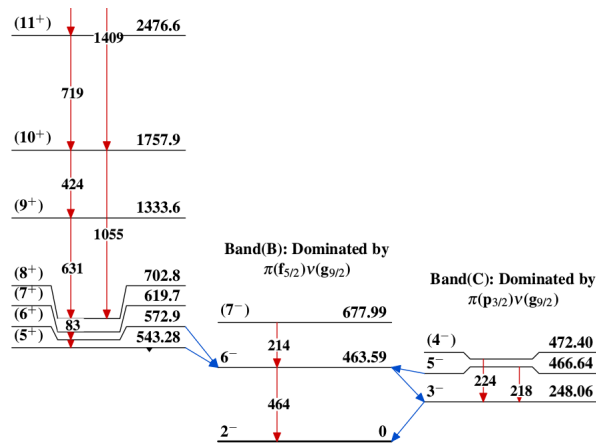


FIGURE 5.5: Relevant Parts of the ^{84}Rb Level Scheme, the 20min isomer is the 6^- level in the centre [62]

5.4.1 ^{84m}Rb Channeling experimental proposal

5.4.2 Experimental Setup

The proposed experimental setup is in figure 5.6. ^{84m}Rb at a charge state $15+$ will impinge on a Si crystal with a minimal divergence, a small fraction of which will be channeled along the crystal parallel to the atomic strings in the $\{110\}$ plane. A representation of this channeling effect is in figure 5.7. Electron capture and loss will occur during channeling due to the very high electron density experienced, which will cause charge state broadening and energy loss of the beam particles.

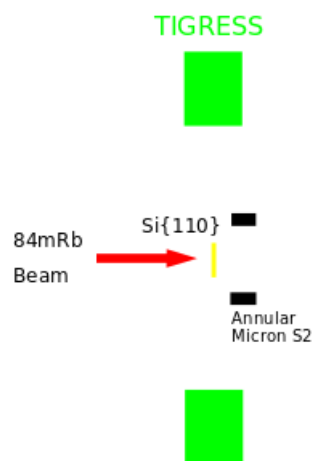


FIGURE 5.6: Basic setup for the accepted ^{84m}Rb experiment at the TRIUMF ISAC 2 beamline. The experiment is axially symmetric. The TIGRESS array will measure gamma decay in sync with the RF pulse timing for NEEC detection, and in sync with Si recoil detection in the Micron S2 detectors for CoulEx detection.

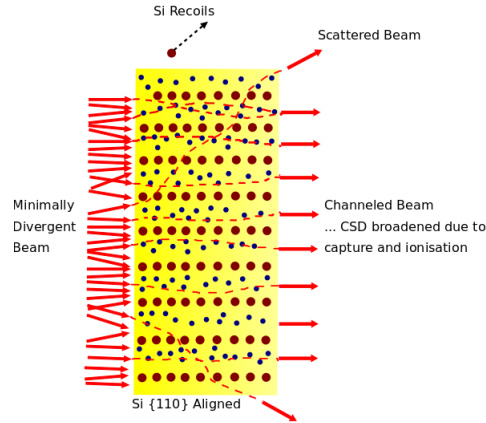


FIGURE 5.7: Inside the target

The resonance beam energies required for ^{84m}Rb NEEC, via capture into the lowest available atomic orbital at all charge states is shown in figure 5.8, with the coloured region showing the resonances met by the beam, initially at 5.55MeV/u, as it slows and broadens its CSD in the channel by around ± 4 . We will use the most stripped charge state available at the facility (15+) without sacrificing significant beam intensity. We have assumed the energy loss in a channel is $\approx 0.5 * \frac{dE}{dz}$, the energy loss for randomly orientated Si, which according to [63, 58] is a reasonable value across a wide range of beams. The distribution of energy loss is difficult to estimate analytically, due to the strong impact parameter dependence of the electronic energy loss and the complex range of transverse oscillations that can occur by beam particles in the channel [63], which has a strong dependence on initial conditions. This needs careful simulation, and it has been judged in this work most appropriate to use the Monte-Carlo code FLUX7 [64] and Geant4 where appropriate.

Using SRIM [47], which computes the Bethe-Bloch formula for nuclear and impact-parameter-averaged electronic stopping, the stopping power of 5.55MeV/u (466MeV) ^{84}Rb is $\approx 10\text{MeV}$ per μm , and for the channeled beam will be $\approx 5\text{MeV}$ per μm . So to pass the available charge state broadened resonances, we will need a target around $10\mu\text{m}$ thick. It is possible to buy {110} aligned Si with thicknesses of several hundred microns, and we plan to thin these into $<10\mu\text{m}$ wafers using KOH solution at 90°C following the method in [65].

In the first few thousand Si atoms experienced (the first micron or so), the flux of

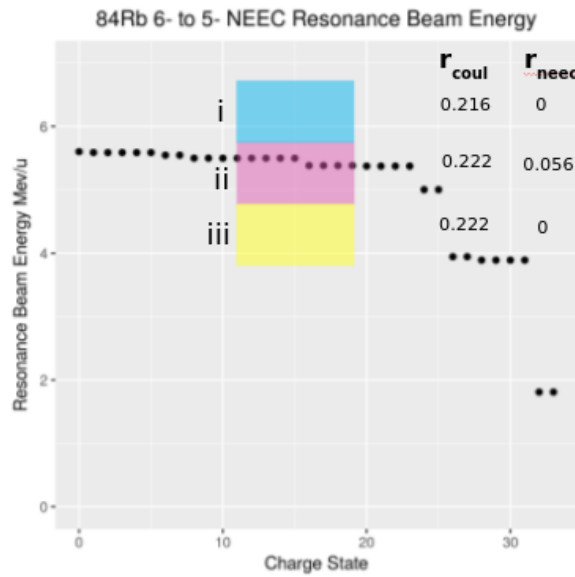


FIGURE 5.8: NEEC resonances energetically met due to the charge state broadening and energy loss of a 15+, 5.5MeV/u ^{84m}Rb beam incident on electrons at rest. Also annotated are the NEEC and Coulex rates experienced by varying the entrance beam energy

beam particles that are actually channeled will vary, and many close nuclear encounters will occur, as can be seen in figure 5.10 due to the low channeling flux (which will cause an inverse effect of ‘blocking’). Typically, at very low energies, these close encounters would be adiabatic when interacting in the electromagnetic field on the timescale of intra-nuclear dynamics, and elastic Rutherford scattering would occur. Though at these energies (~ 100 s MeV), this process becomes inelastic (**Coulomb Excitation**) and one or both of the nuclei can become excited (the nucleons don't have time to reorient themselves while being perturbed). This is especially relevant for the proposed transition ($J^\pi = 6^-$ to 5^-) due to the low multipolarity (M1 or E2).

We have used GOSIA [66] to solve the TDSE and calculate a form factor for Coulomb excitation. This allows us modify the Rutherford [differential] Cross section by an inelastic form factor, then integrate over a detectable scattering angle, giving us an approximate Coulex cross section based on various estimations of the matrix elements for the transition. We have used the M1 matrix element measured for the gamma decay of the proposed NEEC transition and a pessimistically larger value. Similarly, since the excitation is mixed, there is the possibility of E2 excitation. We have used an E2 Weisskopf estimate as a starting point, and then a much larger value. The results are shown in the table below. Evidently the cross section is very sensitive to E2 matrix elements, and we cannot

Type	Matrix Element (w.u.)	Cross Section (mb)
[M1] Gamma	0.080	0.00134
M1 Weisskopf	1	0.0244
M1 Larger	3.5	0.277
E2 Weisskopf	1	5.07
E2 Larger	5	107

TABLE 5.2: Coulomb Excitation cross sections for detection of recoils by the Micron S2 detector behind the target. The analysis is for qualitative comparison, errors are 10% as per the Gosia manual [66]. The table currently needs expanding to include mixing (M1 + E2) but we place an upper limit on E2 CoulEx by assuming it is pure E2 with an overestimated matrix element.

rule out that the proposed NEEC excitation could be strongly swamped by E2 CoulEx. We are aiming to measure the CoulEx cross section and thus extract the matrix elements directly in this experiment, so we can fully understand and discount this competing excitation. Furthermore, we will then be able to predict how the CoulEx cross section evolves with beam energy, running the beam at energies above and below the resonance region. We should then see a spike in the NEEC transition signature when we run the beam on resonance, and accurately predict how much of this yield is above the CoulEx yield.

5.4.3 Beam Dynamics

Channeling is highly sensitive to the beam dynamics at the entrance to the crystal.

Transverse particle phase space (\mathbf{x}, \mathbf{a}) and (\mathbf{y}, \mathbf{a}) , where x or y is the displacement of a beam particle off the ideal trajectory and a the divergence, is distributed as a bivariate Gaussian, limited at large values of x and a by the central limit theorem [67]. There is an ellipse that encloses a specified percentage of this distribution, which satisfies the condition:

$$\gamma x^2 + 2\alpha x a + \beta a^2 = \varepsilon \gamma = \frac{1 + \alpha^2}{\beta} \quad (5.4)$$

Where α, β and γ are the twiss parameters (not to be confused with relativistic Lorentz factors) that define the ellipse based on the various focusing and steering magnets of the accelerator lattice. ε is the geometric emittance of the accelerator, the area $\pi\varepsilon$ (the area

of the geometric ellipse) is conserved, as a fundamental property of beams according to Liouville's Theorem [68].

The divergence is defined as $a = \frac{p_x}{p_z} = \tan \theta \approx \theta$ for small angles, where θ is the angle a beam particle's velocity makes with the beam direction. Ideally for channeling we would want the beam to be entirely rectilinear (i.e. parallel to the beam direction and perpendicular to the target surface), so the beam particles that hit the channels will remain channeled. Realistically, all we can do is tune the shape of the available phase space ellipse (defined by the accelerator lattice), so that it is minimally divergent (small a), at the expense of a large beam waist (large x). By evaluating equation 5.4 and finding the maximum points of x and a , and assuming final focus will produce an uncorrelated ellipse ($\alpha = 0 \implies \gamma = \frac{1}{\beta}$), we can set the following constraints on the beam:

$$\varepsilon = \frac{x^2}{\beta} + \beta a^2 \quad (5.5a)$$

$$\implies x_m = \sqrt{\varepsilon \beta_x} \quad (5.5b)$$

$$a_m = \sqrt{\frac{\varepsilon}{\beta_x}} \quad (5.5c)$$

The possible transverse beam parameters have been quoted via correspondence with TRIUMF [69] between the following range:

- 90% Emittance $\varepsilon = 3.68$ mm mrad (emittance whose ellipse encloses 90% of the beam particles)
- $\beta_{x,y} = 25\text{cm} \implies x_m = \pm 0.959\text{mm}$ by $a_m = \pm 3.84\text{mrad}$
- $\beta_{x,y} = 6.25\text{cm} \implies x_m = \pm 0.48\text{mm}$ by $a_m = \pm 7.67\text{mrad}$

The beam particles in transverse phase space which obey $\theta < \theta_c$, Lindhard's critical angle [70], will instantly be channeled. At the resonance beam energy, $\theta_c = 0.033\mu\text{rad}$ for axial channeling. We can check the channeled fraction by generating random numbers distributed as a bivariate Gaussian with $\sigma_x = \frac{x_m}{n}$ and $\sigma_a = \frac{a_m}{n}$; $n = 1.645$ corresponds to 90% confidence. Some calculations of the initial channeling probability based on the quoted beam parameters are shown in figure 5.9, which shows an upper limit channeled fraction 10^{-4} .

It is no doubt a concern that the initial channeling probability is so low, but the actual channeled fraction could be an order of magnitude higher, due to scattered beam particles channeling along different axial and planar channels further into the target. This would require a thorough Monte Carlo simulation, but at least using Lindhard's critical angle, we are able to conclude if this technique is worth simulating.

The most appropriate detection station at TRIUMF is TIGRESS, a spherical array of array of gamma detectors, which we will use to measure the triggered de-excitation caused by NEEC from the 6^- ($T_{\frac{1}{2}} = 20\text{min}$) to the 5^- ($T_{\frac{1}{2}} = 9\text{ns}$) level, the energy matching of which is shown in figure 5.8, and the nuclear levels relative to the isomer shown in figure 5.5. For the de-excitation from the $84\text{Rb } 5^-$ level there will be a 218 keV (9ns) gamma followed by a 248keV ($T_{\frac{1}{2}} = 0.3\text{ns}$) gamma from the 3^- level within a few ns or so, which will be the signature of NEEC + CoulEx. We have proposed replacing the Ge detectors (which typically have 10ns resolution) with LaBr (<1ns resolution) to allow us to resolve these decay events in coincidence with each other *and* between each ion bunch from the accelerator. Using low level RF which is synchronized with the accelerating cavity RF, we can record time stamps for each ion bunch entering the target, and store prompt gamma events that follow within $\approx 30\text{ns}$, the ion bunch separation will be 85ns. A NEEC (signature) event is defined as a beam bunch entering the target followed by a 218keV gamma and then a 248keV gamma, well before the next bunch (85ns later). Since the beam velocity is $\approx 0.1c$, we will have to apply a Doppler correction to the measured gamma energies at the detector array.

The measurable NEEC and Coulex count rates in [s^{-1}], are computed as follows

$$\mathbb{R}_{tot} = R_{NEEC} + R_{CoulEx} \quad (5.6)$$

$$R_{NEEC} = \phi_{target} f_{ch} \sigma_{NEEC} n_e f_{det} \delta z \quad (5.7a)$$

$$R_{CoulEx} = \phi_{target} \sigma_{coul}(E) \rho_{nuc} f_{det}^c z_{target} \quad (5.7b)$$

where the channeled fraction $f_{ch} = \int_{z=0}^{z=10\mu\text{m}} P(z) dz$ and $P_{ch} = P(z=0)$.

$P(z)$ is the time averaged total channeling probability at a certain distance through the

target, and could be as high as $100 * P(z = 0)$. This arises since $P(z)$ varies drastically during scattering through each layer of crystal atoms, allowing new channeling directions to come into play [71]. f_{det} is the detectable fraction of NEEC's, which depends on the detection efficiency of TIGRESS. The physical resonance width $\delta z = \frac{\Gamma}{dE/dz}$ arises due to the atomic width $\Gamma = 8\Delta V_i \approx 8 * 1\text{eV}$, where the thickness of the target in which the resonance can occur is determined by the rate of energy loss of the beam in a channel; the factor 8 accounts for the number of resonances we can hit due to the charge state broadening.

Using the most conservative estimates for each element of equation 5.7, the NEEC rate could reasonably be tuned to 0.1 (1) detectable NEEC's per second. In the worst case scenario, the detectable CoulEx rate will be 100 (1000) per second, although could be reduced to 1s^{-1} given the impact parameter (scattering angle) reduction of channeled particles.

For CoulEx, the rate will depend on the beam energy and how the cross section evolves as a function of this. The cross section is also dependent on the nuclear impact parameter range, which is strongly reduced during channeling. Hence a good model for the channeling fraction and ability to distinguish channeled particles will be useful in discerning R_{NEEC} from R_{CoulEx} . f_{det}^c here depends on the Si recoil detection efficiency multiplied by the TIGRESS array efficiency. The missing link in connecting the observed rates with theoretical predictions requires us to model the evolution of the channeling probability $P(z)$ and energy loss throughout the target.

To separate the CoulEx background we will first run the beam at the resonance energy (5.55MeV/u) on a Pb Target for 1 shift to extract the transition matrix element. We will then run the beam for 3 shifts at 1 MeV/u above and below the resonance energy, avoiding the NEEC resonances either side. Knowing the matrix element will allow us to predict how the cross section and thus how the CoulEx rate will evolve through the NEEC resonance energy, producing a definite spike in the total depletion rate. We aim to run at resonance for 9 shifts (each shift being 8 hours).

The accuracy of our simulations of $P(z)$ and $\frac{dE}{dz}$ will affect how precisely we can compute the peak value of σ_{neec} from the experiment. This is our proposed link with theoretical predictions, which are yet to be calculated by collaborators. One should start with the simulation programs such as FLUX7 [64], a modification of Geant4 [72] proton

channeling, or any computationally efficient Monte-Carlo simulation.

5.4.4 Setting Up Analysis of Results - Extracting the matrix element and comparing the results with theory

It has been evident through attending a CoulEx school, and conversations with colleagues, that in a dense and partially collective nuclear level scheme; the extraction of matrix elements and shape parameters in order to evaluate offline the unknown matrix elements in order to eliminate the competing depletion is extremely time consuming $\sim 1-2$ years. It is thus suggested that to continue this work, and to advance the subject of isomer depletion (and NEEC verification), there is funded a new PhD student to focus entirely on CoulEx and channeling based on our results in this chapter. Such analysis needs experimental-theoretical collaboration before the experiment and the most novel and sensitive detectors to properly eliminate the non-depletion contribution to the detection spectrum. In future work, the candidate searching technique needs to be expanded into the beam-foil approach, by connecting the NEEC database with inputs to GOSIA and SRIM. The candidate environments are expected to be similar to those identified in the plasma approach, but a different analysis should be made of the charge state distribution.

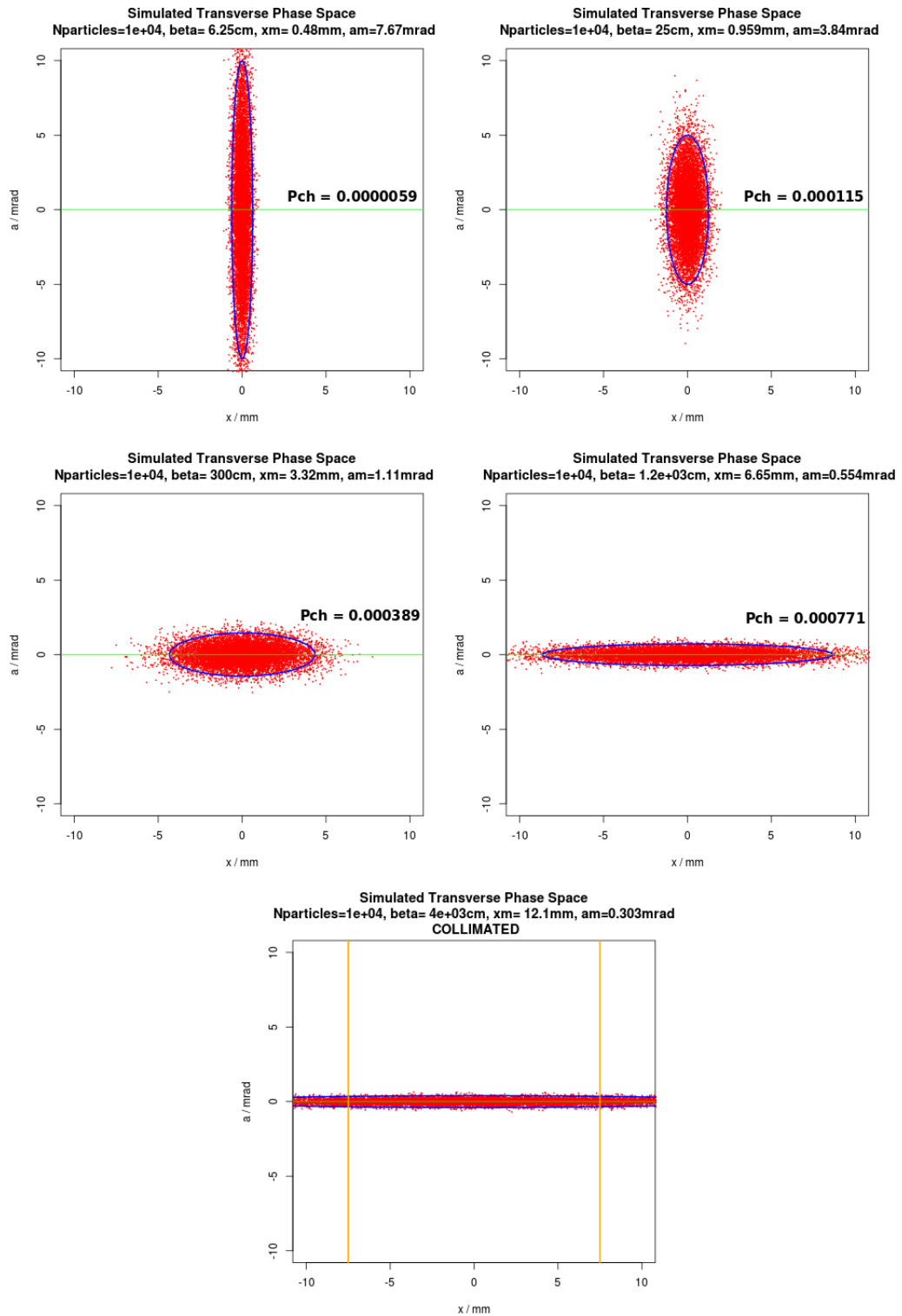


FIGURE 5.9: Change in the Transverse phase-space calculated as a function of Twiss β . The top row corresponds to the quoted range of β for final focus. The bottom row corresponds to an increase in β , which would require re-optimising the focusing quadrupole strengths. The green line roughly represents the area in which beam particles will be initially channelled. Orange lines represent a spacial cutoff (collimation). The best case channelled fraction is $\sim 10^{-4}$

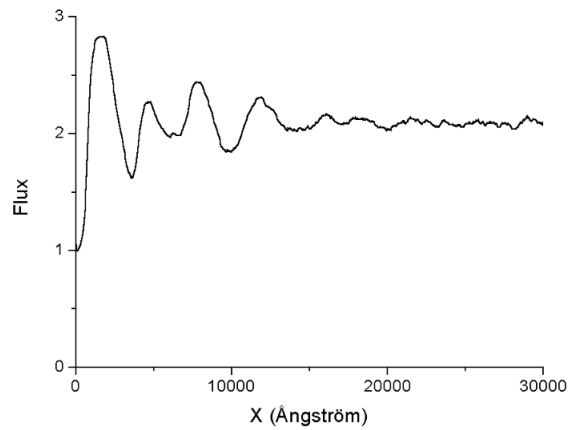


FIGURE 5.10: Channeling Flux of proton beam particles [63]. Stabilisation takes around $2\mu\text{m}$, where CoulEx will then be suppressed. The situation will be similar for a nuclear beam, as the effects on the proton can be scaled by Z .

Chapter 6

Conclusions

In this thesis we have presented the generalised NEEC rate equations using the principle of detailed balance and assessed the limitations of the principle. The cases for different NEEC pathways have been identified and assessed individually in order to calculate an accurate-enough total NEEC rate, guaranteed as an upper limit. All currently investigated experimental approaches have been considered and generalised.

In the plasma and EBIT approach every viable NEEC candidate system has been considered and approximated as an upper limit in order to generate a master database of rates, and as such an associated experimental/theoretical tool developed to encourage extensions to this work indefinitely, so long as the tool is used by the wider isomer depletion community. Also we have enriched the possibilities for theoretical and experimental study across the nuclear chart and periodic table, by placing a limit on how much NEEC we can discount. Examples of how this tool can aid in experimental design are presented for the medium irradiance plasma approach, and a macroscopic factor is presented for the high power approach so that the experimenter can quickly and efficiently proceed in their facility choice and laser-target design. The results presented for isomeric states in chapter 4 should receive intensive focus, especially in regards to how many of the isomers one can induce into a reaction volume. Similarly, with strong NEEC rates these isomeric candidates can have astrophysical significance, which should be assessed in high electron flux environments.

Throughout this study, simplifications have been made to render the general case tractable, yet we have highlighted and defined where this is the case, logically sustaining the upper limit. The upper limit allows one to discount microscopic and macroscopic candidates that would inevitably be waste of time, without having considered all other

possible cases. One can be guaranteed the approach and the tool will lead to many future publications and experiments as the database is utilised by groups worldwide. The malleability of this search is expected to save a lot of people a lot of time since the mechanism in the constructed database can be changed to any reaction type, and thus we have designed a methodology that will massively enrich the field of isomer depletion.

In the final chapter, details of an experiment and accepted proposals are given. This experiment should be carried out as soon as possible to assist with challenging the unclaimed isomer depletion probability in the NEEC discovery experiment. Extensions to the NEEC candidate tool should be made to design the best course of action in beam-foil experimental depletion design.

Appendix A

Theoretical Computation of Internal Conversion Coefficients

Analytically, in [7], The IC coefficient is calculated as:

$$\alpha_i(\tau L) = \alpha_{FS} \pi \omega \frac{2j_i + 1}{L(L+1)} \sum_{k_f} |C_{j_i-1/2}^{j_f, -1/2} (R_{k_f}^{(\tau L)} + T_{k_f}^{(\tau L)})|^2 \quad (\text{A.1})$$

Where α_{FS} is the fine structure constant and $C_{j_i-1/2}^{j_f, -1/2}$ is the Clebsch-Gordon coefficient. R and T involve integrations over large and small components of the Dirac equation and nuclear current densities.

Appendix B

Original Channeling Proposal

Submitted to TRIUMF

The EEC committees strongly recommend that you limit your submissions, including figures and tables, to no more than 4 pages for the MMSEEC or 10 pages for the SAPEEC. The following information should be included:

- (a) **Scientific value of the experiment:** Describe the importance of the experiment and its relation to previous work and to theory. All competitive measurements at other laboratories should be mentioned. Include examples of the best available theoretical calculations with which the data will be compared.
- (b) **Description of the experiment:** Techniques to be used, scale drawing of the apparatus, measurements to be made, data rates and background expected, sources of systematic error, results and precision anticipated. Compare this precision with that obtained in previous work and discuss its significance in regard to constraining theory. Give a precise list of targets to be used in order of their priority.
- (c) **Experimental equipment:** Describe the purpose of all major equipment to be used.
- (d) **Readiness:** Provide a schedule for assembly, construction and testing of equipment. Include equipment to be provided by TRIUMF. For secondary beam for ISAC, provide information on established yields of the isotope of interest as well as the established isobaric contaminants form the same target/ion-source combination.
- (e) **Beam time required:** State in terms of number of 8-hour shifts. Show details of the beam time estimates, indicate whether prime-user or parasitic time is involved, and distinguish time required for test and adjustment of apparatus.
- (f) **Data analysis:** Give details and state what data processing facilities are to be provided by TRIUMF.

For μ SR experiments, make sure that your detailed information includes:

- a concise summary of the scientific problem under investigation, with appropriate literature references;
- clear justification for the proposed experiments and, specifically, a justification for using μ SR/ β -NMR techniques;
- a description of the experimental techniques to be used, naming the μ SR/ β -NMR spectrometer(s) or ISAC facilities to be used;
- an analysis of beam time requirements, including a prioritized list of samples;
- groups with multiple experiments should list all concurrent experiments and proposals, including outside of TRIUMF, with an indication of how the personnel effort is to be divided between these activities.

1 Background and Scientific Value

Nuclear excitation via electron capture (NEEC) is an excitation process in nuclei which has important consequences in nuclear astrophysics, first suggested by Goldanskii and Namiot in the 1970s [1]. It corresponds effectively to the inverse of internal conversion, where, instead of a state emitting a conversion electron with defined energy corresponding to the difference of the nuclear transition energy and the electron binding energy, a nucleus is excited by encountering an electron which gains energy on becoming bound. The energy balance for a typical candidate nuclide is displayed in figure 1. Evidently one must present electrons with the correct energy, but also one must carefully choose a nuclear transition and subsequent atomic capture orbital.

The NEEC excitation mechanism could have the effect of depopulating isomers in astrophysical plasma environments where nuclei are often highly ionized [2]. The consequences of this are not fully explored as the mechanism is not completely understood. There is a large theoretical literature related to NEEC and the potential to observe it in different experimental environments such as beam-target interactions, laser-plasma interactions and in electron-ion traps: for example, the first attempt at calculating an analytical cross section, by scaling internal conversion coefficients [3], and extensions of this early work using a Feshbach formalism which accounts for all interactions terms in the Hamiltonian [4]. Analytical calculations, based on this theory, have also been made for the observation of NEEC in laboratory laser produced plasmas [5] (See Fig. 2).

However, despite the extensive theoretical literature, there is only one, very recent report of experimental observation of NEEC in Nature in 2018 [6] making this issue highly topical. The observation was made using the approach of ‘isomer depletion’. The long-lived isomer, ^{93m}Mo was produced using a fusion-evaporation reaction and the isomer recoiled through a thick lead backing. The NEEC process pumps the long-lived isomer up to a close-lying excited state which decays by characteristic delayed gamma-ray emission, due to the few ns half-life of the excited state. The relative energy of the recoiling isomers (which will necessarily have a broad energy distribution from the production mechanism) and target electrons is not precisely controlled. Rather, it is relied on that the recoiling isomers will encounter resonances where the electron energies match while slowing down in the thick foil (see figure 3).

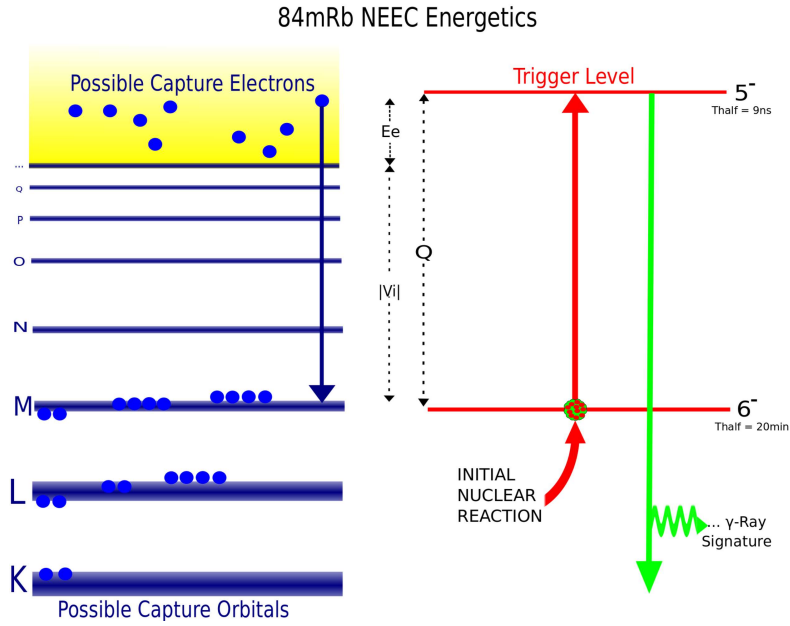


Figure 1: Energy matching for ^{84}Rb M-shell NEEC. Left: Atomic System, Right: Nuclear Transition

The reported probability for NEEC excitation in ^{93m}Mo was $P_{exc} = 0.010$, while the Coulomb excitation probability was estimated to be 2×10^{-6} over the target. This was calculated using a highly simplified level scheme, with unknown matrix elements taken from ^{93}Mo input into GOSIA. This suggested that the average NEEC cross section through the target was around 40 b, meaning that at the resonances where it takes place, the peak cross sections must be extremely large. However, the major limitation of the ^{93m}Mo measurement is that the ^{93m}Mo is produced as a secondary beam with a broad range of energies and angles, transiting a thick target so the details of the excitation process are not fully under control. Nevertheless, it sets a value on the integrated cross section which is a challenge to contemporary theory.

2 Experiment Description

The experimental conditions for a NEEC investigation may be much better controlled than in the discovery experiment, as well restricted to a specific set of electron resonances, by using an accelerated radioactive beam of the isomer of interest. A ^{93m}Mo beam is difficult to produce with the ISOL technique due to the refractory nature of Molybdenum. However, an ^{84m}Rb beam can be readily produced with significant intensity and the experimental conditions are extremely similar. The ^{84m}Rb isomer ($J^\pi = 6^-$) has a half-life of 20.26 min and an excitation energy of 463.59 keV. A ($J^\pi = 5^-$) state is available at 466.64 keV which can be excited via the NEEC process. The high precision on the excited state energies is invaluable in defining the conditions to match to electron energies.

The 5^- state has a half-life of 9 ns meaning that it can be readily distinguished via its delayed gamma-ray emission, which bypasses the long-lived isomer and cascades to the ground state via a 3^- state at 248 keV. This presents, therefore, a highly characteristic decay cascade readily identifiable using gamma-ray detection relative to the RF timing to identify the delayed gamma rays. For the delayed gamma ray emission, the TIGRESS array could be augmented by replacing the forward detectors by eight $\text{LaBr}_3(\text{Ce})$ detectors from the GRIFFIN array will be used. The excellent timing

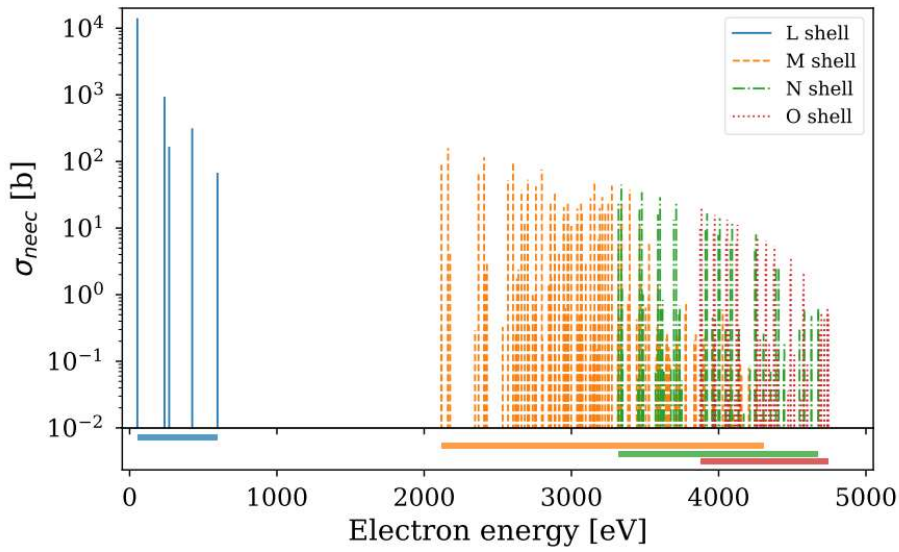


Figure 2: Peak Cross Sections for ^{93m}Mo NEEC isomer triggering for different capture shells. Note a 4 keV electron energy would correspond to a beam energy of $\approx 7 \text{ MeV/u}$ [5]

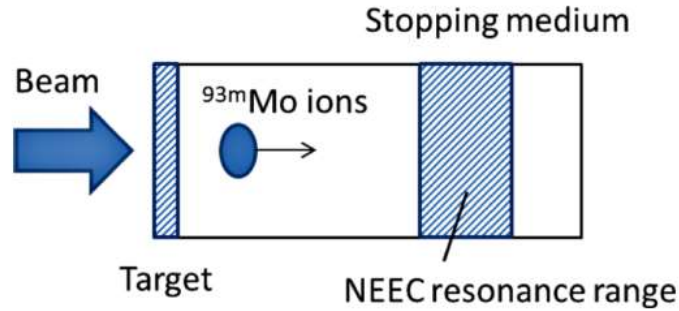


Figure 3: Principle Behind the First Observation, the fusion evaporation recoils would drift into stopping medium after a short distance, in a rather uncontrolled manner [6]

resolution of the $\text{LaBr}_3(\text{Ce})$ detectors would be very helpful since the timing with respect to the RF pulse can be used to determine the point where the ions, flying away from the target at high velocity, emit the delayed gamma ray. This can be used to account for the Doppler effect due to uncertainty in relative angle of emission in this case and restore the intrinsic resolution of the detectors. Nevertheless, the goals could be achieved with just the TIGRESS detectors on their own.

The approach to be taken in the present experiment would be to accelerate the beam to an energy allowing valence and conduction band electrons in a fixed-target to be presented with impact energies (E_e) corresponding to the highly-resonant NEEC process. A schematic of the Rb capture system is displayed in figure 1. The nuclear transition (energy Q) is excited by the energy gained by a target electron on becoming bound in a vacant ion orbital (V_i) plus the impact kinetic energy E_e .

$$E_e + |V_i| = Q \tag{1}$$

Note if the capture electrons are initially at rest, one can assert the beam energy provides the impact electron energy. For the resonance to be energetically met then, by relativistic energy and

momentum conservation [7],

$$E_{beam} = \left(\frac{M_p}{m_e} + 1 + \frac{(Q - |V_i|)}{2m_e c^2} \right) (Q - |V_i|). \quad (2)$$

The width of the resonance, is dominated by the width of the atomic capture orbital. This is composed of contributions from Doppler broadening and hyperfine splitting and will be $\approx 1\text{eV}$. The fraction of impact electron energies available within this width will scale our NEEC probability through the target.

For the proposed experiment, we would prefer a narrow spread in the central energy of the beam and a narrow Compton profile of the capture electrons, which is achievable in the conduction band of Si.

2.1 Channeling

We will effectively bias the interaction towards that with electrons rather than nuclei by electing to channel ^{84m}Rb (initial charge state 15^+) ions through a thin ordered crystal of silicon. It should be noted there has been a previous attempt to observe NEEC via channeling reported in [8] using the LISE beam line at GANIL. $^{57}\text{Fe}^{26+}$ in its ground state was channeled through $\{110\}$ Si at 9.3MeV/u , with the signature decay ($T_{\frac{1}{2}} = 98\text{ns}$) detected via conversion electrons in a 6m drift between dipoles. It is thought the lack of signature was due to the poor vacuum conditions in the drift region, preventing the sensitivity required to observe the effect above the background.

In the present experiment, the beam energy (approximately 5.55 MeV/u) will be tuned so that the ions encounter M-shell electrons and be resonantly excited at the front of the target. As the ions lose energy, and channel through the crystal they will encounter successive regions where there is again matching with electron energies. The transition between the 466.64 keV ($J^\pi = 5^-$) and the long-lived ($J^\pi = 6^-$) isomer at 463.59 keV has been studied. The reported conversion coefficients, $\alpha_L = 304(5)$ and $\alpha_M = 50.5(7)$ support it being almost purely M1 in character ($B(M1) \approx 0.08\text{ Wu}$). The NEEC process is essentially insensitive to the multipolarity of the transition and can occur for M1, E2 etc. However, the competing process for direct excitation of the 466.64 keV ($J^\pi = 5^-$) state in the proposed experiment is Coulomb excitation which proceeds largely by virtual E2 transitions. We expect this direct process to be suppressed due to the dominant M1 character of the relevant transition. However, we cannot rule out this short-lived isomer being populated from above due to exciting higher-lying states which feed back down. Nevertheless, we anticipate that the channeling to be employed will serve to limit the Coulomb excitation process as the channeled ions will be kept far from the target nuclei. We will characterize the Coulomb excitation (in fact, Coulomb/nuclear due to the beam energy) by detecting scattered target nuclei in an annular silicon detector e.g. Micron S2, mounted at forward angles (between 30 and 60° in the lab). The choice of a silicon target should essentially limit excitations to single-step, simplifying the analysis. In this way, we should be able to account directly for the cross-section for Coulomb excitation and distinguish it from NEEC which is important as it effectively defines the sensitivity of our measurement. The ordered Si $\{110\}$ target (10 microns or thinner - in fact, as thin as mechanically possible) will be produced in the cleanrooms at the University of York. In the past, the group has developed flexible silicon detectors by thinning down silicon wafers using KOH solution at a temperature of 90°C , and so have a well defined process for producing such a target in a reliable way.

The extensive review of channeling by Cohen et al. [9], shows that a classical description of interactions can be used but they are highly stochastic, with a strong dependence on initial conditions. The energy loss is hard to compute, with the stopping power expected to be roughly half the stopping

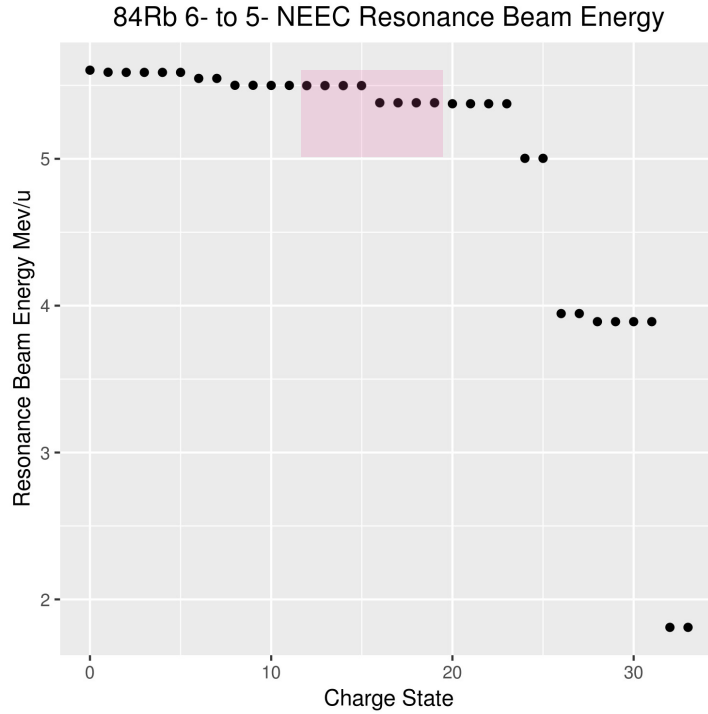


Figure 4: The electron resonances expected for the ^{84m}Rb NEEC process as a function of ion charge state and beam energy (in MeV/u). The pink region shows the approximate region to be covered in this experiment based on assumed energy loss of a 5.55 MeV/u beam with initial charge state 15^+ .

power for randomly oriented Si, see figure 5. We therefore assume this kind of reduced stopping power for our determination of the appropriate running conditions. The uncertainty in stopping powers will introduce a systematic uncertainty which we can try to control through accounting for the Doppler shift of promptly-emitted gamma rays.

2.2 Experiment plan

The NEEC cross sections are expected to be very large but highly-resonant so effectively limited to a narrow range of the target thickness. Coulomb excitation has much smaller cross sections but occurs all through the target. However, it should evolve smoothly as a function of beam energy. We therefore propose to bracket the NEEC excitation region by choosing three beam energies, one where the resonances are within the target, and two further energies above and below the resonant region where NEEC should be absent for the charge state distribution of the beam once it has encountered the target. In this way, we will be easily sensitive to a large average NEEC cross-section of order 10s of barns as reported for ^{93m}Mo but would also be sensitive to a NEEC cross-section exceeding the Coulomb excitation cross-section by a factor of 3-5, through study of the evolution of the observed cross sections with beam energy. Assuming a typical Coulomb excitation cross section of 10 mb, this means we would be sensitive down to the 50 mb level for NEEC. We cannot estimate this precisely at this stage, since the relevant transition matrix element is not known. Another source of background excitation is Resonant Coherent Excitation [10][9], where the varying string potential along the channel can virtually excite the nuclei. It has been calculated that at the energy proposed here, only the 8th and 9th string harmonic match the nuclear excitation frequency at charge states

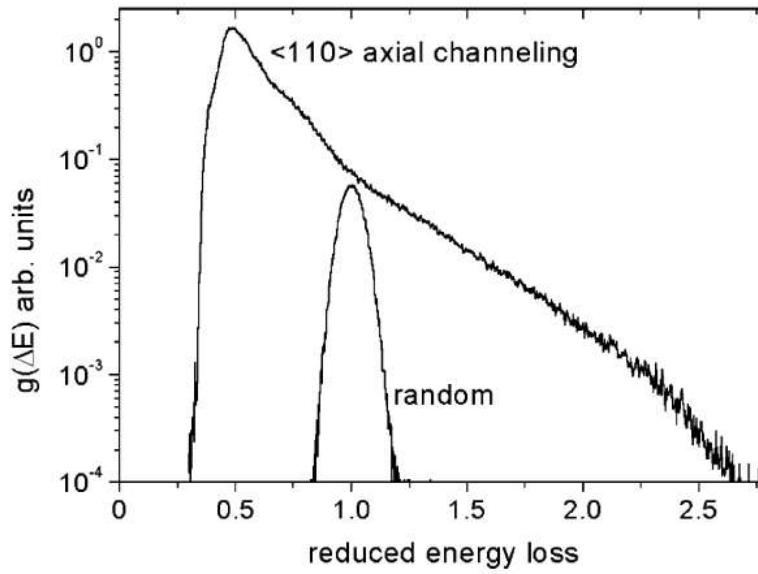


Figure 5: Broadening and shifting of the energy loss for 110 channeling compared to random oriented Si for a Pb^{56+} beam at 29MeV/u [9]. The energy loss relative to random orientation peaks significantly at 0.5; this value is further validated in [10] for Si^{14+} at 22.5A MeV

27+ and above, which will not be reached given an initial charge state 15+.

Assuming a Coulomb excitation cross-section of 10 mb , beam current of 10^7 s^{-1} and silicon target thickness of 10 microns, the rate of excitations per second from the isomer to the nearby excited state would be 5 per second. With an estimated gamma-ray efficiency of 5% for detecting either of the de-excitation gamma rays, this implies a rate of detected delayed events of 0.5 per second, or around 2000 per hour. However, to characterise the Coulomb excitation, we can only cover a fraction (perhaps 10% of the scattered target ions with the annular silicon detector), implying 200 correlated events per hour (or 1600 per shift). We should be conservative, in that the effective cross section could be as small as 1 mb especially as we are attempting to suppress Coulomb excitation by employing channeling, which should still be compatible with the predicted rates.

3 Readiness

The TIGRESS array plus annular silicon detector is a standard set-up and so requires no special work-up. The $\text{LaBr}_3(\text{Ce})$ detectors are standard within the GRIFFIN setup which has a largely mechanically compatible frame with TIGRESS but would need some work in terms of fitting the detectors and the electronics if this option is pursued.

Reported primary yields at TRIUMF for $^{84\text{m}}\text{Rb}$ are very large e.g. in the 10^{10} particles per second range from a ZrC primary target. Even with a relatively low efficiency ($< 1\%$) for re-acceleration, it should be possible to have an accelerated beam in excess of 10^7 particles per second. Likely beam contaminants are radioactive ^{84}Sr and stable ^{84}Kr . Such beam components should not present any difficulty to the proposed identification technique as no delayed gamma rays are expected from their excitation so they would effectively spectate. The beam will not be stopped in the target and should be dumped some distance away to provide clean conditions for a delayed-gamma ray analysis.

4 Beam Time Required

The beam would firstly be tuned to 5.55 MeV/u. A Pt or Pb target would initially be installed to characterise fully the Coulomb excitation making good use of the range of available angles in the annular silicon detector. This would allow extraction of the E2 transition matrix element for the transition of interest and other excitations. Since high precision is not needed, we request one shift to make this initial measurement. We will then install the silicon channeling target and take data for nine shifts. The beam energies will then be changed successively to 6.5 MeV/u and 4.5 MeV/u, above and below the NEEC resonance region. Data will be taken for three shifts at each energy. We assume one shift is required to change energy. This makes a total of eight shifts for this part of the experiment.

The total beam time requested is therefore 18 shifts (6 days).

5 Data Analysis

The data analysis will be carried out by Ben Wallis, a PhD student at the University of York. The work will comprise the mainstay of his PhD project. Given that Ben spent the first year of his PhD investigating the NEEC process and identifying candidates, he currently does not have a dataset to analyse. It would therefore be of high benefit to his studies to carry out this experiment as early as possible in 2019.

The University of York has a long-standing connection with TRIUMF and the TIGRESS programme meaning that there is considerable expertise in-house to support this analysis. The York group is also expert in GOSIA analysis of Coulomb excitation which will be necessary to characterize the background to the NEEC process.

References

- [1] V I Goldanskii and V A Namiot. “On the excitation of isomeric nuclear levels by laser radiation through inverse internal electron conversion”. In: *Physics Letters B* (1976). ISSN: 03702693. DOI: 10.1016/0370-2693(76)90665-1.
- [2] G. Gosselin and P. Morel. “Enhanced nuclear level decay in hot dense plasmas”. In: *Physical Review C - Nuclear Physics* 70.6 (2004), pp. 1–9. ISSN: 1089490X. DOI: 10.1103/PhysRevC.70.064603.
- [3] Zhu-Shu Yuan and J C Kimball. “First-principles calculation of the cross sections for nuclear excitation by electron capture of channeled nuclei”. In: *Physical Review C* 47.1 (1993).
- [4] Adriana Pálffy, Werner Scheid, and Zoltan Harman. “Theory of nuclear excitation by electron capture for heavy ions”. In: *Physical Review A - Atomic, Molecular, and Optical Physics* 73.1 (2006). ISSN: 10941622. DOI: 10.1103/PhysRevA.73.012715.
- [5] Jonas Gunst et al. “Nuclear excitation by electron capture in optical-laser-generated plasmas”. In: (2018), pp. 1–18.
- [6] C J Chiara et al. “Isomer depletion as experimental evidence of nuclear excitation by electron capture”. In: *Nature Publishing Group* 554.7691 (2018), pp. 216–218. ISSN: 0028-0836. DOI: 10.1038/nature25483. URL: <http://dx.doi.org/10.1038/nature25483>.

- [7] Nelson Cue et al. "Exciting the Nucleus by Target Electron Capture into Atomic Orbitals Exciting the Nucleus by Target Electron Capture into Atomic Orbitals ." In: *Europhysics Letters* (1989).
- [8] Denis Dauvergne. "Crystal assisted experiments for multi-disciplinary physics with heavy ion beams at GANIL". In: *Journal of Physics: Conference Series* 629 (2015), p. 012010. ISSN: 1742-6588. DOI: 10.1088/1742-6596/629/1/012010. URL: <http://stacks.iop.org/1742-6596/629/i=1/a=012010?key=crossref.b135761398f59a8a96a794b67ba9da62>.
- [9] C Cohen and D Dauvergne. "High energy ion channeling: Principles and typical applications". In: *Nuclear Instruments and Methods in Physics Research, Section B: Beam Interactions with Materials and Atoms*. 2004. DOI: 10.1016/j.nimb.2004.03.017.
- [10] J. U. Andersen et al. "Heavy ion channeling". In: *Nuclear Instruments and Methods in Physics Research, Section B: Beam Interactions with Materials and Atoms* (1996). ISSN: 0168583X. DOI: 10.1016/0168-583X(96)00209-1.

Appendix C

PRL: First Direct Measurement of an Astrophysical p-Process Reaction Cross Section Using a Radioactive Ion Beam

First Direct Measurement of an Astrophysical p -Process Reaction Cross Section Using a Radioactive Ion Beam

G. Lotay,¹ S. A. Gillespie,^{2,†} M. Williams,^{2,3} T. Rauscher,^{4,5} M. Alcorta,² A. M. Amthor,⁶ C. A. Andreoiu,⁷ D. Baal,² G. C. Ball,² S. S. Bhattacharjee,^{2,‡} H. Behnamian,⁸ V. Bildstein,⁸ C. Burbadge,^{8,*} W. N. Catford,¹ D. T. Doherty,¹ N. E. Esker,² F. H. Garcia,⁷ A. B. Garnsworthy,² G. Hackman,² S. Hallam,¹ K. A. Hudson,^{2,9} S. Jazrawi,¹ E. Kasanda,⁸ A. R. L. Kennington,¹ Y. H. Kim,¹⁰ A. Lennarz,² R. S. Lubna,² C. R. Natzke,^{2,11} N. Nishimura,¹² B. Olaizola,^{2,8} C. Paxman,^{1,2} A. Psaltis,^{13,||} C. E. Svensson,⁸ J. Williams,² B. Wallis,³ D. Yates,^{2,14} D. Walter,² and B. Davids^{2,9}

¹*Department of Physics, University of Surrey, Guildford GU2 7XH, United Kingdom*

²*TRIUMF, 4004 Wesbrook Mall, Vancouver, British Columbia V6T 2A3, Canada*

³*Department of Physics, University of York, Heslington, York YO10 5DD, United Kingdom*

⁴*Department of Physics, University of Basel, Klingelbergstrasse 82, CH-4056 Basel, Switzerland*

⁵*Centre for Astrophysics Research, University of Hertfordshire, Hatfield AL10 9AB, United Kingdom*

⁶*Department of Physics and Astronomy, Bucknell University, Lewisburg, Pennsylvania 17837, USA*

⁷*Department of Chemistry, Simon Fraser University, Burnaby, British Columbia V5A 1S6, Canada*

⁸*Department of Physics, University of Guelph, Guelph, Ontario N1G 2W1, Canada*

⁹*Department of Physics, Simon Fraser University, Burnaby, British Columbia V5A 1S6, Canada*


¹⁰*Department of Nuclear Engineering, Hanyang University, Seoul 04763, Republic of Korea*

¹¹*Department of Physics, Colorado School of Mines, Golden, Colorado 80401, USA*

¹²*Astrophysical Big Bang Laboratory, CPR, RIKEN, Wako, Saitama 351-0198, Japan*

¹³*Department of Physics and Astronomy, McMaster University, Hamilton, Ontario L8S 4L8, Canada*

¹⁴*Department of Physics and Astronomy, University of British Columbia, Vancouver BC V6T 1Z4, Canada*

 (Received 14 May 2021; revised 19 July 2021; accepted 11 August 2021; published 10 September 2021)

We have performed the first direct measurement of the $^{83}\text{Rb}(p, \gamma)$ radiative capture reaction cross section in inverse kinematics using a radioactive beam of ^{83}Rb at incident energies of 2.4 and 2.7A MeV. The measured cross section at an effective relative kinetic energy of $E_{\text{cm}} = 2.393$ MeV, which lies within the relevant energy window for core collapse supernovae, is smaller than the prediction of statistical model calculations. This leads to the abundance of ^{84}Sr produced in the astrophysical p process being higher than previously calculated. Moreover, the discrepancy of the present data with theoretical predictions indicates that further experimental investigation of p -process reactions involving unstable projectiles is clearly warranted.

DOI: 10.1103/PhysRevLett.127.112701

It has long since been established that the stellar nucleosynthesis of elements heavier than iron is largely governed by the slow (s) and rapid (r) neutron capture processes [1]. However, there exist ~ 30 stable, neutron-deficient nuclides, between Se and Hg, that cannot be formed by either of the aforementioned processes, and whose astrophysical origin remains a subject of active investigation [2]. These p nuclides, because they account for only a small fraction of overall elemental abundances, are not directly observable in stars or supernova remnants. As such, it is necessary to study their formation using a combination of detailed nucleosynthetic models and meteoritic data [3]. At present, it is believed that p nuclides are formed by photodisintegration reactions on preexisting r - and s -process seed nuclei in the O/Ne layers of core-collapse supernovae (CCSN) [4,5] and in thermonuclear supernovae [6,7], with typical peak plasma temperatures of $T_{\text{max}} \sim 2 - 3.5$ GK in the p -process layers. In particular,

(γ, n) reactions drive the pathway of nucleosynthesis toward the neutron-deficient side of stability until neutron separation energies become high enough that (γ, p) and (γ, α) disintegrations largely dominate the flow of material. This astrophysical γ process is capable of reproducing the bulk of the p nuclides within a single stellar site [3]. However, there are abiding issues in obtaining abundances consistent with solar system values for the lightest p nuclides ($A \lesssim 110$) [8,9] to be resolved. In this regard, a possible solution may be found in the underlying nuclear physics input, as experimental cross sections of p -process reactions are almost entirely unknown, and the related reaction rates are based entirely on theoretical calculations.

It is well known (see, e.g., [10,11]) that experimental measurements for constraining stellar rates should be performed in the reaction direction of positive Q value, in order to minimize the impact of thermal excitations of target nuclei in the stellar plasma and numerical inaccuracies when

converting between forward and reverse rates. In the application to the nucleosynthesis of p nuclides, this implies that capture reactions, instead of the reverse photodisintegration reactions, should be experimentally studied. The vast majority of these reactions involve unstable nuclei and exhibit cross sections of order $100 \mu b$. As such, most p -process reactions have remained experimentally inaccessible, even with the latest developments in the production and acceleration of radioactive ion beams, and astrophysical abundance calculations have relied extensively on the use of Hauser-Feshbach (HF) theory [12,13]. Although this approach is valid for reactions appearing in the synthesis of p nuclides, the nuclear properties required as input are not well known off stability. This may lead to larger uncertainties in the predictions of astrophysical reaction rates and, therefore, requires experimental validation. Consequently, in this Letter, we present the first direct measurement of a p -process reaction involving an unstable nuclide, in the relevant energy window (Gamow window) for the γ process in CCSN ($E_{\text{cm}} \sim 1.4 - 3.3$ MeV [14]).

This pioneering study, performed at the ISAC-II facility of TRIUMF, utilized an intense radioactive beam of ^{83}Rb ions, together with the TIGRESS γ -ray array [15] and the newly commissioned EMMA recoil mass spectrometer [16], to investigate the astrophysical $^{83}\text{Rb}(p, \gamma)^{84}\text{Sr}$ reaction. In particular, by exploiting the fact that the electromagnetic decay of proton-unbound states in ^{84}Sr , populated via resonant proton capture on the $5/2^-$ ground state of ^{83}Rb , predominantly proceeds via γ -decay cascades to the lowest-lying 2^+ level, rather than directly to the ground state, it was possible to determine the reaction cross section from the observed $793.22(6)$ -keV, $2_1^+ \rightarrow 0_1^+$ γ -ray yield [17]. This not only provides valuable information for current models of p -process nucleosynthesis, but also represents a new approach to the direct measurement of astrophysical reaction cross sections. Most notably, the $^{83}\text{Rb}(p, \gamma)^{84}\text{Sr}$ reaction impacts the ^{84}Sr abundance obtained in CCSN [2,18] and elevated levels of ^{84}Sr have recently been discovered in calcium-aluminium-rich inclusions (CAIs) in the Allende meteorite [19]. While it has been proposed that the ^{84}Sr abundances found in CAIs may be accounted for by r - and s -process variability in ^{88}Sr production, such distributions are most easily described by an anomaly in the astrophysical p process.

Here, radioactive ^{83}Rb ions ($t_{1/2} \sim 86$ days), produced and accelerated to energies of 2.4 and 2.7A MeV by the ISAC-II facility of TRIUMF, were used to bombard 300 to 900 $\mu\text{g}/\text{cm}^2$ thick polyethylene $(\text{CH}_2)_n$ targets at intensities of $1 - 5 \times 10^7 \text{ s}^{-1}$ in order to perform measurements of the $^{83}\text{Rb}(p, \gamma)$ reaction cross section. A measurement of the stable $^{84}\text{Kr}(p, \gamma)$ radiative capture cross section was carried out as well at a bombarding energy of 2.7A MeV in a test of the new experimental setup with a nearly identical mass beam free from radioactive-beam-induced

background. The intensities of both the stable and radioactive beams were limited to maintain the integrity of the target foils; much greater intensity on target was available from the ISAC-II accelerator. Prompt γ rays were detected with the TIGRESS array, which, in this instance, consisted of 12 Compton-suppressed HPGe detectors [15], while recoiling ^{83}Rb and ^{84}Sr nuclei were transmitted to the focal plane of the EMMA recoil mass spectrometer [16] in either the 25^+ or 26^+ charge state. The electrodes of the two electrostatic deflectors were held at potential differences of ~ 320 kV while three slit systems enabled the rate of scattered beam reaching the focal plane to be suppressed by a factor of $\sim 50\,000$; such beam suppression was required in order to reduce radioactive beam-induced background to a tolerable level, but the slit settings did not diminish the transmission efficiency for recoils due to their small angular and energy spreads. An electromagnetic separator capable of a relatively large electrostatic rigidity of 13 MV was needed to transmit the recoils of these reactions. The rigidity limits of EMMA imply that relative kinetic energies up to 10% larger than studied here can be reached, rendering the spectrometer well matched to the Gamow window for the p process.

Recoils were highly forward focused due to the inverse kinematics and including the effects of multiple scattering in the target foil emerged at scattering angles not exceeding 0.4° . This allowed for very high recoil transport efficiency which was estimated on the basis of empirical energy and angular acceptance studies with an α source to exceed 99%. Recoils and scattered beam reaching the focal plane were detected by a parallel grid avalanche counter, a transmission ionization chamber, and a 500 μm thick ion-implanted Si detector [16].

The charge state distribution of a reduced-intensity beam of 2.7A MeV ^{84}Kr was measured and used to infer the charge state fractions of ^{85}Rb and ^{84}Sr recoils, using the dependence of the equilibrium charge state on Z and energy predicted by the empirical parametrization of Ref. [20]. The intensities of six charge states were measured. During the radiative capture cross section measurements, the integrated luminosity was obtained by monitoring target protons elastically scattered into two 150 mm^2 silicon surface barrier detectors mounted at 20° with respect to the beam axis downstream of the target position, relative to regular Faraday cup readings, while γ -ray detection efficiencies were established using standard ^{152}Eu and ^{56}Co sources. During the measurement of the $^{83}\text{Rb}(p, \gamma)$ reaction, background arose due to the presence of contaminant ^{83}Sr in the beam. In particular, ^{83}Sr scattering into the entrance aperture of EMMA resulted in the detection of ^{83}Sr β -delayed γ rays in the TIGRESS array. Consequently, immediately following the experiment, and again 22 days later, the GRIFFIN spectrometer [21] was used to study the decay of beam ions scattered into the entrance aperture; the ^{83}Rb fraction was determined to be 62(3)%.

Estimates of the relative uncertainties associated with the integrated luminosity, the recoil transmission efficiency, γ -ray detection efficiency, and charge state fractions amount to $\pm 19\%$, $^{+0.1}_{-33}\%$, $\pm 5\%$, and $\pm 10\%$, respectively. We note that the recoil transmission efficiency is known to be high based on the measured transmission of ^{84}Kr and ^{83}Rb beam ions during attenuated beam runs and due to the small recoil cone angle and kinetic energy spread of $\pm 1\%$. However, we have placed a very conservative estimate on its lower limit to account for any possible unforeseen losses during the measurement of the (p, γ) reaction cross sections, given the large energy losses in the thick targets and the unmeasured stopping powers of ^{84}Sr and ^{85}Rb ions in polyethylene. The statistical uncertainty in the data acquisition live-time fraction, which exceeded 90% for data taking with both beams, is negligible.

An example of a timing peak observed in this study, corresponding to the time difference between γ -ray events registered in TIGRESS and recoils detected at the focal plane of EMMA, is presented in Fig. 1. Such a timing peak provides clear evidence for distinct (p, γ) events and, by placing a software gate on this peak for the measurement of the $^{84}\text{Kr}(p, \gamma)^{85}\text{Rb}$ reaction, 130- and 151-keV γ rays, corresponding to decays from the $1/2_1^-$ and $3/2_1^-$ levels in

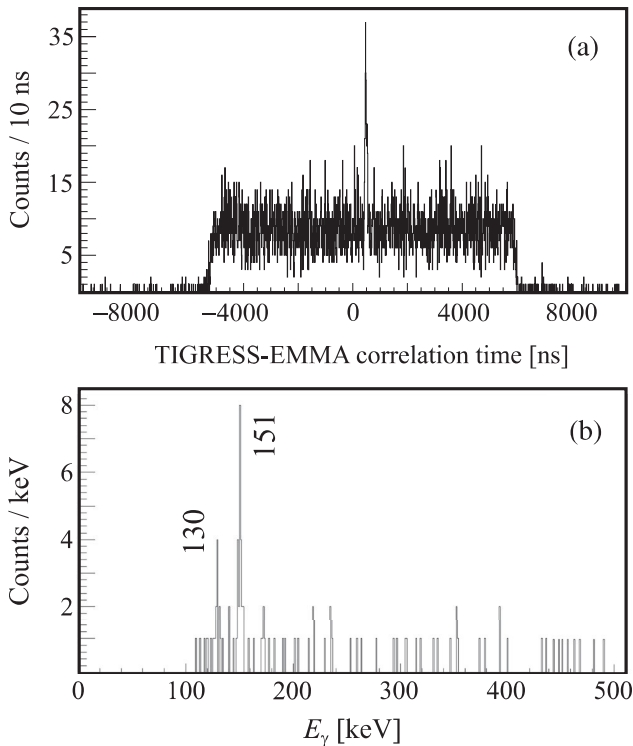


FIG. 1. (a) Time difference between events observed in the TIGRESS γ -ray array and the focal plane of the EMMA recoil mass spectrometer, following the $^{84}\text{Kr}(p, \gamma)$ reaction. (b) Energies of γ rays observed in coincidence with $A = 85$ recoils from the timing peak shown in panel (a).

^{85}Rb [22], were cleanly identified [see Fig. 1(b)]. In this case, the $1/2_1^-$ and $3/2_1^-$ excited states were populated following primary γ decays from high-lying, proton-unbound levels in ^{85}Rb . As such, the observed γ -ray intensities provide direct measures of the inclusive partial reaction cross sections. Note, e.g., that the $1/2_1^-$ state decays 99.42(9)% of the time to the $3/2_1^-$ level [22], so the total radiative capture cross section is not the sum of all the partial cross sections. Rather, the total cross section can be inferred from the measured partial cross section and the calculated population of the state through a γ cascade.

For the measurement of the $^{84}\text{Kr}(p, \gamma)^{85}\text{Rb}$ reaction, an effective relative kinetic energy, $E_{\text{cm}}^{\text{eff}}$, of 2.435 MeV was determined from the incident beam energy ($E_{\text{beam}} = 2.7A$ MeV) and energy loss through the $(\text{CH}_2)_n$ target, assuming a reaction cross-section energy dependence similar to the one obtained from statistical model calculations [12,13]. Specifically, effective energies were calculated by solving Eq. (1) for $E_{\text{cm}}^{\text{eff}}$

$$\langle \sigma(E) \rangle = \frac{\int_{E_f}^{E_i} \sigma(E) dE}{\int_{E_f}^{E_i} dE} = \sigma(E_{\text{cm}}^{\text{eff}}). \quad (1)$$

Target thicknesses were established with an α source and the corresponding energy loss of the beam ($E_i - E_f$) was calculated using the program SRIM [23]. The relative uncertainty in the measured cross section due to the determination of the effective energy is estimated to be $\pm 16\%$, while the decay branching ratios of 27% and 65% to the $1/2_1^-$ and $3/2_1^-$ excited states in ^{85}Rb , respectively, are expected to be accurate to within $\pm 10\%$ (see below). The relative cross section uncertainty due to the effective energy determination is estimated via a comparison between the energy dependence of the cross sections predicted by the statistical model at the effective energy and at the effective energy calculated with an energy-independent astrophysical S factor. Here, we observe 22(5) counts due to the 151-keV γ -ray transition in ^{85}Rb , resulting from the $^{84}\text{Kr}(p, \gamma)$ reaction, while 11(4) counts are observed from the 130-keV transition that dominates the decay of the 281-keV state. Combining these yields with the predicted branching ratios in a weighted average, we infer a total reaction cross section at $E_{\text{cm}} = 2.435$ MeV of $94^{+64}_{-30} \mu\text{b}$. A summary of the parameters used for the determination of the reaction cross sections is given in Table I.

In considering the astrophysically important $^{83}\text{Rb} + p$ reaction, clearly correlated γ rays, extending to high energies, are observed at an effective energy of $E_{\text{cm}} = 2.393$ MeV, as shown in Fig. 2. This is entirely consistent with the population of proton-unbound levels in ^{84}Sr and provides conclusive evidence for $^{83}\text{Rb}(p, \gamma)$ events in the present work. However, as can also be seen in Fig. 2, there is significant background throughout the low-energy part of

TABLE I. Parameters used for the determination of radiative capture cross sections. The integrated luminosity represents the product of the total number of beam ions and the areal target density. The detection efficiency is the product of the recoil transmission efficiency, the recoil charge state fraction, the focal plane detection efficiency, the live-time fraction, and the γ -ray detection efficiency. Upper limits are specified at the 90% C.L. Predicted cross sections are based on a statistical model of the reaction [13].

Reaction	E_γ (keV)	Transition	Integrated luminosity (μb^{-1})	Events	Detection efficiency (%)	E_{cm} (MeV)	Measured $\sigma_{partial}$ (μb)	Calculated population (%)	Measured σ_{total} (μb)	Predicted σ_{total} (μb)
$^{83}\text{Rb}(p,\gamma)^{84}\text{Sr}$	793	$2^+ \rightarrow 0^+$	28(5)	16(6)	$1.2_{-0.4}^{+0.1}$	2.393	49_{-21}^{+37}	71(10)	69_{-31}^{+54}	262
	793	$2^+ \rightarrow 0^+$	16(2)	< 16	$1.1_{-0.4}^{+0.1}$	2.259	< 102	71(10)	< 143	154
$^{84}\text{Kr}(p,\gamma)^{85}\text{Rb}$	151	$3/2^- \rightarrow 5/2^-$	12(2)	22(5)	$3.1_{-1.1}^{+0.4}$	2.435	59_{-18}^{+40}	65(10)	91_{-31}^{+63}	385
	130	$1/2^- \rightarrow 3/2^-$	12(2)	11(4)	$3.1_{-1.1}^{+0.3}$	2.435	31_{-12}^{+22}	27(10)	115_{-62}^{+93}	385

the spectrum, due to the β -delayed γ decay of ^{83}Sr (a known beam contaminant). Nevertheless, it is possible to accurately account for this background using well-known ^{83}Sr decay data [24] and by only investigating γ -decay transitions detected in the eight detectors centered at 90° with respect to the beam axis. In this regard, when applying a Doppler correction appropriate for ^{84}Sr recoils, β -delayed transitions from the decays of stopped ^{83}Sr beam contaminants are shifted into several distinct peaks according to the angles of the detectors, while prompt (p,γ) transitions are observed as a peak at a single energy.

Figure 3 illustrates the γ decays observed in the eight TIGRESS detectors centered at 90° with respect to the beam axis in coincidence with $A = 84$ recoils transmitted to the focal plane of EMMA, during the measurement of the $^{83}\text{Rb}(p,\gamma)$ reaction at $E_{cm} = 2.393$ MeV. A timing gate 150 ns wide was applied to obtain the coincidence spectrum

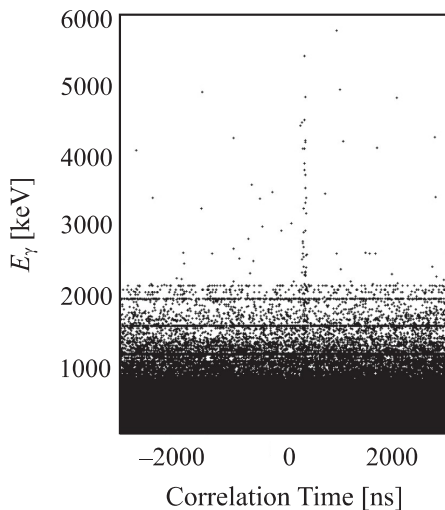


FIG. 2. Observed γ -ray energies in the TIGRESS array, during the measurement of the $^{83}\text{Rb}(p,\gamma)$ reaction, as a function of TIGRESS-EMMA correlation time. A vertical cluster of counts indicates the observation of correlated primary and secondary γ rays up to high energies, corresponding to $^{83}\text{Rb}(p,\gamma)$ events.

while the estimated beam-induced background spectrum was obtained using a 1500-ns-wide timing gate on either side of the coincidence peak, correspondingly normalized by a factor of 1/20. Here, 16(6) counts, in excess of those expected as a result of beam-induced background, are observed at 793 keV, indicating strong population of the 2_1^+ excited level in ^{84}Sr [17]. As such, we measure a partial radiative cross section to the 2_1^+ excited state in ^{84}Sr of $49_{-21}^{+37} \mu b$. For inferring the total reaction cross section, it is necessary to determine the relative amount of γ decays passing through this state. To this end, we performed a calculation with the code SMARAGD [25,26], which is the successor to the NON-SMOKER code [12,13] and allows—additionally to a standard Hauser-Feshbach approach—to consistently compute level populations through the γ cascade in the compound nucleus. Based on this calculation, it is expected that 71(10)% of the total radiative capture cross section flows through this state and, in the present work, no other decay branches were observed.

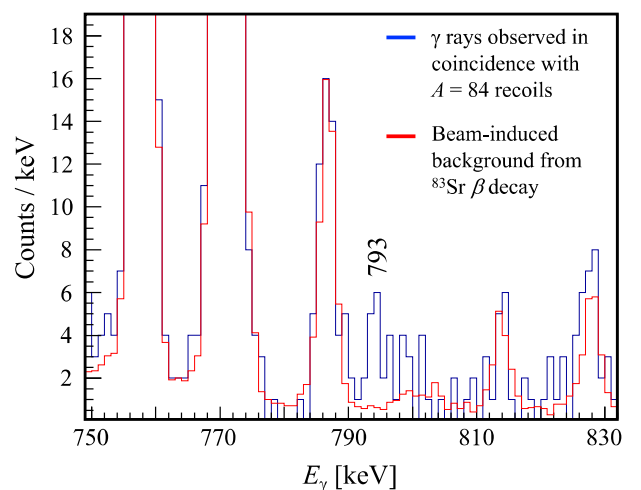


FIG. 3. Gamma rays observed in the eight TIGRESS detectors centered at 90° with respect to the beam axis in coincidence with $A = 84$ recoils, following the $^{83}\text{Rb}(p,\gamma)$ reaction.

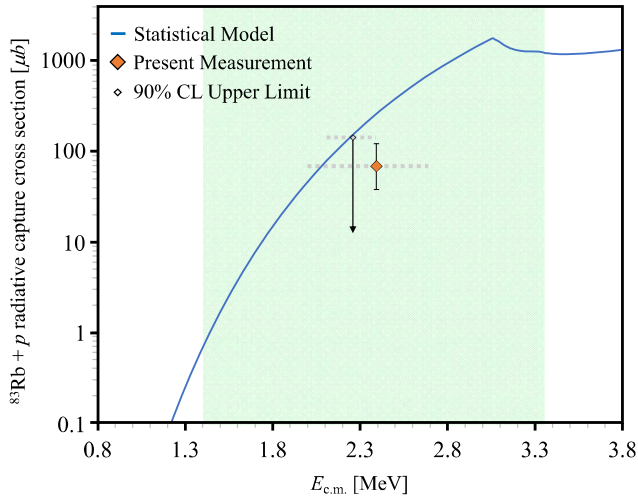


FIG. 4. Total cross section of the $^{83}\text{Rb}(p, \gamma)$ reaction inferred from the measured partial cross section for populating the 793 keV state in ^{84}Sr in comparison with statistical model predictions [13]. The shaded region indicates the approximate location of the Gamow window [14] for the $^{83}\text{Rb}(p, \gamma)$ reaction in CCSN ($2 \text{ GK} < T < 3.5 \text{ GK}$), the experimental points are centred on the effective relative kinetic energies, and the dashed horizontal bars indicate the energies covered in each measurement. The measured point at $E_{\text{cm}} = 2.259 \text{ MeV}$ is a 90% confidence level upper limit.

A further measurement of the $^{83}\text{Rb}(p, \gamma)$ reaction was also performed at $E_{\text{cm}} = 2.259 \text{ MeV}$. Regrettably, only a small excess of counts above background was observed at 793 keV in the resultant γ -ray spectrum, corresponding to population of the 2_1^+ excited state in ^{84}Sr . Therefore, only an upper limit could be placed on the $^{83}\text{Rb}(p, \gamma)$ reaction cross section at $E_{\text{cm}} = 2.259 \text{ MeV}$. An upper limit on the signal in the presence of expected background events was derived using the method of Feldman and Cousins [27], leading to a limit of < 16 , γ -gated, $A = 84$ recoils at the 90% confidence level (C.L.).

In order to assess the astrophysical impact of the present work on p -nuclide abundances, in Fig. 4, we compare the predictions of the statistical model code NON-SMOKER [12,13] with the total cross sections inferred from the experimentally measured partial $^{83}\text{Rb}(p, \gamma)$ reaction cross sections. The NON-SMOKER results for a wide range of nuclides provide the default set of reaction rates for astrophysical calculations in the absence of experimental data. It is hard to draw strong conclusions from the upper limit at $E_{\text{cm}} = 2.259 \text{ MeV}$, but the present experimental determination of the cross section of the $^{83}\text{Rb}(p, \gamma)$ reaction at $E_{\text{cm}} = 2.393 \text{ MeV}$ seems to indicate a value smaller than the HF prediction and, thus, implies a reduced thermonuclear reaction rate in comparison to previous expectations. A recent study [2] reported a strong anticorrelation between the rate of the $^{83}\text{Rb}(p, \gamma)$ reaction and the final abundance of the p nuclide ^{84}Sr . In a first, exploratory recalculation

using the same approach as in [2] and assuming a reduction of the rate by roughly a factor of 4, in line with the cross section range permitted by the experimental results, we found an increase in the resulting ^{84}Sr abundance. This may help explain the observation of enhanced ^{84}Sr levels in CAIs of the Allende meteorite. A more detailed account of the astrophysical simulation will be given in an extended follow-up paper.

In summary, we have performed the first direct measurement of the cross section of an astrophysical p -process reaction in the Gamow window of CCSN using a radioactive beam. A novel experimental method allowed us to measure the partial cross section of the $^{83}\text{Rb}(p, \gamma)$ reaction at energies of $E_{\text{cm}} = 2.259$ and 2.393 MeV , indicating that the thermonuclear reaction rate is lower than that predicted by statistical model calculations. This is most likely caused by an inaccurately predicted proton width [28] and requires further investigation using data across a wider energy range. With a smaller reaction cross section, the abundance of ^{84}Sr produced during the astrophysical p process becomes higher than previously expected, offering a possible explanation for the observation of elevated levels of ^{84}Sr discovered in meteorites. Furthermore, given the discrepancy between the present experimental measurements and theoretical predictions, now, we strongly encourage the further study of p -process reactions involving unstable projectiles. These reactions may hold the key to understanding the observed abundances of several p nuclides throughout our Galaxy.

The authors acknowledge the generous support of the Natural Sciences and Engineering Research Council of Canada. TRIUMF receives federal funding via a contribution agreement through the National Research Council of Canada. The GRIFFIN infrastructure was funded jointly by the Canada Foundation for Innovation, the Ontario Ministry of Research and Innovation, the British Columbia Knowledge Development Fund, TRIUMF, and the University of Guelph. UK personnel were supported by the Science and Technologies Facilities Council (STFC). T.R. acknowledges support by the European COST action “ChETEC” (Grant No. CA16117). N.N. acknowledges support by JSPS KAKENHI (Grants No. 19H00693, No. 21H01087).

*Deceased

†Present Address: FRIB, Michigan State University, East Lansing, Michigan 48824, USA

‡Present Address: Institute of Experimental and Applied Physics, Czech Technical University in Prague, Husova 240/5, 110 00 Prague 1, Czech Republic

§Present Address: ISOLDE, CERN, CH-1211 Geneva 23, Switzerland

|| Present Address: Institut für Kernphysik, Technische Universität Darmstadt, Darmstadt D-64289, Germany

- [1] E. M. Burbidge, G. R. Burbidge, W. A. Fowler, and F. Hoyle, *Rev. Mod. Phys.* **29**, 547 (1957).
- [2] T. Rauscher, N. Nishimura, R. Hirschi, G. Cescutti, A. St. J. Murphy, and A. Heger, *Mon. Not. R. Astron. Soc.* **463**, 4153 (2016).
- [3] T. Rauscher, N. Dauphas, I. Dillmann, C. Fröhlich, Zs. Fülöp, and G. Gyürky, *Rep. Prog. Phys.* **76**, 066201 (2013).
- [4] M. Arnould, *Astron. Astrophys.* **46**, 117 (1976), <http://adsabs.harvard.edu/full/1976A%26A....46..117A>.
- [5] S. E. Woosley and W. M. Howard, *Astrophys. J. Suppl.* **36**, 285 (1978).
- [6] C. Travaglio, F. K. Röpke, R. Gallino, and W. Hillebrandt, *Astrophys. J.* **739**, 93 (2011).
- [7] N. Nishimura, T. Rauscher, R. Hirschi, A. St. J. Murphy, G. Cescutti, and C. Travaglio, *Mon. Not. R. Astron. Soc.* **474**, 3133 (2018).
- [8] M. Arnould and S. Goriely, *Phys. Rep.* **384**, 1 (2003).
- [9] U. Battino, M. Pignatari, C. Travaglio, C. Lederer-Woods, P. Denissenkov, F. Herwig, F. Thielemann, and T. Rauscher, *Mon. Not. R. Astron. Soc.* **497**, 4981 (2020).
- [10] T. Rauscher, G. G. Kiss, Gy. Gyürky, A. Simon, Zs. Fülöp, and E. Somorjai, *Phys. Rev. C* **80**, 035801 (2009).
- [11] T. Rauscher, *Essentials of Nucleosynthesis and Theoretical Nuclear Astrophysics* (IOP, Bristol, 2020).
- [12] T. Rauscher and F.-K. Thielemann, *At. Data Nucl. Data Tables* **75**, 1 (2000).
- [13] T. Rauscher and F.-K. Thielemann, *At. Data Nucl. Data Tables* **79**, 47 (2001).
- [14] T. Rauscher, *Phys. Rev. C* **81**, 045807 (2010).
- [15] G. Hackman and C. E. Svensson, *Hyperfine Interact.* **225**, 241 (2014).
- [16] B. Davids *et al.*, *Nucl. Instrum. Methods Phys. Res., Sect. A* **930**, 191 (2019).
- [17] D. Abriola, M. Bostan, S. Erturk, M. Fadil, M. Galan, S. Juutinen, T. Kibédi, F. Kondev, A. Luca, A. Negret, N. Nica, B. Pfeiffer, B. Singh, A. Sonzogni, J. Timar, J. Tuli, T. Venkova, and K. Zuber, *Nucl. Data Sheets* **110**, 2815 (2009).
- [18] W. Rapp, J. Görres, M. Wiescher, H. Schatz, and F. Käppeler, *Astrophys. J.* **653**, 474 (2006).
- [19] B. L. A. Charlier, F. L. H. Tissot, N. Dauphas, and C. J. N. Wilson, *Geochim. Cosmochim. Acta* **265**, 413 (2019).
- [20] K. Shima, T. Ishihara, and T. Mikumo, *Nucl. Instrum. Methods Phys. Res.* **200**, 605 (1982).
- [21] A. B. Garnsworthy *et al.*, *Nucl. Instrum. Methods Phys. Res., Sect. A* **918**, 9 (2019).
- [22] B. Singh and J. Chen, *Nucl. Data Sheets* **116**, 1 (2014).
- [23] J. F. Ziegler, M. D. Ziegler, and J. P. Biersack, *Nucl. Instrum. Methods Phys. Res., Sect. B* **268**, 1818 (2010).
- [24] E. A. McCutchan, *Nucl. Data Sheets* **125**, 201 (2015).
- [25] T. Rauscher, *Int. J. Mod. Phys. E* **20**, 1071 (2011).
- [26] T. Rauscher, Code SMARAGD, version 0.10.2 (2014).
- [27] G. J. Feldman and R. D. Cousins, *Phys. Rev. D* **57**, 3873 (1998).
- [28] T. Rauscher, *Astrophys. J. Suppl.* **201**, 26 (2012).

Appendix D

Progress Report for Rb Channeling Experiment at TRIUMF

TRIUMF Nuclear Physics Experiment Evaluation Committee (NP-EEC) Experiment Progress Report Detailed Statement of Proposed Research for Experiment S1866

Please use text in 12 point font. The Progress Report page limit is 4 pages (figures included, instructions can be deleted).

Experiment Summary: The overall scientific objective of the experiment remains the same: to observe NEEC isomeric depletion using a radioactive beam of $^{84}\text{Rb}^m$ through an M1 transition with E2 mixing, and separate the Coulex depletion yield from the overall depletion yield. This experiment requires the TIGRESS array to detect the depopulation of the $^{84}\text{Rb}^m$ isomer. The goals of the experiment remain extremely important in our understanding and characterization of these mechanisms, which has both astrophysical and terrestrial relevance, especially in regard to the realisation of nuclear batteries.

Status: The experiment is yet to be run. There are two main reasons for this. Firstly, the priority at the lab is to run experiments with TIGRESS coupled to EMMA, and this experiment does not require EMMA. Second, naturally, the COVID pandemic which has made international travel either impossible or highly restricted. We would not want to run the experiment without the PI and team present on the ground.

Update of information supporting science case: After the proposal was accepted, a profound disagreement emerged between the measured and theoretical NEEC depletion probability in the NEEC discovery experiment reported in Nature for $^{93}\text{Mo}^m$ [1]. This has led to the hypothesis that there is an unknown depletion mechanism at work, over and above the expected NEEC process. Confirming this hypothesis by studying a second system under the controlled conditions of an accelerated radioactive beam therefore has great importance in resolving this controversy. We know of no competing proposals to study this process under such conditions.

Previously there was no published theoretical calculation of the discovery experiment available and now there are methods [1] and [2], and as a result we have vastly improved our NEEC calculations. Since submission of the original proposal, new accurate NEEC resonance strengths relevant to S1866 have been performed in collaboration with the world-expert on NEEC, A. Palffy. These calculations involve a modification from the earlier suggested silicon target to a carbon target. They suggest a NEEC rate between 0.43 and 0.10 total NEEC's s^{-1} based on quickly reaching equilibrium charge state of 29^+ from the initial proposed entrance charge state of 15^+ of a $^{84}\text{Rb}^m$ beam with an intensity of 3×10^7 pps. This was calculated using the CasP tool and methods suggested in [1]; the range in NEEC probability is based on the uncertainty in the nuclear transition energy associated with the NEEC process [3] and is discussed more extensively in the next section.

Update of experimental method: A visit by Ben Wallis (PhD student at York) to TRIUMF in 2019 allowed many aspects of the original proposal to be reviewed in detail with local experts. This confirmed that the use of EMMA was not appropriate to the experiment: the PGAC detectors, although an ideal tool to monitor the CSD due to electron capture mechanisms and to align the crystal target, cannot handle the non-Rutherford scattered projectile intensity of $1 \times 10^7 \text{ s}^{-1}$. In addition, the downstream lampshade of TIGRESS is essential for the overall depletion detection efficiency, due to

the 9 ns, ~30 cm mean decay distance of the 5^- depletion level with a beam emerging at high velocity. Moreover, the positioning of a channeled target with sufficient accuracy would be very hard to achieve. In this regard, and taking account of the controversy regarding the $^{93}\text{Mo}^m$ isomer study, we have elected to change the secondary target in the experiment from a silicon target to a carbon target to parallel the $^{93}\text{Mo}^m$ study. We would also seek to carry out the experiment under this new scenario at a single beam energy of 617MeV (7.35 MeV/u), for which we have evaluated the NEEC rates in figure 1 and 2. At the lower end of the transition energy range (3.31keV, figure 1), we can expect fewer of the L shell resonances available, and thus a maximal NEEC rate of 0.10 s^{-1} .

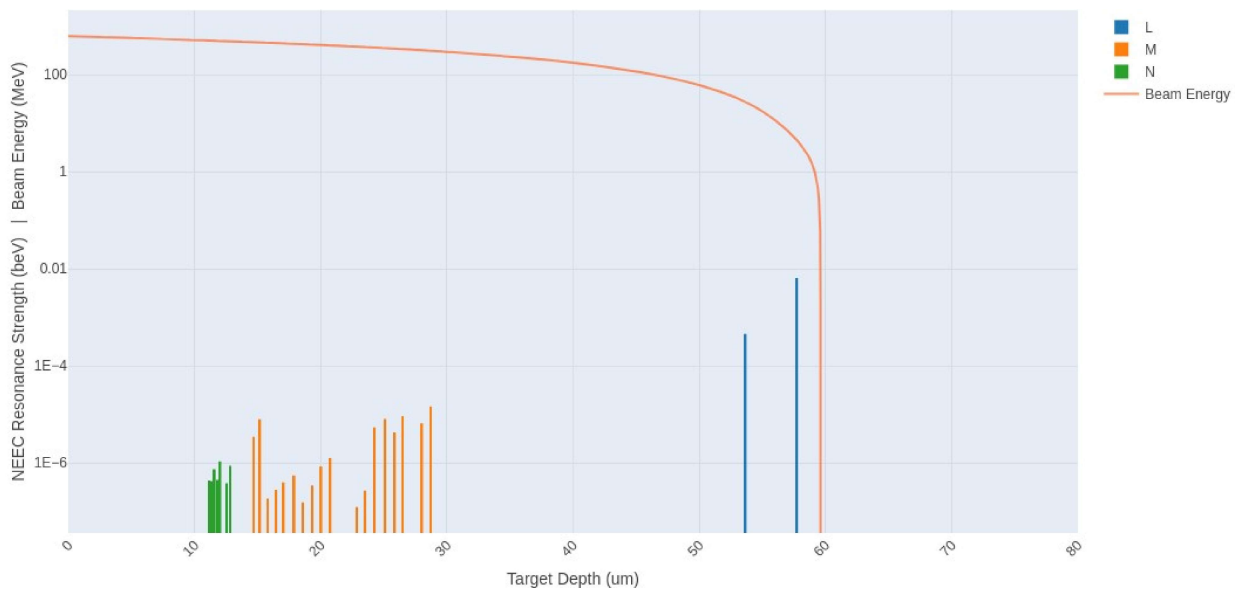


Figure 1: NEEC resonance strengths and explored beam energy within the target with an entrance beam energy of 617MeV (7.35MeV/u), assuming the transition energy is 3.31keV.

Similarly, using the upper limit on the entrance beam energy, we expect the larger transition energy (4keV, figure 2) would provide more of the L shell resonances to be energetically available, and thus a maximal NEEC rate of 0.43 s^{-1} .

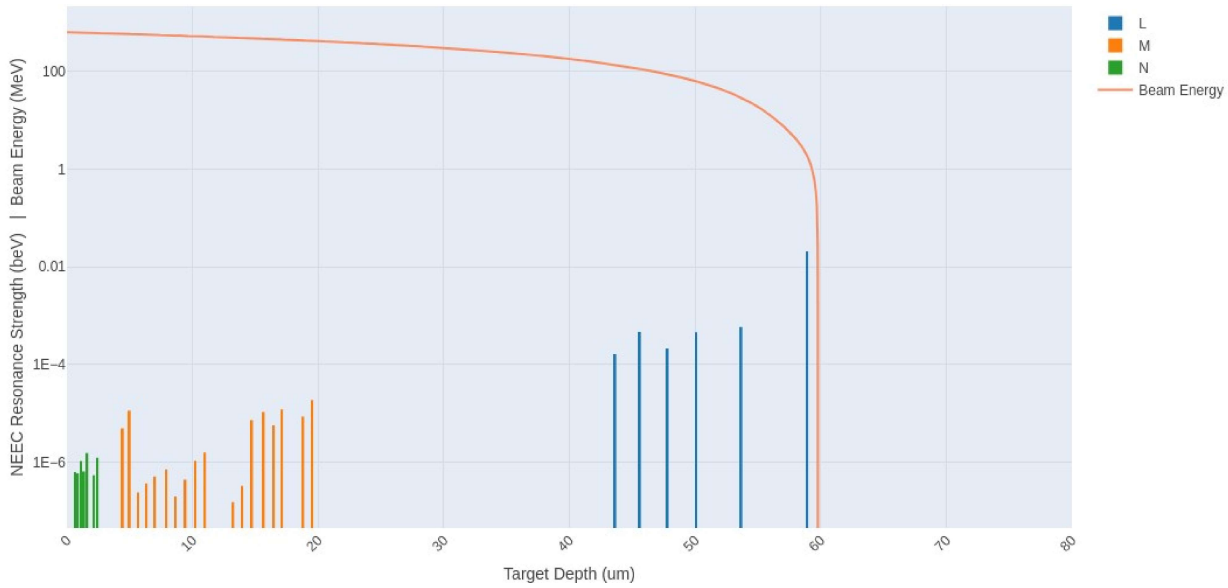


Figure 2: NEEC resonance strengths and explored beam energy within the target with an entrance beam energy of 617MeV (7.35MeV/u), assuming the transition energy is 4.00keV

One might suppose it is best to provide the resonance energy based on only exposing the L shell resonance channels, but these channels require reaching a charge state of 27^+ , reached after quite some distance through the target ~ 10 um. Running the beam at entrance energy for L shell only, 135MeV (1.61MeV/u) would only eventually produce a mean charge state of 24^+ , which would not expose any L shell resonances.

Stopping the radioactive ions within the target is highly undesirable, and we therefore aim to fabricate a target of 55um of Carbon in order to accommodate the maximal number of L shell resonances, whilst allowing for some uncertainty in the thickness, so that scattered beam particles can exit with at least 10 MeV.

Fabricating a 30 um target is also possible to include only M and N shell resonances at 617MeV (7.35MeV/u) entrance energy within the transition uncertainty but will yield a NEEC rate of between $0.00040s^{-1}$ and $0.00028s^{-1}$.

As it stands, we require the original number of shifts, and recent publications have allowed us to propose a simplification to the original setup, described below. The limits in our calculations allow us to assert that there is a good overall chance of observing NEEC, or at least non-coulex isomeric depletion, with a total yield upwards of 2,000 and possibly several orders of magnitude higher, taking 1% detector efficiencies into account. This is within the 16 shifts originally requested, and using now 2 shifts to best characterize Coulex initially, so still a total of 18 shifts is still requested.

In all above scenarios, we predict the possibility of an increase in the overall NEEC probability (and thus the rate) by up to 3 orders of magnitude due to the novel approach to the ^{93}Mo beam analysis in [2], which includes capture of bound carbon electrons. This allows us to dispose of the complex setup

requirements to achieve the large explored electron density in Si channels in the original proposal, as we expect an observable non-Coulex depletion rate overall, even in the worst case scenario. We would expect to be ready to run in this updated scenario, with TIGRESS fully available and no COVID disruption, in early to mid 2022.

References:

[1] Y. Wu, C. H. Keitel, and A. Pálffy. “ ^{93m}Mo isomer depletion via beam-based nuclear excitation by electron capture”. In: *Physical Review Letters*(Mar. 2019). DOI: 10.1103/PhysRevLett.122.212501. URL: <http://arxiv.org/abs/1904.00809> % 20<http://dx.doi.org/10.1103/PhysRevLett.122.212501>.

[2] J. Rzadkiewicz et al. “Novel Approach to Mo 93 m Isomer Depletion: Nuclear Excitation by Electron Capture in Resonant Transfer Process”. In: *Physical Review Letters* 127.4 (July 2021), p. 042501. ISSN: 0031-9007. DOI: 10.1103/PhysRevLett.127.042501. URL: <https://link.aps.org/doi/10.1103/PhysRevLett.127.042501>.

[3] D. Denis-Petit et al. “Calculation of the rate of nuclear excitation by electron transition in an Rb 84m plasma under the hypothesis of local thermodynamic equilibrium using a multiconfiguration Dirac-Fock approach”. In: *Physical Review C* 96.2 (Aug. 2017). ISSN: 24699993. DOI: 10.1103/PhysRevC.96.024604.

Bibliography

- [1] V. I. Goldanskii and V. A. Namiot. "On the excitation of isomeric nuclear levels by laser radiation through inverse internal electron conversion". In: *Physics Letters B* (1976), pp. 393–394. ISSN: 03702693. DOI: [10.1016/0370-2693\(76\)90665-1](https://doi.org/10.1016/0370-2693(76)90665-1).
- [2] C. Brandau, A. Pálffy, and B. Wallis. *Private Communication*. Apr. 2019.
- [3] J. Oxenius. *Kinetic Theory of Particles and Photons*. Vol. 20. Springer Berlin Heidelberg, 1986, pp. 1–32. ISBN: 978-3-642-70728-5. DOI: [10.1007/978-3-642-70728-5](https://doi.org/10.1007/978-3-642-70728-5).
- [4] G. N. Lewis. "A New Principle of Equilibrium". In: *Proceedings of the National Academy of Sciences (PNAS)* 11.3 (1925), pp. 179–183. DOI: <https://doi.org/10.1073/pnas.11.3.179>.
- [5] G. Gosselin and P. Morel. "Enhanced nuclear level decay in hot dense plasmas". In: *Physical Review C - Nuclear Physics* 70.6 (2004), pp. 1–9. ISSN: 1089490X. DOI: [10.1103/PhysRevC.70.064603](https://doi.org/10.1103/PhysRevC.70.064603).
- [6] T. Kibédi et al. "Evaluation of theoretical conversion coefficients using BrIcc". In: *Nuclear Instruments and Methods in Physics Research, Section A: Accelerators, Spectrometers, Detectors and Associated Equipment* 589.2 (May 2008), pp. 202–229. ISSN: 01689002. DOI: [10.1016/j.nima.2008.02.051](https://doi.org/10.1016/j.nima.2008.02.051).
- [7] M. Ryšav and O. Dragoun. "On the reliability of the theoretical internal conversion coefficients". In: *Journal of Physics G: Nuclear and Particle Physics* 26 (2000), pp. 1859–1872. DOI: [10.1088/0954-3899/26/12/309](https://doi.org/10.1088/0954-3899/26/12/309).
- [8] S. Raman, C. W. Nestor, A. Ichihara, and M. B. Trzhaskovskaya. "How good are the internal conversion coefficients now?" In: *Physical Review C* 66.4 (Oct. 2002), p. 044312. DOI: [10.1103/PhysRevC.66.044312](https://doi.org/10.1103/PhysRevC.66.044312).

- [9] F. Yang and J. H. Hamilton. *Modern Atomic and Nuclear Physics*. Revised. World Scientific Publishing Company, 2010. DOI: <https://doi.org/10.1142/9789814374262>.
- [10] D. G. Jenkins and J. L. Wood. *Nuclear Data: A Primer*. IOP Publishing, 2021. DOI: [10.1088/978-0-7503-2674-2](https://doi.org/10.1088/978-0-7503-2674-2).
- [11] S. Gargiulo, I. Madan, and F. Carbone. “Nuclear Excitation by Electron Capture in Excited Ions”. In: *Physical Review Letters* 128.21 (May 2022). ISSN: 10797114. DOI: [10.1103/PhysRevLett.128.212502](https://doi.org/10.1103/PhysRevLett.128.212502).
- [12] A. Pálffy, W. Scheid, and Z. Harman. “Theory of nuclear excitation by electron capture for heavy ions”. In: *Physical Review A - Atomic, Molecular, and Optical Physics* (2006). ISSN: 10941622. DOI: [10.1103/PhysRevA.73.012715](https://doi.org/10.1103/PhysRevA.73.012715).
- [13] R. D. Cowan. *The Theory of Atomic Structure and Spectra*. University of California Press, 1981, pp. 67–138. ISBN: 978-0-520-03821-9. DOI: <https://doi.org/10.1525/9780520906150>.
- [14] P. Ring and P. Schuck. *The Nuclear Many-Body Problem*. 1980 Edition. Springer-Verlag, 1941, pp. 589–590. ISBN: 0-387-09820-8.
- [15] C. Froese-Fischer, T. Brage, and P. Jonsson. *Computational Atomic Structure*. 1st. Routledge, 1997, pp. 1–29. ISBN: 9781315139999. DOI: <https://doi.org/10.1201/9781315139999>.
- [16] P. Bilous, A. Pálffy, and F. Marquardt. “Deep-learning approach for large atomic structure calculations”. In: *ArXiv* (Sept. 2022). DOI: <https://doi.org/10.48550/arXiv.2209.05867>.
- [17] K. Heyde. *Basic Ideas and Concepts in Nuclear Physics*. 3rd Edition. CRC Press, 2004. ISBN: 9780367806576. DOI: <https://doi.org/10.1201/9780367806576>.
- [18] J. D. Holt, S. R. Stroberg, A. Schwenk, and J. Simonis. “Ab initio limits of atomic nuclei”. In: *Physical Review Letters* 126 (2 Jan. 2021), p. 022501. DOI: [10.1103/physrevlett.126.022501](https://doi.org/10.1103/physrevlett.126.022501).
- [19] A. Pálffy. *Theory of nuclear excitation by electron capture for heavy ions*. PhD Thesis, University of Geißen, 2006. URL: <https://d-nb.info/982444052/34>.

- [20] B.R. Martin. *Nuclear and Particle Physics - An Introduction*. 2nd Edition. Wiley and Sons, 2006, pp. 1–28. ISBN: 0-470-01999-9.
- [21] G. D. Dracoulis, P. M. Walker, and F. G. Kondev. “Review of Metastable States in Heavy Nuclei”. In: *Reports on Progress in Physics* 79.7 (May 2016), p. 076301. DOI: [10.1088/0034-4885/79/7/076301](https://doi.org/10.1088/0034-4885/79/7/076301).
- [22] C J Chiara et al. “Isomer depletion as experimental evidence of nuclear excitation by electron capture”. In: *Nature Publishing Group* 554.7691 (2018), pp. 216–218. ISSN: 0028-0836. DOI: [10.1038/nature25483](https://doi.org/10.1038/nature25483).
- [23] M. Buchanan. “Going into resonance”. In: *Nature Physics* 15.3 (Mar. 2019), p. 203. ISSN: 17452481. DOI: [10.1038/s41567-019-0458-z](https://doi.org/10.1038/s41567-019-0458-z).
- [24] C. Rolfs and W. Rodney. *Cauldrons in the Cosmos*. 1st Edition. The University of Chicago Press, 1988, pp. 133–189. ISBN: 0-226-72456-5.
- [25] J. Rządkiwicz et al. “Novel Approach to ^{93m}Mo Isomer Depletion: Nuclear Excitation by Electron Capture in Resonant Transfer Process”. In: *Physical Review Letters* 127.4 (July 2021), p. 042501. ISSN: 0031-9007. DOI: [10.1103/PhysRevLett.127.042501](https://doi.org/10.1103/PhysRevLett.127.042501).
- [26] K. Leach. *TRIUMF EEC Letter of Intent #1865 - 2019*. Tech. rep.
- [27] A. Pálffy, J. Evers, and C. H. Keitel. “Isomer triggering via nuclear excitation by electron capture”. In: *Physical Review Letters* 99.17 (Oct. 2007), p. 172502. ISSN: 00319007. DOI: [10.1103/PhysRevLett.99.172502](https://doi.org/10.1103/PhysRevLett.99.172502).
- [28] A. Pálffy et al. “Nuclear excitation by electron capture followed by fast x-ray emission”. In: *Physics Letters, Section B: Nuclear, Elementary Particle and High-Energy Physics* 661.4 (Mar. 2008), pp. 330–334. ISSN: 03702693. DOI: [10.1016/j.physletb.2008.02.027](https://doi.org/10.1016/j.physletb.2008.02.027).
- [29] Y. Wu, C. H. Keitel, and A. Pálffy. “X-ray assisted nuclear excitation by electron capture in optical laser-generated plasmas”. In: *Physical Review A* 100.6 (Sept. 2019), p. 063420. DOI: <https://doi.org/10.1103/PhysRevA.100.063420>.
- [30] P. Walker and Z. Podolyák. “100 years of nuclear isomers—then and now”. In: *Physica Scripta* 95.4 (Feb. 2020), p. 044004. ISSN: 0031-8949. DOI: [10.1088/1402-4896/ab635d](https://doi.org/10.1088/1402-4896/ab635d).

- [31] K. Ślabkowska et al. “ ^{93m}Mo Isomer Depletion via Nuclear Excitation by Electron Capture: Energy Released for Different Atomic Subshells as Benchmarks for a Beam-based Scenario Approach”. In: *Acta Physica Polonica B* 50.3 (Aug. 2019), p. 651. ISSN: 0587-4254. DOI: [10.5506/APhysPolB.50.651](https://doi.org/10.5506/APhysPolB.50.651).
- [32] S. Guo et al. “Probing ^{93m}Mo Isomer Depletion with an Isomer Beam”. In: *Physical Review Letters* 128.24 (June 2022), p. 242502. ISSN: 0031-9007. DOI: [10.1103/PhysRevLett.128.242502](https://doi.org/10.1103/PhysRevLett.128.242502).
- [33] Y. Wu, C. H. Keitel, and A. Pálffy. “ ^{93m}Mo isomer depletion via beam-based nuclear excitation by electron capture”. In: *Physical Review Letters* 122.21 (Mar. 2019), p. 212501. DOI: [10.1103/PhysRevLett.122.212501](https://doi.org/10.1103/PhysRevLett.122.212501).
- [34] A. K. Jain et al. “Atlas of Nuclear Isomers”. In: *Nuclear Data Sheets* 128 (Sept. 2015), pp. 1–130. ISSN: 00903752. DOI: [10.1016/j.nds.2015.08.001](https://doi.org/10.1016/j.nds.2015.08.001).
- [35] P. M. Walker. “High-K isomers: some of the questions”. In: *EPJ Web of Conferences - Heavy Ion Accelerator Symposium 2015: International Nuclear Structure Conference in Remembrance of George Dracoulis* 123 (Sept. 2016), p. 01001. DOI: <https://doi.org/10.1051/epjconf/201612301001>.
- [36] J. J. Carroll et al. *Dynamic Materials, Intelligence, and Power for Future Army Capabilities: A Report of the FY19 Army Science Planning and Strategy Meetings*. Tech. rep. May 2019. URL: <https://apps.dtic.mil/sti/citations/AD1077248>.
- [37] T. D. Arber et al. “Contemporary particle-in-cell approach to laser-plasma modelling”. In: *Plasma Physics and Controlled Fusion* 57.11 (Sept. 2015), p. 113001. ISSN: 13616587. DOI: [10.1088/0741-3335/57/11/113001](https://doi.org/10.1088/0741-3335/57/11/113001).
- [38] G. J. Tallents. “Plasma and Atomic Physics”. In: *An Introduction to the Atomic and Radiation Physics of Plasmas*. Cambridge University Press, Feb. 2018, pp. 1–19. DOI: [10.1017/9781108303538.002](https://doi.org/10.1017/9781108303538.002).
- [39] M. R. Harston and J. F. Chemin. “Mechanisms of nuclear excitation in plasmas”. In: *Physical Review C* 59.5 (May 1999), pp. 2462–2473. DOI: <https://doi.org/10.1103/PhysRevC.59.2462>.

- [40] J. Gunst, Y. Wu, C. H. Keitel, and A. Pálffy. “Nuclear excitation by electron capture in optical-laser-generated plasmas”. In: *Physical Review E* 97.6 (June 2018), p. 063205. DOI: <https://doi.org/10.1103/PhysRevE.97.063205>.
- [41] Y. Wu and A. Pálffy. “Determination of Plasma Screening Effects for Thermonuclear Reactions in laser-generated Plasmas”. In: *The Astrophysical Journal* 838.1 (Mar. 2017), p. 55. ISSN: 1538-4357. DOI: [10.3847/1538-4357/aa6252](https://doi.org/10.3847/1538-4357/aa6252).
- [42] M. G. Haines, M. S. Wei, F. N. Beg, and R. B. Stephens. “Hot-electron temperature and laser-light absorption in fast ignition”. In: *Physical Review Letters* 102.4 (Jan. 2009), p. 045008. DOI: [10.1103/PhysRevLett.102.045008](https://doi.org/10.1103/PhysRevLett.102.045008).
- [43] J. Gunst et al. “Direct and secondary nuclear excitation with x-ray free-electron lasers”. In: *Physics of Plasmas* 22.11 (Nov. 2015), p. 112706. DOI: [10.1063/1.4935294](https://doi.org/10.1063/1.4935294).
- [44] H. K. Chung, R. W. Lee, M. H. Chen, and Y. Ralchenko. *The How To For FLYCHK @ NIST*. Tech. rep. Nov. 2008. URL: https://nlte.nist.gov/FLY/Doc/Manual_FLYCHK_Nov08.pdf.
- [45] N. Cue. “Nuclear excitation by target electron capture”. In: *Nuclear Instruments and Methods in Physics Research Section B: Beam Interactions with Materials and Atoms* 40-41 (Apr. 1989), pp. 25–27. DOI: [10.1016/0168-583X\(89\)90914-2](https://doi.org/10.1016/0168-583X(89)90914-2).
- [46] N. Cue, J.C. Poizat, and J. Remillieux. “Exciting the Nucleus by Target Electron Capture into Atomic Orbitals”. In: *Europhysics Letters* 8.1 (Jan. 1989), pp. 19–23. DOI: [10.1209/0295-5075/8/1/004](https://doi.org/10.1209/0295-5075/8/1/004).
- [47] J. F. Ziegler, M. D. Ziegler, and J. P. Biersack. “SRIM - The stopping and range of ions in matter (2010)”. In: *Nuclear Instruments and Methods in Physics Research, Section B: Beam Interactions with Materials and Atoms* (June 2010), pp. 1818–1823. ISSN: 0168583X. DOI: [10.1016/j.nimb.2010.02.091](https://doi.org/10.1016/j.nimb.2010.02.091).
- [48] B. Wallis. *Producing Environments for Nuclear Excitation by Electron Capture*. 2nd Year PhD report, University of York, Sept. 2019.
- [49] W. Herr and B. Muratori. “Concept of luminosity”. In: *CERN Accelerator School: Intermediate Accelerator Physics* (Apr. 2006), pp. 361–378. DOI: [10.5170/CERN-2006-002.361](https://doi.org/10.5170/CERN-2006-002.361).

- [50] Entire Evaluated Nuclear Structure Data File (ENSDF) database as of November, 1st, 2020. URL: <http://www.nndc.bnl.gov/ensarchivals/>.
- [51] National Institute of Standards and Technology (NIST) - Atomic Spectra Database: ground states and ionization energies of atoms and atomic ions. Nov. 2020. URL: <https://www.nist.gov/pml/atomic-spectra-database>.
- [52] C. Granja, J. Kuba, A. Haiduk, and O. Renner. "Survey of nuclei for low-energy nuclear excitation in laser-produced plasma". In: *Nuclear Physics A* 784.1-4 (2007), pp. 1–12. ISSN: 03759474. DOI: [10.1016/j.nuclphysa.2006.12.003](https://doi.org/10.1016/j.nuclphysa.2006.12.003).
- [53] K. T. Jagdish. *Evaluated Nuclear Structure Data File A Manual for Preparation of Data Sets*. Tech. rep. Feb. 2001. DOI: <https://doi.org/10.2172/779777>.
- [54] A. V. Aho. *Algorithms for finding patterns in strings, Handbook of theoretical computer science (vol. A): algorithms and complexity*. MIT Press Elsevier, 1990, pp. 255–300. ISBN: 9780444880710. DOI: <https://doi.org/10.1016/B978-0-444-88071-0.50010-2>.
- [55] R. Schuch et al. "The new Stockholm electron beam ion trap (S-EBIT)". In: *Journal of Instrumentation* 5.12 (Dec. 2010), p. C12018. ISSN: 17480221. DOI: [10.1088/1748-0221/5/12/C12018](https://doi.org/10.1088/1748-0221/5/12/C12018).
- [56] S. Gargiulo, M. F. Gu, F. Carbone, and I. Madan. "Nuclear Excitation by Muon Capture". In: *Physical Review Letters* 129.14 (Feb. 2022), p. 142501. DOI: <https://doi.org/10.1103/PhysRevLett.129.142501>.
- [57] M. Polasik et al. "Resonance conditions for ^{93m}Mo isomer depletion via nuclear excitation by electron capture in a beam-based scenario". In: *Physical Review C* 95.3 (2017), p. 034312. ISSN: 2469-9985. DOI: [10.1103/PhysRevC.95.034312](https://doi.org/10.1103/PhysRevC.95.034312).
- [58] S. Datz and C. Moak. "Heavy Ion Channeling". In: *Treatise on Heavy Ion Science*. Vol. 6. 1985, pp. 167–240. DOI: [10.1007/978-1-4615-8103-1_5](https://doi.org/10.1007/978-1-4615-8103-1_5).
- [59] C. Cohen and D. Dauvergne. "High energy ion channeling: Principles and typical applications". In: *Nuclear Instruments and Methods in Physics Research, Section B: Beam Interactions with Materials and Atoms* 225.1-2 SPEC. ISS. (2004), pp. 40–71. ISSN: 0168583X. DOI: [10.1016/j.nimb.2004.03.017](https://doi.org/10.1016/j.nimb.2004.03.017).

- [60] D. Dauvergne. “Crystal assisted experiments for multi-disciplinary physics with heavy ion beams at GANIL”. In: *Journal of Physics: Conference Series* 629.21 (June 2015), p. 012010. ISSN: 1742-6588. DOI: [10.1088/1742-6596/629/1/012010](https://doi.org/10.1088/1742-6596/629/1/012010).
- [61] Z. Yuan and J. C. Kimball. “First-principles calculation of the cross sections for nuclear excitation by electron capture of channeled nuclei”. In: *Physical Review C* 47.1 (Jan. 1993), pp. 323–328. DOI: <https://doi.org/10.1103/PhysRevC.47.323>.
- [62] F. G. Kondev. *84Rb ENSDF File*. Full Evaluation, NDS 110 2815, Sept. 2009. URL: <https://www.nndc.bnl.gov/ensdf/>.
- [63] J. U. Andersen. *Notes on Channeling*. Univerisity of Aarhus, Dec. 2014, pp. 1–137. URL: https://phys.au.dk/fileadmin/site_files/publikationer/Lecture_notes/Channeling_notes_2018.pdf.
- [64] P. Smulders and U. Wahl. *FLUX7 - Simulating trajectories of Ions in Crystals - Website*. 2017. URL: <http://www.pjms.nl/FLUXHTML/>.
- [65] S. Wang et al. “Large-area free-standing ultrathin single-crystal silicon as processable materials”. In: *Nano Letters* 13.9 (2013), pp. 4393–4398. ISSN: 15306984. DOI: [10.1021/nl402230v](https://doi.org/10.1021/nl402230v).
- [66] D. Cline et al. *Gosia user manual for simulation and analysis of coulomb excitation experiments*. Tech. rep. 2012. URL: https://www.pas.rochester.edu/~cline/Gosia/Gosia_Manual_20120510.pdf.
- [67] R. Barlow. *Twiss parameters and bunch properties - Lecture Notes*. University of Huddersfield, Jan. 2015, pp. 1–6.
- [68] M. Berz, K. Makino, and W. Wan. *An Introduction to Beam Physics*. eng. 1st ed. Baton Rouge: CRC Press, 2015. ISBN: 9780750302630. DOI: <https://doi.org/10.1201/b12074>.
- [69] G. Hackman, F. Ames, R. Baartman, and B. Wallis. *Private Communication*. Dec. 2018.
- [70] J. U. Andersen et al. “Heavy ion channeling”. In: *Nuclear Instruments and Methods in Physics Research, Section B: Beam Interactions with Materials and Atoms* (1996), pp. 292–307. ISSN: 0168583X. DOI: [10.1016/0168-583X\(96\)00209-1](https://doi.org/10.1016/0168-583X(96)00209-1).

-
- [71] K. Nordlund, F. Djurabekova, and G. Hobler. "Large fraction of crystal directions leads to ion channeling". In: *Physical Review B* 94.21 (Dec. 2016), p. 214109. ISSN: 24699969. DOI: [10.1103/PhysRevB.94.214109](https://doi.org/10.1103/PhysRevB.94.214109).
- [72] E. Bagli et al. "A model for the interaction of high-energy particles in straight and bent crystals implemented in Geant4". In: *The European Physical Journal C* 74 (8 2014), p. 2996. DOI: <https://doi.org/10.1140/epjc/s10052-014-2996-5>.